https://lib.uliege.be https://matheo.uliege.be

Hydrodynamic characterisation of a body-like shape: a contribution to guide the search for victims of drowning in rivers

Auteur : Delhez, Clément
Promoteur(s) : Dewals, Benjamin; Erpicum, Sebastien
Faculté : Faculté des Sciences appliquées
Diplôme : Master en ingénieur civil des constructions, à finalité spécialisée en "civil engineering"
Année académique : 2020-2021
URI/URL : http://hdl.handle.net/2268.2/11498

Avertissement à l'attention des usagers :

Tous les documents placés en accès ouvert sur le site le site MatheO sont protégés par le droit d'auteur. Conformément aux principes énoncés par la "Budapest Open Access Initiative"(BOAI, 2002), l'utilisateur du site peut lire, télécharger, copier, transmettre, imprimer, chercher ou faire un lien vers le texte intégral de ces documents, les disséquer pour les indexer, s'en servir de données pour un logiciel, ou s'en servir à toute autre fin légale (ou prévue par la réglementation relative au droit d'auteur). Toute utilisation du document à des fins commerciales est strictement interdite.

Par ailleurs, l'utilisateur s'engage à respecter les droits moraux de l'auteur, principalement le droit à l'intégrité de l'oeuvre et le droit de paternité et ce dans toute utilisation que l'utilisateur entreprend. Ainsi, à titre d'exemple, lorsqu'il reproduira un document par extrait ou dans son intégralité, l'utilisateur citera de manière complète les sources telles que mentionnées ci-dessus. Toute utilisation non explicitement autorisée ci-avant (telle que par exemple, la modification du document ou son résumé) nécessite l'autorisation préalable et expresse des auteurs ou de leurs ayants droit.

UNIVERSITY OF LIEGE
FACULTY OF APPLIED SCIENCES

Hydrodynamic characterisation of a body-like shape: a contribution to guide the search for victims of drowning in rivers

Advisor
B. Dewals (ULiege)

Co-advisor
S. Erpicum (ULiege)

Jury
A. Hage (ULiege)
M. Pirotton (ULiege)
T. Andrianne (ULiege)
N. Riviere (INSA, Lyon)

DISSERTATION SUBMITTED AS PART REQUIREMENT FOR THE DEGREE OF MASTER IN CIVIL ENGINEERING BY DELHEZ CLÉMENT

Academic year 2020-2021

Remerciements

Je voudrai tout d'abord remercier mon promoteur Mr. Dewals ainsi que mon co-promoteur Mr. Erpicum pour m'avoir permis d'étudier un sujet si intéressant. Ceci en me laissant une grande autonomie dans ma façon de travailler tout en corrigeant mes erreurs pour me permettre d'avancer.

Je remercie également l'équipe du Laboratoire d'Hydraulique (Claude Lhermerout, Grégory Thonard, Maxime Mathieu), ainsi que celle du Bassin de carènes (André Hage, Radomir Jašic et Philippe Rigo) sans qui mes expériences n'auraient pu se réaliser.

Finalement, je tiens à remercier tous mes proches qui ont supportés mes hauts et mes bas pendant ce travail. Et plus particulièrement Eloïse qui a fait de son mieux pour m'encourager et me tirer vers le haut durant cette période.

Abstract

This thesis is a contribution towards model-based guidance for the search of victims of drowning in rivers. It includes two parts: (i) an experimental study aiming at characterizing the hydrodynamic properties of a human-body shape, and (ii) the setup of a preliminary computational tool designed to simulate the drift of a human body in an open channel.

Literature on the prediction of the motion of floating objects and bodies in water was first reviewed. For the case of a human body, a lack of knowledge on the parameters influencing controlling the drift was highlighted.

Next, two complementary series of laboratory experiments were undertaken, one in a 20-m long glass flume and the second one in a 100-m long towing tank. The former involves rigid body models (dummies) at a scale of approximately 1:6, the covered range of relative velocity is 0.09 and 0.2 m/s and the particulate Reynolds number spans between $2.8 * 10^4$ and $5.2 * 10^4$. In the towing tank, a prototype-scale rigid body model was used, with a velocity of 0.1 to 0.5 m/s, and a particulate Reynolds number varying between 10^5 and $8 * 10^5$.

The experiments enabled estimating the drag coefficient of the body models, and the results were compared to a reference shape (cylinder). A systematic analysis of parameters such as the body shape, its orientation with respect to the approaching flow, and its submersion depth was undertaken. Additional parameters were also explored, including the presence of hair and clothes.

Based on a combination of backwater profile calculation and parametrized cross-sectional velocity distribution, a 3D computational model of the flow field in the laboratory flume was set up. Simple drift computations were performed, which focused on the body motion in the streamwise direction. This enabled sensitivity analysis regarding the relative importance of the drag and added mass coefficients.

Finally, limitations of the study are discussed and future research directions are proposed.

Résumé

Cette thèse est une contribution au guidage par modèle pour la recherche de victimes de noyade en rivière. Elle comprend deux parties : (i) une étude expérimentale visant à caractériser les propriétés hydrodynamiques d'une forme de corps humain, et (ii) la mise en place d'un outil de calcul préliminaire destiné à simuler la dérive d'un corps humain dans un canal ouvert.

La littérature sur la prédiction du mouvement des objets et des corps flottants dans l'eau a d'abord été examinée. Dans le cas d'un corps humain, un manque de connaissances sur les paramètres influençant le contrôle de la dérive a été mis en évidence.

Ensuite, deux séries complémentaires d'expériences de laboratoire ont été entreprises, l'une dans un canal en verre de 20 m de long et la seconde dans un bassin de carène de 100 m de long. La première implique des modèles de corps rigides (mannequins) à une échelle d'environ 1:6, la plage de vitesse relative couverte est de 0,09 et 0,2 m/s et le nombre de Reynolds des particules s'étend de $2,8*10^4$ à $5,2*10^4$. Dans le bassin de carène, un modèle de corps rigide à l'échelle du prototype a été utilisé, avec une vitesse de 0,1 à 0,5 m/s et un nombre de Reynolds particulaire variant entre 10^5 et $8*10^5$.

Les expériences ont permis d'estimer le coefficient de traînée des modèles de corps, et les résultats ont été comparés à une forme de référence (cylindre). Une analyse systématique des paramètres tels que la forme du corps, son orientation par rapport au flux d'approche et sa profondeur de submersion a été entreprise. D'autres paramètres ont également été étudiés, notamment la présence de cheveux et de vêtements.

Un modèle de calcul 3D du champ d'écoulement dans le canal de laboratoire a été mis en place en combinant le calcul du profil du flux et la distribution paramétrée de la vitesse transversale. Des calculs de dérive simples ont été effectués, qui se sont concentrés sur le mouvement du corps dans la direction du courant. Cela a permis une analyse de sensibilité concernant l'importance relative des coefficients de traînée et de masse ajoutée.

Enfin, les limites de l'étude sont discutées et des directions de recherche futures sont proposées.

Contents

1 Introduction **1**

2 Background **3**

2.1 Human body . . . 3

2.2 Floating objects . . . 9

2.3 Objectives of this work . . . 12

3 Experimental modelling **13**

3.1 Laboratory flume . . . 13

3.1.1 Experimental setup and flow characteristics . . . 13

3.1.2 Body models characteristics . . . 18

3.1.3 Measurement devices . . . 26

3.2 Towing tank . . . 34

3.2.1 Experimental setup . . . 34

3.2.2 Models characteristics . . . 35

3.2.3 Measurement devices . . . 36

3.3 Results . . . 38

3.3.1 Determination of the cross sectional velocity profile . . . 38

3.3.2 Measurement of drag with a Re_p between 10^4 and 10^5 . . . 41

3.3.3 Towing tank . . . 56

3.3.4 Comparison between the different scale tests . . . 59

3.4 Conclusion . . . 63

4 Numerical modelling **64**

4.1 Schematisation of the body models . . . 64

4.1.1 Pointwise approximation . . . 64

4.1.2 Simplified shape . . . 65

4.2 Equations of motion . . . 68

4.2.1 Translation . . . 68

4.2.2 Rotation . . . 69

4.3 Flow characteristic . . . 70

4.3.1 Flow depths . . . 70

4.3.2 Flow velocity . . . 72

4.4 Results . . . 81

4.4.1 Streamwise body motion 81
4.4.2 Influence of the initial orientation of the body 86
4.5 Conclusion 95

5 Outlook **96**
5.1 Improvements 96
5.1.1 Experimental modelling 96
5.1.2 Numerical modelling 99
5.2 Collaborative work 104

6 Conclusion **105**

Bibliography **107**

A Appendix **110**
.1 First measuring system, variable, surface 110
.2 First measuring system, stable, surface 112
.3 Second measuring system, very stable, surface 114
.4 Second measuring system, very stable, mid height 118
.5 Measurement of drag with a $Re = 0$ and lower Re_p 122

1 | Introduction

The United Nations (UN) predicted in 2018 that two thirds of the world population will live in an urban environment in 2050, with a total population of 50 billions inhabitants in total. In 2014, the UN estimated that there were 372 000 drowning accidents per year with a worldwide population of 7.2 billions inhabitants, and with 90% of these drowning accidents happening in low- and middle-income countries. These countries are expected to be the countries with highest urban population in the world in the years to come (World Health Organization, 2014).

It could be thought that this problem has less impact on developed nations like ours. However, in Belgium there are in average 77 drowning accidents a year (Bilterijs et al., 2019). In France, *Santé publique France* listed 1649 drowning accidents over the summer 2018 (from 1/06/18 to 30/09/18) including 22% of them occurring in rivers (Santé publique France, 2019). They pointed that the high portion of people unable to swim, although if it is supposed to be a basic ability in developed nations.

As a result, drowning has been identified as a major cause of death and strategies are being developed to reduce the drowning risk.

Currently there are mostly two ways for searching victims of drowning: search with sonar and search by divers. Both techniques are often combined. A sonar may prove hard to use in rivers because of the uneven river bottom, the small inspection area and its relatively high price. Search by divers is used in urban rivers but the search strategy is mainly determined by the divers themselves and their experience. Indeed, the main data available to underwater brigades are often limited to the discharge of the river and the water depth at some points. Furthermore, flow conditions need to be safe enough to allow a diving search and turbidity reduces the effectiveness of the investigation. As a consequence, chances to find a drowning victim when the body has sunk are unfortunately relatively low. Hence, it happens that relatives of the victim have to wait for days or weeks before they can grieve, while public services devote a lot of resources to a particularly difficult task. The need for a tool to improve search of victims of drowning is justified both from a human point of view and from an economic perspective.

The ultimate goal of the work initiated in this master thesis is to improve our understanding of the motion of a drowned human body drifting in a river with the aim of being able to predict the vertical and horizontal motions from the point of disappearance of the body. Such a model would provide a map of probability of presence based on the flow conditions of the river and additional parameters (water temperature, body characteristics, operation of hydraulic structures ...). This map could serve as a guidance for the search by divers so as to increase the chances of finding the victim in a shorter period of time.

This work is among the first ones on the physical and hydrological processes influencing the motion of a drowning victim. In chapter 2, we discuss a typical position of a drowning victim, as well as the main parameters influencing the drift of the body. A literature survey is briefly summarised. Chapter 3 presents an experimental study. In chapter 4, results of the experimental study are combined with a first, simplified, numerical model aiming at reproducing the drift of a human body in water. Outlooks are discussed in chapter 5.

2 | Background

The first step of this work consists in a summary of relevant literature. These studies can be classified into two groups: those studying the behaviour of a human body in water and those examining other floating objects.

At the end of this chapter, we clarify the specific objectives of this master thesis.

2.1 Human body

The disappearance of drowned persons has been a concern for ages, operational tools to address this problem remain limited. A pioneering study was conducted by Reh (1967), who established a statistical correlation between the putrefactive signs on submerged bodies and the aquatic temperature during the Postmortem Submersion Interval (PMSI). However, as reported by Madea and Doberentz (2010), these tables are considered now as obsolete to a great extent, as water temperature ranges changed between his study and present days. Indeed, tables from Reh (1967) show a maximum water temperature not exceeding 20^oC while nowadays these temperatures are exceeded in many urban rivers (Cool Huy, 2021).

Megyesi et al. (2005) were the first ones to identify the need for a more generally accepted score for estimating the Postmortem Interval (PMI), a tool to help estimating the hour of death in any kind of death, not especially drowning. Their research was designed to examine the ways that forensic anthropologists could improve their PMI estimations based on decomposition by using a more quantitative approach. A total of 68 human remains with a known date of death were scored based on the degree of putrefaction and they established a first correlation between these evaluated scores and the Accumulated Degree Days (ADD), as detailed in the following.

Two key parameters have been defined thanks to their study: the Total Body Score (TBS) and the Accumulated Degree Day (ADD).

The Total Body Score is obtained from visual inspection of the body. The table displayed in Figure 2.1 are used to assign separate scores to the decomposition of the head and neck, chest and limbs. Then, the three scores are added to finally get the TBS based on the observations made on the recovered body.

Categories and stages of decomposition for the head and neck.

A. Fresh
- (1 pt) Fresh, no discoloration

B Early decomposition
- (2 pts) Pink-white appearance with skin slippage and some hair loss.
- (3 pts) Gray to green discoloration: some flesh still relatively fresh.
- (4 pts) Discoloration and/or brownish shades particularly at edges, drying of nose, ears and lips.
- (5 pts) Purging of decompositional fluids out of eyes, ears, nose, mouth, some bloating of neck and face may be present.
- (6 pts) Brown to black discoloration of flesh.

C. Advanced decomposition
- (7 pts) Caving in of the flesh and tissues of eyes and throat.
- (8 pts) Moist decomposition with bone exposure less than one half that of the area being scored.
- (9 pts) Mummification with bone exposure less than one half that of the area being scored.

D. Skeletonization
- (10 pts) Bone exposure of more than half of the area being scored with greasy substances and decomposed tissue.
- (11 pts) Bone exposure of more than half the area being scored with desiccated or mummified tissue.
- (12 pts) Bones largely dry, but retaining some grease.
- (13 pts) Dry bone.

Figure 2.1: Table for the estimation of the Head-neck score (Megyesi et al., 2005)

The obtained TBS has then been linked to the Accumulated Degree Days in order to be able to calculate the PMI. Megyesi et al. (2005) identified that the main factor influencing the rate of body decomposition was the ambient temperature. A study of these temperatures and duration on known cases enables linking TBS and ADD and finally get the PMI. Once the relation TBS-ADD has been established, they were able to estimate the PMI on new cases. The ADD is defined as follows:

$$ADD = \sum_i T_i * \frac{h_i}{24} \tag{2.1}$$

with T_i the temperature in degree Celsius during the time period i and h_i the period of time in hours during which the temperature T_i has been measured divided by 24 to estimate the ADD in days instead of hours.

The ADD is considered not dependent on the environment for the post-mortem interval. This means that a body in water will have the same ADD as a body in air at the same temperature and for the same time span. As the ADD is of capital importance for the studied subject, here is an example of its calculation.

Somebody dies in his garden at the sunrise and has been found on the next sunrise. The water/air temperature during the day was $T = 15^oC$ while it was $T = 8^oC$ at night with a night of 10h. The calculation of the ADD is the following:

$$ADD = 15 * \frac{14}{24} + 8 * \frac{10}{24} = 12.08 \tag{2.2}$$

Once the two key parameters have been identified, more studies have been undertaken on their relation. Simmons et al. (2010) were the first to compare different results of studies made on the TBS-ADD relation in various conditions. The goal of their study was to determine the dependence on other parameters like the size of the body, the nature of the environment, the body fat percentage, etc. Their conclusion supports once again the relevance of the TBS-ADD relation and highlights the fact that the most influential other parameter is the presence or absence of insects. That means that at equivalent ADD, a body is decomposed differently if the environment allows insects to interact with it or not. Whether the absence of insects occurs indoors, as a result of burial, or as a result of submersion in water, is essentially irrelevant. It is merely the absence of insects that results in an alteration (decrease) of the rate at which decomposition occurs (Simmons et al., 2010).

It is now obvious that another decomposition score, the Total Aquatic Decomposition Score (TADS), was needed to find the PMSI in the same way as the PMI with the TBS. The creation of corresponding tables has been realised by the same team as that which studied the influence of the environment on the TBS-ADD relation (Heaton et al., 2010).

The TBS-ADD relation established by Megyesi et al. (2005) works very precisely when the environment is known Humphreys et al. (2013). The need of keeping this consistency between body score and ADD was evident for the TADS-ADD relation. Once again they divided the score in three intermediate scores which are the Facial Aquatic Decompositional Score (FADS, Figure 2.2), Body Aquatic Decompositional Score (BADS, Figure 2.3) and Limbs Aquatic Decompositional Score (LADS, Figure 2.4). The sum of these three scores gives the TADS.

FADS	Description
1	No visible changes.
2	Slight pink discoloration, darkened lips, goose pimpling.
3	Reddening of face and neck, marbling visible on face. Possible early signs of animal activity/predation—concentrated on the ears, nose, and lips.
4	Bloating of the face, green discoloration, skin beginning to slough off.
5	Head hair beginning to slough off—mostly at the front. Brain softening and becoming liquefied. Tissue becoming exposed on face and neck. Green/black discoloration.
6	Bone becoming exposed—concentrated over the orbital, frontal, and parietal regions. Some on the mandible and maxilla. Early adipocere formation.
7	More extensive skeletonization on the cranium. Disarticulation of the mandible.
8	Complete disarticulation of the skull from torso. Extensive adipocere formation.

Figure 2.2: Table for the estimation of the FADS (Heaton et al., 2010)

BADS	Description
1	No visible changes.
2	Slight pink discoloration, goose pimpling.
3	Yellow/green discoloration of abdomen and upper chest. Marbling. Internal organs beginning to decompose/autolysis.
4	Dark green discoloration of abdomen, mild bloating of abdomen, initial skin slippage.
5	Green/purple discoloration, extensive abdominal bloating—tense to touch, swollen scrotum in males, exposure of underlying fat and tissues.
6	Black discoloration, bloating becoming softer, initial exposure of internal organs and bones.
7	Further loss of tissues and organs, more bone exposed, initial adipocere formation.
8	Complete skeletonization and disarticulation.

Figure 2.3: Table for the estimation of the BADS (Heaton et al., 2010)

LADS	Description
1	No visible changes.
2	Mild wrinkling of skin on hands and/or feet. Possible goose pimpling.
3	Skin on palms of hands and/or soles of feet becoming white, wrinkled, and thickened. Slight pink discoloration of arms and legs.
4	Skin on palms of hands and/or soles of feet becoming soggy and loose. Marbling of the limbs—predominantly on upper arms and legs.
5	Skin on hands/feet starting to slough off. Yellow/green to green/black discoloration on arms and/or legs. Initial skin slippage on arms and/or legs.
6	Degloving of hands and/or feet—exposing large areas of underlying muscles and tendons. Patchy sloughing of skin on arms and/or legs.
7	Exposure of bones of hands and/or feet. Muscles, tendons, and small areas of bone exposed in lower arms and/or legs.
8	Bones of hands and/or feet beginning to disarticulate. Bones of upper arms and/or legs becoming exposed.
9	Complete skeletonization and disarticulation of limbs.

Figure 2.4: Table for the estimation of the LADS (Heaton et al., 2010)

Heaton et al. (2010) also give a relation between TADS and ADD.

$$\mathrm{TADS} = -3.706 + 7.778 \log_{10} \mathrm{ADD} \tag{2.3}$$

Later on, Van Daalen et al. (2017) proposed other FADS, BADS and LADS tables in order to calculate the TADS. These two methods are currently the only way to calculate the TADS of a body. They were compared by Palazzo et al. (2020) who highlighted that the Van Daelen's method is easier to use in practice. However they have the same accuracy and,here, Heaton's method is likely be a better fit because it results from a study made in fresh water while Van Daelen's method is based on both fresh and sea water. Indeed, the decomposition depends on the water salinity and its temperature (Boxho, 2013). Results of the comparison are as accurate when a global TADS-ADD relation is considered but Heaton's method is more accurate when places and water conditions are known precisely.

It is known that human bodies in water follow two stages in terms of vertical motion, depending on their degree of decomposition: sinking and resurfacing (figure 3.8). The sinking phase depends on the morphology of the body, its clothes, circumstances of death, etc. while the resurfacing depends on all the same factors combined with the most important one: the decomposition stage. In any case, the density of a human body is really close to the one of the water in which it lays (Donoghue and Minnigerode, 1977). In this respect, a small modification of its volume or mass induces a modification of the vertical position. This implies that the sinking phase is strongly controlled by the amount of residual air in the lungs, which tends to decrease over time. The resurfacing phase is controlled to a great extent by the generation of putrefaction gases (Boxho, 2013).

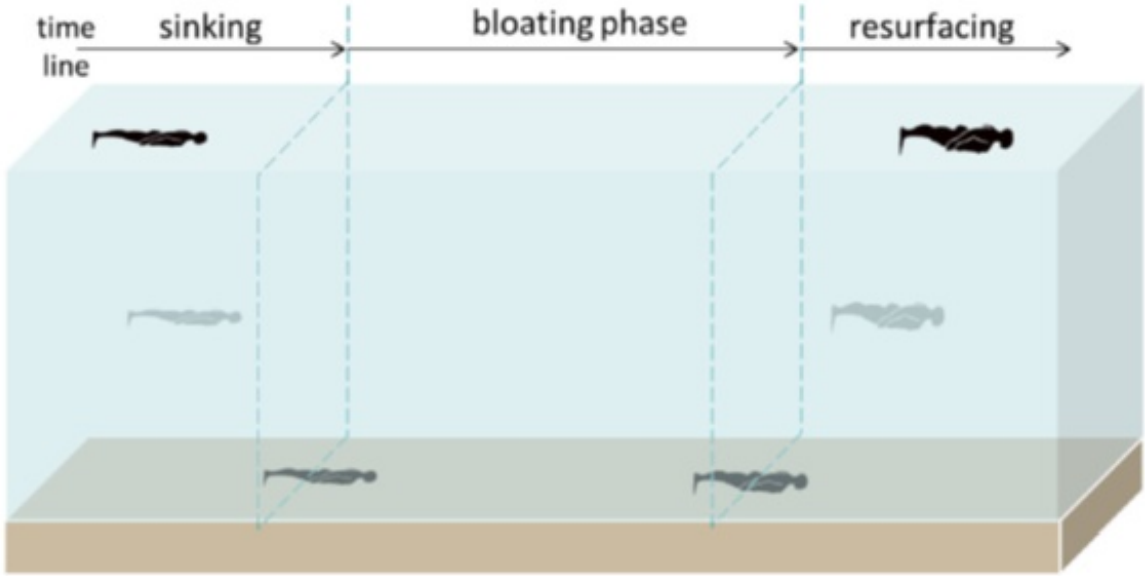

Figure 2.5: Stage of vertical motion (Matheus et al., 2013)

This led to the first attempts of predicting the position of a body over time, as performed by Matheus et al. (2013), Mateus and Vieira (2014) and Heaton et al. (2010). The first two studies followed a similar procedure:

- create a data set with cases of bodies found in water, with known positions of drowning and recovery;
- calculate the ADD for each case;
- calculate the PMSI for each case;
- compare each ADD and PMSI to estimate the time of resurfacing

Studies by *Matheus and colleagues* do not consider TADS in the evaluation of the PMSI. They decided to directly come to the conclusion that in their study area, the PMSI was of 8.6 days for an ADD between 95 and 117. Their analysis is based on two cases of drowning for which the calculated the PMSI and the ADD. One of the two victim had an ADD of 95 and the other one an ADD of 117, their average PMSI was 8.6 days and they extended their results to all cases saying that an common PMSI was 8.6 days and the ADD of resurfacing was between 95 and 117.

However, Heaton et al. (2010) organised their work in a different way:

- create a dataset with cases of bodies found in water, with known positions of drowning and recovery;
- calculate the TADS for each case;
- calculate the PMSI for each case;
- deduce the ADD from the empirical relation previously established with the TADS

$$\mathrm{ADD} = 10^{\frac{(\mathrm{TADS} + 3.706)}{7.778}} \tag{2.4}$$

- compare each ADD and PMSI to estimate the time of resurfacing of a body

The two procedures are used with different goals in mind: the first one attempts to predict the PMSI before the body recovery while the second one attempts to estimate the time of resurfacing of the body thanks to observations on the recovered body (Figure 2.6). Furthermore, those studies focus on the vertical motion while little attention is devoted to the horizontal one. This means that time of resurfacing and PMSI are studied but the position of these points is not known, as well as all the other positions of the body over time.

Figure 2.6: Sketch of the motion of a body in the horizontal plane

Furthermore, these studies do not account for the particular characteristics of each body. Indeed, bodies with different body shapes, clothes, blood alcohol, as well as the kind of flow (turbulence influences the decomposition (Heaton et al., 2010)), etc. are all considered in the same manner. In this respect, the evaluation of the PMSI is often limited to an estimation for an "averaged body". Hence, search operations in practice remain so challenging that some studies recommend to start search operations after a certain time (linked to the ADD) to improve the chances of finding the body because it may have resurfaced. This is of course an undesirable practice.

Moreover, Heaton et al. (2010) pointed to the fact that their method lacks accuracy because of considerable uncertainties on the motion of bodies. Water temperature decreases with depth and turbidity and so the actual ADD may substantially differ from the one estimated. Similarly, when the river is deep, water pressure may be so high that the chest is unable to inflate enough to allow resurfacing to occur. In such cases, sub-aquatic search becomes inevitable. Currently it is not possible to take these processes into account.

In conclusion, lacks of knowledge remain on the determination of the motion of a body in water. Despite existing research on the medical and biological aspects of the motion, large uncertainties affect the predictions.

A study on the two-dimensional motion would be valuable to improve the quality of the TADS-ADD relation and to improve the sub-aquatic investigations. Indeed, decomposition is influenced by the turbulence of the flow, its turbidity, water temperature, etc. and all of them do vary horizontally. An accurate estimation of the motion of the body would lead to more accurate estimations of TADS and ADD and so improve the estimation of the PMSI.

2.2 Floating objects

While previous section focuses on the biological effects of water on a body, in this section the physical interactions between a flow and a body are considered.

Carniel et al. (2002) studied the motion of a body in a marine environment. They focused on body drift at the surface and assumed that the body strictly follows the currents. Vertical motion and differences between water and body velocity were neglected. They simulated the motion of a body by starting from a cloud of hundreds of points positioned randomly around the assumed location of drowning. The motion of each particle was then computed (Figure 2.7) delivering ultimately a map of probability of presence of the body.

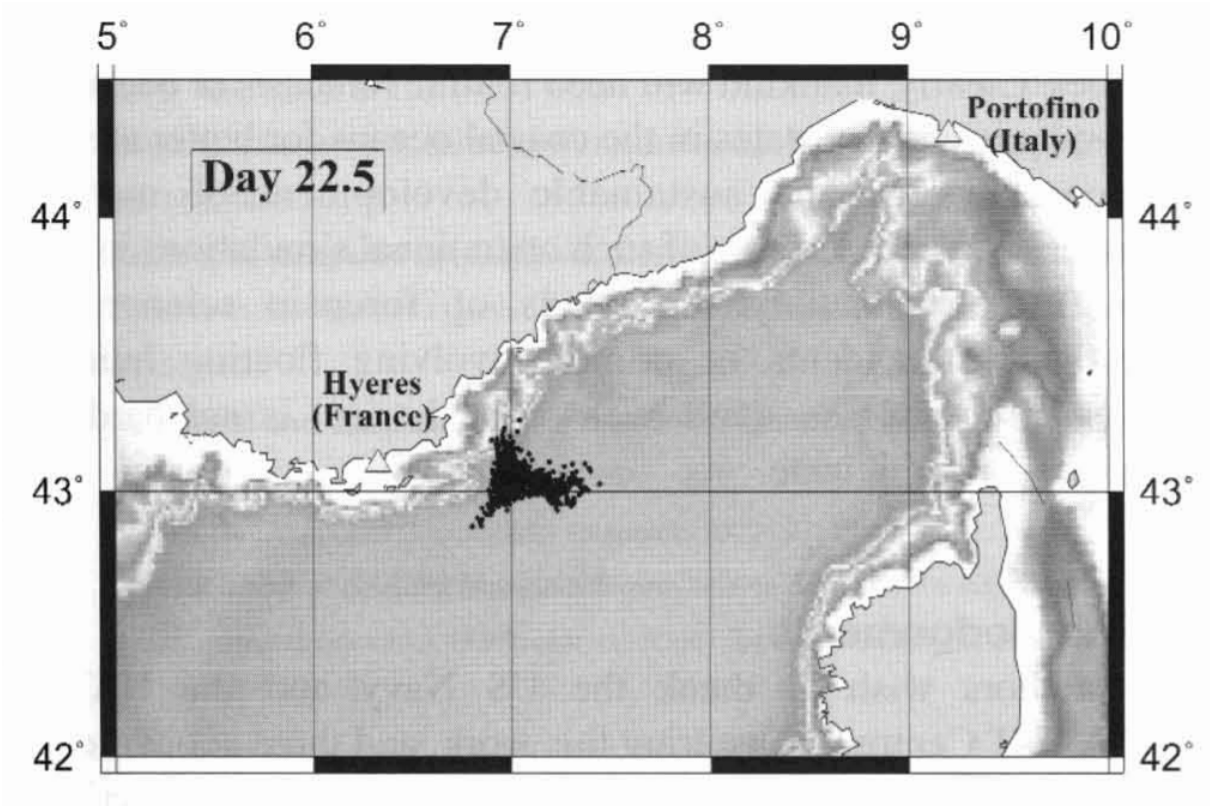

Figure 2.7: Cloud particle after 45 time steps (Carniel et al., 2002)

Several recent works were published about the motion of logs (i.e. tree trunks) in rivers like Braudrick and Grant (2000). All of them assumed simplified shapes, like a cylinder, to model the motion of a log. Studies on this subject become increasingly successful and some analogy with our work is of relevance.

These models couple a Discrete Element (DE) Lagrangian approach for the calculation of the motion of rigid bodies with the Eulerian solution of the shallow water equations (SWE), in order to simulate the transport of a cylinder in a two-dimensional stream. A particularly recent model is based on a dynamic approach, adapting the Basset-Boussinesq-Oseen (BBO) equations (Ghaffarian et al., 2020; Persi et al., 2016, 2019). They all solve similar equations for log motion as Equations 2.5 and 2.6 taken from Persi et al. (2016):

$$(m_b + \frac{1}{2}C_{AM}m_f)\frac{d\overrightarrow{U}_b}{dt} = \frac{1}{2}\rho_w A(C_D + C_S)(\overrightarrow{U}_w - \overrightarrow{U}_b)^2 + m_f(1 + \frac{1}{2}C_{AM})\frac{D\overrightarrow{U}_w}{Dt} \tag{2.5}$$

$$I\frac{d\overrightarrow{\omega}_b}{dt} = \sum \overrightarrow{r} \wedge \overrightarrow{F} + \frac{1}{2}C_{AI}I\left(\frac{D\overrightarrow{\omega}_f}{Dt} - \frac{d\overrightarrow{\omega}_b}{dt}\right) \tag{2.6}$$

$$\frac{d\overrightarrow{X}_b}{dt} = \dot{X}_b = \overrightarrow{U}_b\ ;\ \frac{d\overrightarrow{\theta}_b}{dt} = \dot{\theta} = \overrightarrow{\omega}_b \tag{2.7}$$

with m_b the mass of the body, C_{AM} the added mass coefficient, m_f the mass of the surrounding fluid, $\overrightarrow{U}_b$ the velocity of the body, ρ_w the water density, A the projected/frontal area, C_D the drag coefficient, C_S the side coefficient, $\overrightarrow{U}_w$ the water velocity, I the inertia of the body around *z*, $\overrightarrow{\omega}_b$ the angular velocity of the body, $\overrightarrow{r}$ the distance between the force and the centre of mass, $\overrightarrow{F}$ the applied force, C_{AI} the added inertia coefficient, $\overrightarrow{\omega}_w$ the angular velocity of the fluid, $\overrightarrow{X}_b$ the position of the body, and $\overrightarrow{\theta}_b$ the orientation of the body.

The coefficients involved in Eq. 2.5 are known for simple, standard shapes.

These equations are solved in an explicit resolution assuming a linear acceleration over one time step. Software like *ORSA2D_WT* are already working on this basis and show a good agreement with laboratory experiments realised under controlled conditions. For instance, figure 2.8 shows results of such experiments reported by Persi et al. (2019), where the numerical log motion is displayed in blue.

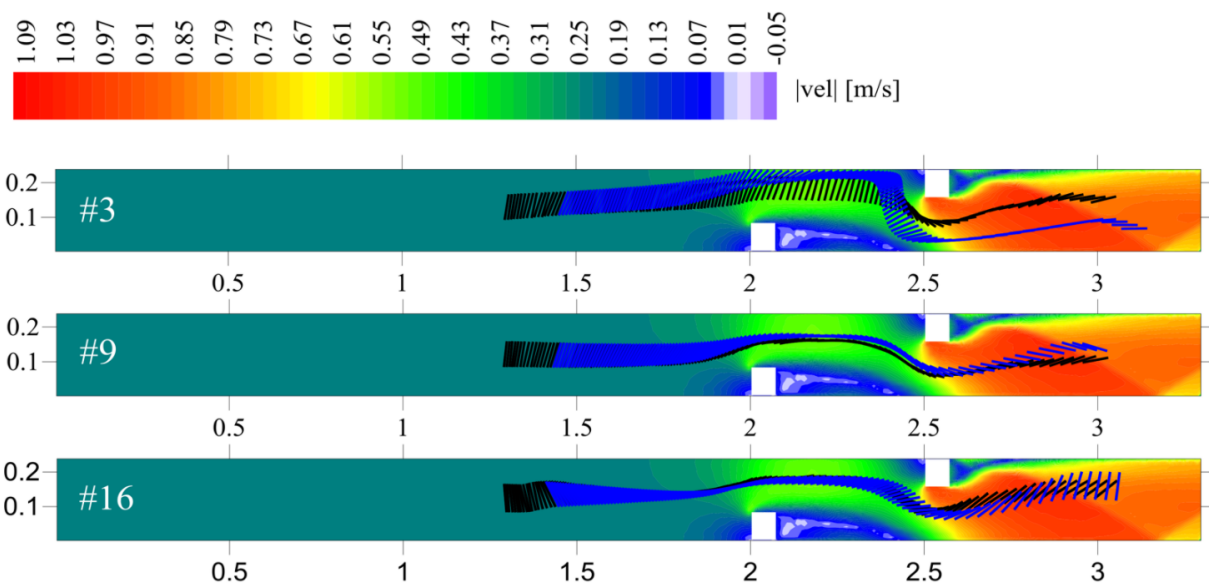

Figure 2.8: ORSA2D (Persi et al., 2019)

Ghaffarian et al. (2020) also realised a study on large moving shapes at the water surface (figure 2.9). This work differs from the previous one because it tests shapes of different materials. Indeed, comparisons between computations and the experimental observations were presented in Persi et al. (2016) but the comparisons between identical shapes of different materials is also considered. This reflects the variety of existing studies on moving logs in uniform or non-uniform flow.

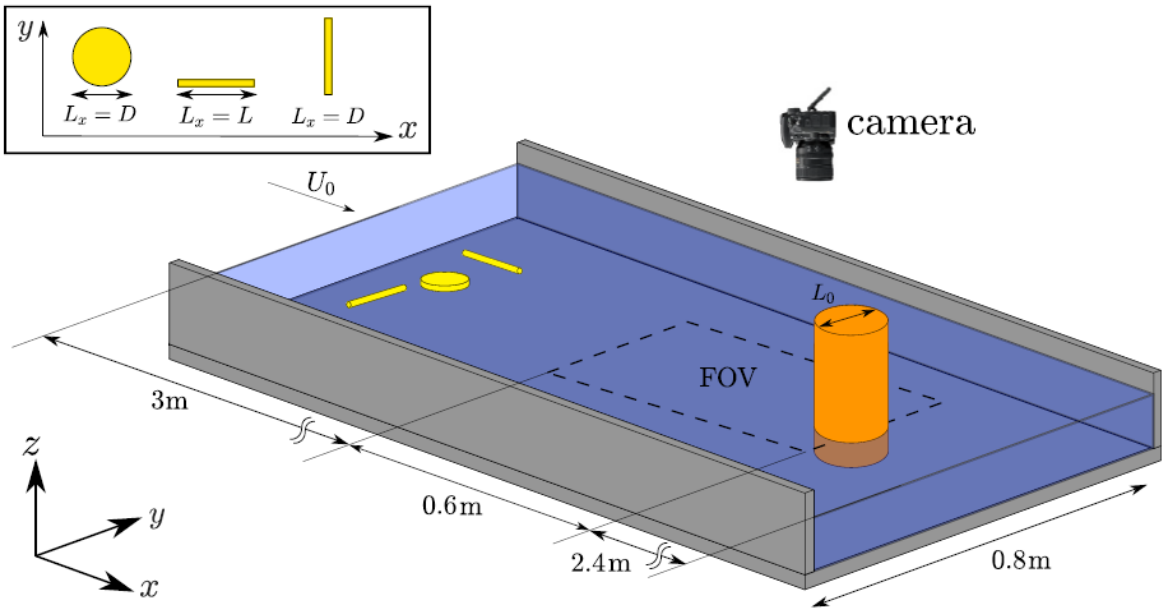

Figure 2.9: Initial situation of *Ghaffarian*'s study (Ghaffarian et al., 2020)

The inception of motion of logs was also studied, such as by Braudrick and Grant (2000). This motion is similar to the initiation of bed load transport and could be adapted to a human shape.

Overall, computational predictions are fairly close to the reality when simple shapes in a non-uniform flow are considered. In addition, knowledge on the motion of particles on the bottom of the river could serve as a basis for modelling the motion of the body when it is in contact with the river bottom.

2.3 Objectives of this work

So far, most studies focused on the biological processes directly influencing the vertical motion of a body in water. Less attention has been given to the horizontal drift of a victim of drowning, particularly in rivers. Conversely, the drift of objects of simple shapes, such as cylinders, is another research topic which is fairly advanced (Persi et al., 2016).

The present master's thesis is a contribution to initiate research efforts aiming at developing a 2D/3D model for predicting the motion of victims of drowning in urban rivers. As a first stage, it is relevant to investigate the possible transposition of existing computational models for reproducing the drift of rigid objects such as logs, to the case of human bodies. To do so, we start from a formulation like Eq. 2.5, in which the values of the coefficients (added mass, drag and side coefficients) are relatively well known for objects of simple, standard shapes; but this is not the case for human bodies in various positions. Only the case of a swimmer was analysed in literature, and the investigations were mostly restricted to the drag coefficient (Bixler et al., 2007).

A specific objective of the present thesis is to investigate the possible range of values taken by the drag coefficient in the case of a victim of drowning. Therefore, a plausible positioning of the human body in water was identified and experiments were conducted in a laboratory flume based on three distinct 1:6 scale models (dummies). Tests were also performed with a prototype scale dummy in a towing tank. The tested parameters include the relative velocity between the dummies and water, the orientation of the dummies with respect to the flow, the submersion depth, as well as the effect of clothes. The outcomes of these experimental observations were plugged into a simple computational model of drift of a human body in water. Finally, based on the findings of our analyses, outlooks for subsequent steps of the research are formulated.

3 | Experimental modelling

Experimental tests were performed in two separate facilities: a laboratory flume and a towing tank. In this chapter, we describe the experimental setups, the models used (dummies), the test procedures, the measurement devices and the obtained results.

3.1 Laboratory flume

3.1.1 Experimental setup and flow characteristics

A 20-m long laboratory tilting flume installed at the Laboratory of Engineering Hydraulics of ULiege was used to perform a first series of experiments. The flume is 0.5 m wide and ≈0.8 m high. In all the tests conducted so far, the flume bottom was set in horizontal position (no slope).

Considered as rigid, the body models used here have six degrees of freedom as they move in the flume(besides the positioning of the limbs) : three in translation and three in rotation. The corresponding positions are defined as follows (Figure 3.1):

- x: streamwise position along the main flow direction
- y: crosswise position in the plane aligned with the main flow stream and parallel to the flume bottom
- z: elevation along the direction normal to the flume bottom

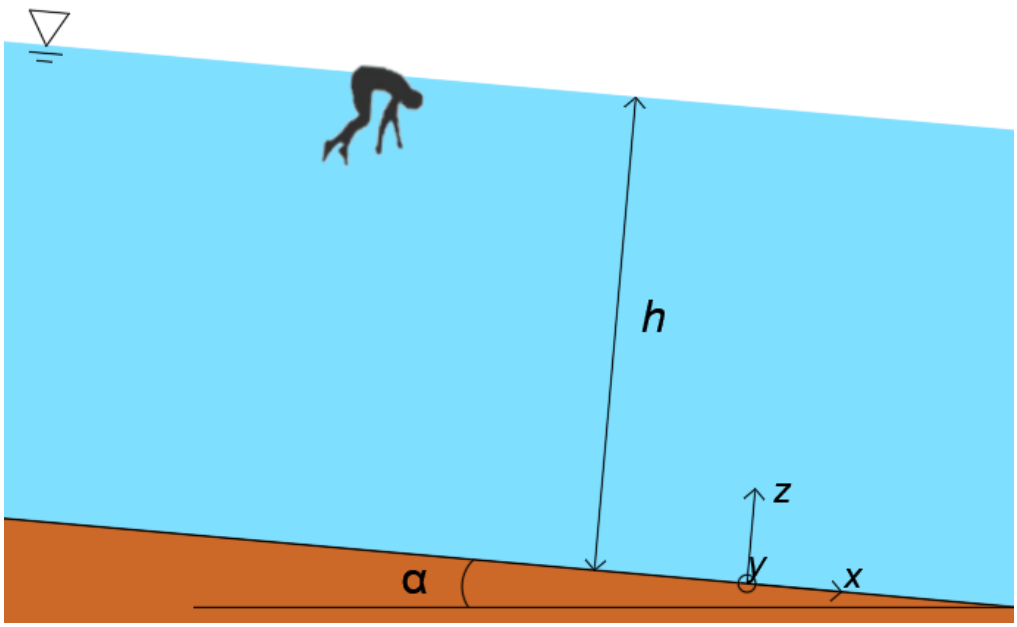

Figure 3.1: Scheme of the situation, *xz* plan

The three angles defining the orientation of the model are shown in Figure 3.2.

- ϕ: the angle position of the body in the *xz* plane, corresponding to the pitch rotation (*tangage* in French)
- ψ: the angle position of the body in the *yz* plane, corresponding to the roll rotation (*roulis* in French)
- θ: the angle position of the body in the *xy* plane, corresponding to the yaw rotation (*lacet* in French)

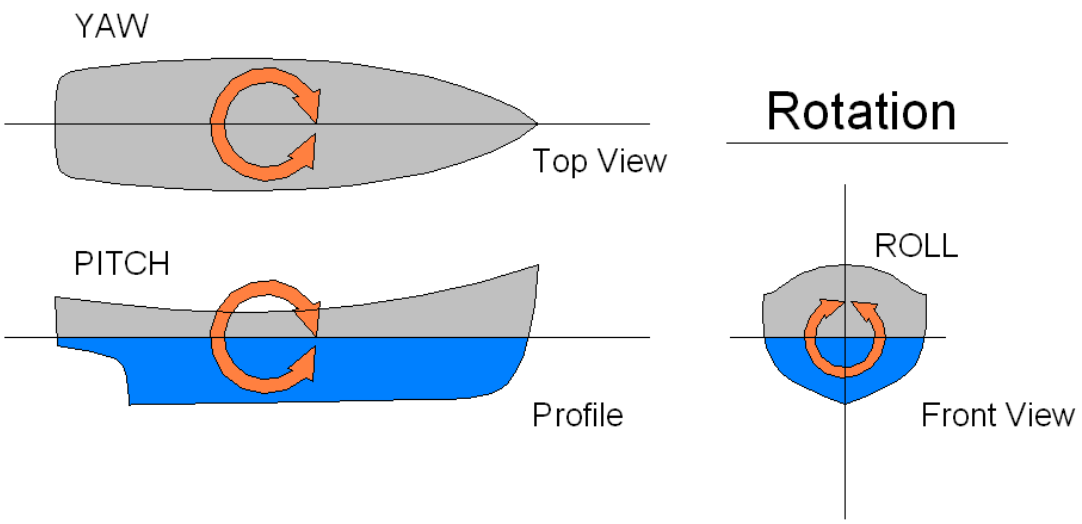

Figure 3.2: Angles defining the orientation (Wikipédia, 2021)

For the yaw rotation, a reference position for which $\theta = 0^o$ was defined. It corresponds to the head downstream and feet upstream, the main direction of the body aligned with the the main flow direction. Figure 3.3 displays a plane view and shows that the conventional trigonometric direction is used to characterise the body yaw rotation.

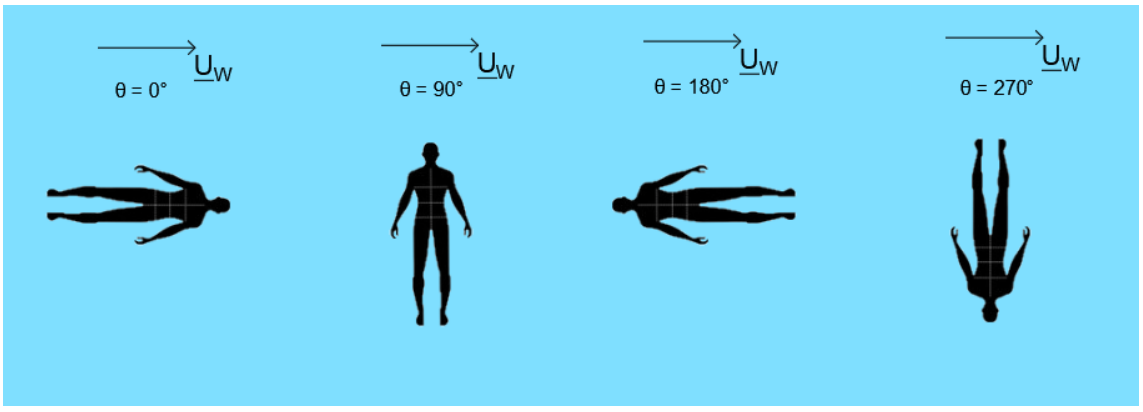

Figure 3.3: Yaw rotation

Origins of the axes in this flume are defined by:

- *x = 0*: the upstream end of the flume
- *y = 0*: the left edge of the flume when looking downstream
- *z = 0*: the bottom of the flume
- θ *= 0*: the position with the head-legs axis of the model aligned with the flow, head downstream (Figure 3.3)

The origin of the *z* axis is conventionally set here at the bottom of the flume while in some articles it is defined at the surface.

For all the tests, the flume was fed with a steady inflow discharge Q, ranging between 30 l/s and 55.7 l/s. A constant flow depth was prescribed at the downstream end of the flume of width $l = 0.5$ m. In the following paragraphs, we estimate the non-dimensional parameters characterising the flow in the flume, namely the Froude number Fr and the Reynolds number Re.

In a flume of rectangular cross-section, the Froude number Fr is calculated as follows:

$$Fr = \frac{U_{mean}}{\sqrt{gh}} \tag{3.1}$$

with:

- $U_{mean} = \dfrac{Q}{h * l}$ $[m/s]$, the cross sectional average velocity,
- $g = 9.81$ $[m/s^2]$, the gravity acceleration,
- $h =$ flow depth $[m]$

The flow depth variations in space are not visible with the naked eye in the flume (the free surface looks horizontal). Indeed flow velocity is very low ($U_{mean} \approx 0.1$ m/s) and so the variations of water depth along the flume remains limited. Furthermore, all measurements have been made at *x* = 16.65 m where the flow depth is very close to 62 cm and the flow is as little disturbed as possible.

Flow depth was measured with a mechanical limnimeter at the downstream and upstream end of the flume and at the position of measurement, for both maximum and minimum discharge. Each flow depth has been measured to 62 cm at the precision of the mechanical limnimeter. This is the reason why flow depth will be considered to be constant at $h = 0.62$ m in this whole chapter.

The range of Fr in the flume can now be plotted in Figure 3.4.

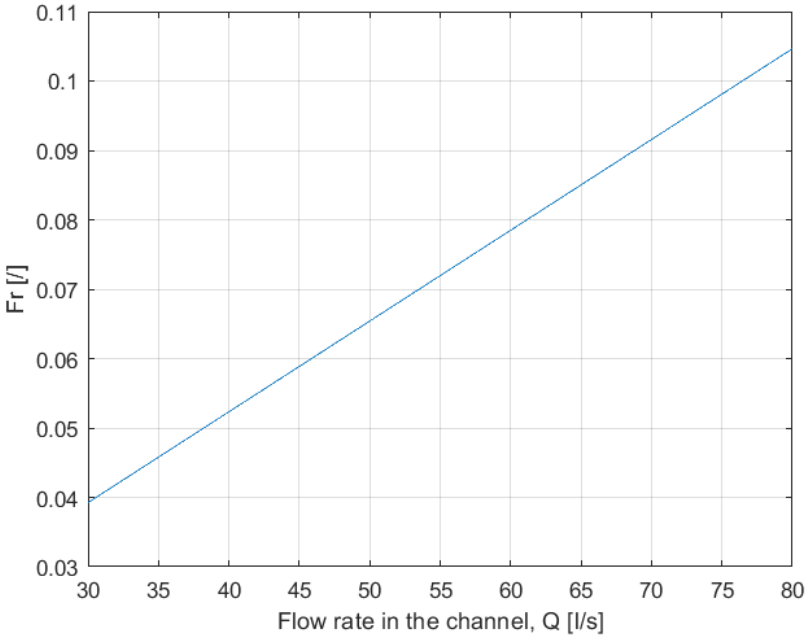

Figure 3.4: Froude number for all Q and $h = 62\ cm$

Two type of Reynolds numbers may be distinguished in the considered setup: on one hand the flow Reynolds number Re, and on the other hand the particulate Reynolds number Re_p. The former is based on the flow velocity and a characteristic length of the flow (e.g., hydraulic radius), whereas the latter is based on the relative velocity between water and the body models as well as on a characteristic length of the body models (e.g., its size).

The Reynolds number at the surface of the flow in the flume enables describing the turbulence regime. It is defined as follows:

$$Re = \frac{4U_{mean}R_H}{\nu} \tag{3.2}$$

with:

- Ω, the cross-section area
- P, the wet perimeter of the cross-section
- $R_H = \frac{\Omega}{P}\ [m]$, the hydraulic radius
- $\nu = 10^{-6}\ [m^2/s]$, the water kinematic viscosity at 20^oC

In our experiments, the range of Re at the surface of the flow in the flume is:

$$Re_{min,surf} = \frac{4 * 0.09677 * 0.1781}{10^{-6}} = 68,960 \tag{3.3}$$

$$Re_{max,surf} = \frac{4 * 0.1797 * 0.1781}{10^{-6}} = 128,000 \tag{3.4}$$

The Reynolds number Re of the flow is defined in equation 3.5.

$$Re = \frac{U_{mean} R_H}{\nu} \tag{3.5}$$

The range of Re in the flume is:

$$Re_{min} = \frac{0.09677 * 0.1781}{10^{-6}} = 17,240 \tag{3.6}$$

$$Re_{max} = \frac{0.1797 * 0.1781}{10^{-6}} = 32,000 \tag{3.7}$$

The particulate Reynolds number is defined based on the height L of the body model.

$$Re_p = \frac{U_{mean} L}{\nu} \tag{3.8}$$

A human body is not rigid (conversely to the body-models) and so the length of separation of the boundary layer is not known. For simplicity, the maximum possible length, i.e. the size of a standing body model, was considered here, although if in our experiments the body models are not in a standing position.

3.1.2 Body models characteristics

3.1.2.1 Identification

Three body models at scale 1:6 were used in the experiments. As shows in Figure 3.5, they are referred to as (a) Hagrid, (b) Bruce and (c) Charlie. Each model shows particular features compared to the others. Hagrid is more corpulent than the others and has hair, Bruce is in shape with no real hair while Charlie is thin with hair (Figures 3.5 and 3.6).

The added-value of using three different models lies in the opportunity to compare various parameters, such as body shapes and presence or absence of hair. The three body models have articulated limbs which enables adjusting their position.

(a) Hagrid (b) Bruce (c) Charlie

Figure 3.5: Identification of the models

Figure 3.6: Models side-by-side

3.1.2.2 Volume, mass and length

The volume of the models was measured with a graduated container filled with 4.5 L of water at an ambient temperature of about 20^oC. Each model was put inside the container just after getting the model out of the flume. The model has to be out of water for the lowest possible time to avoid water loss. Indeed the body models are hollow, with some holes allowing water to enter the body. The variation of volume has to be determined with a filled model for the sake of consistency with the conditions in which the experiments were conducted.

The volume of the filled model is simply evaluated as the difference between the volumes of water read on the container with and without the body in it (Figure 3.7).

The mass of a filled model is determined by weighting the container with and without the body and taking the difference of the two measured values of mass.

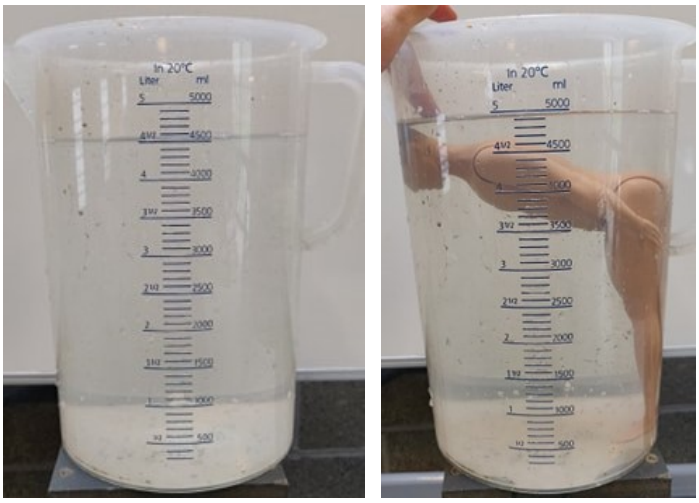

(a) Reference (b) Measurement of ΔV

Figure 3.7: Measurement of the volume

The lengths of the different parts of the body were measured by hand on the models (see section 3.1.2.4).

3.1.2.3 Body position

As this work is one of the first to study the drift of a drowned human body in water with considerations for the body's position and orientation, an assumption on the studied position needs to be formulated. In contrast, previous research such as by Carniel et al. (2002) or Matheus et al. (2013) studied body drift the marine currents with a pointwise approximation of the horizontal motion for the first research or a pointwise approximation of the vertical motion for the second one.

In contrast to what was schematised by Matheus et al. (2013) in Figure 3.8, the investigation is made considering that a body does not stay perfectly straight. Literature on forensic medicine and lung capacity have been browsed and tentative of interpretations could be reached (Bern, 2021; Boxho, 2013).

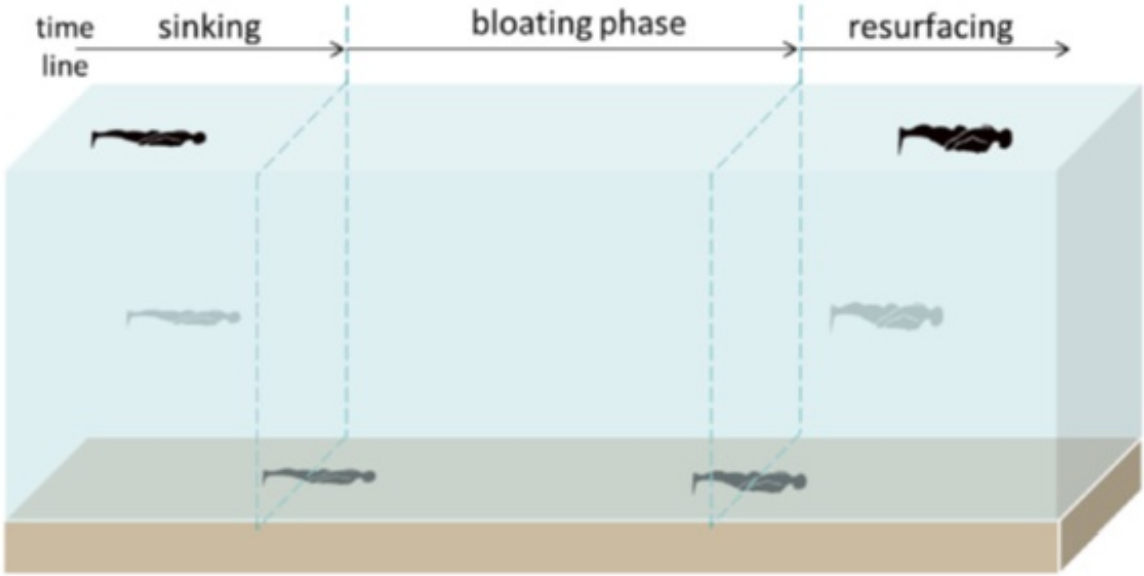

Figure 3.8: Body position considered in literature (Matheus et al., 2013)

The period of interest is the time just after the death (when $t > t_0$, with t the time and t_0 the time of the last heartbeat). At this moment blood pressure tends to decrease to zero and blood accumulates in lower parts of the body. This is called the hypostasis phenomenon. That means that blood which was in the chest and legs goes down in the feet while blood of the arms goes down in the hands and the one in the head stays in the head or goes down in the feet. For a common people, the lung capacity is of about 3.5 to 4 L (Bern, 2021). Studies on human buoyancy state that most of the time when all the air is blown out of the lungs, the body tends to sink while it float when the lungs are full of air (Donoghue and Minnigerode, 1977). However all the air can not be blown out of the lungs and about 1 L of air remains inside (Bern, 2021). That means that the vertical motion is controlled by the buoyancy of about 2.5 L of air. Indeed, even in a case of drowning with the people respiring water, about 1 L of air remains inside the lungs and makes the chest density lower than that of the rest of the body. Matheus et al. (2013) pointed to the fact that water could be swallowed and the chest would become heavier; but this aspect was not accounted for here for formulating an assumption on the body position. The amount of swallowed water is assumed small; but this should be further analysed in subsequent research.

Heymsfield et al. (2007) report that the head density is higher than the one of the rest of the body, and the head is located the furthest from the centre of mass, situated near the navel (Wieczorek et al., 2021).

According to the estimated relative densities of each part of the body, in the experiments, the body position is assumed with limbs hanging down and the chest close to the surface, as sketched in Figure 3.9, and various orientations were tested (Figure 3.10, flow direction schematised by the blue arrows):

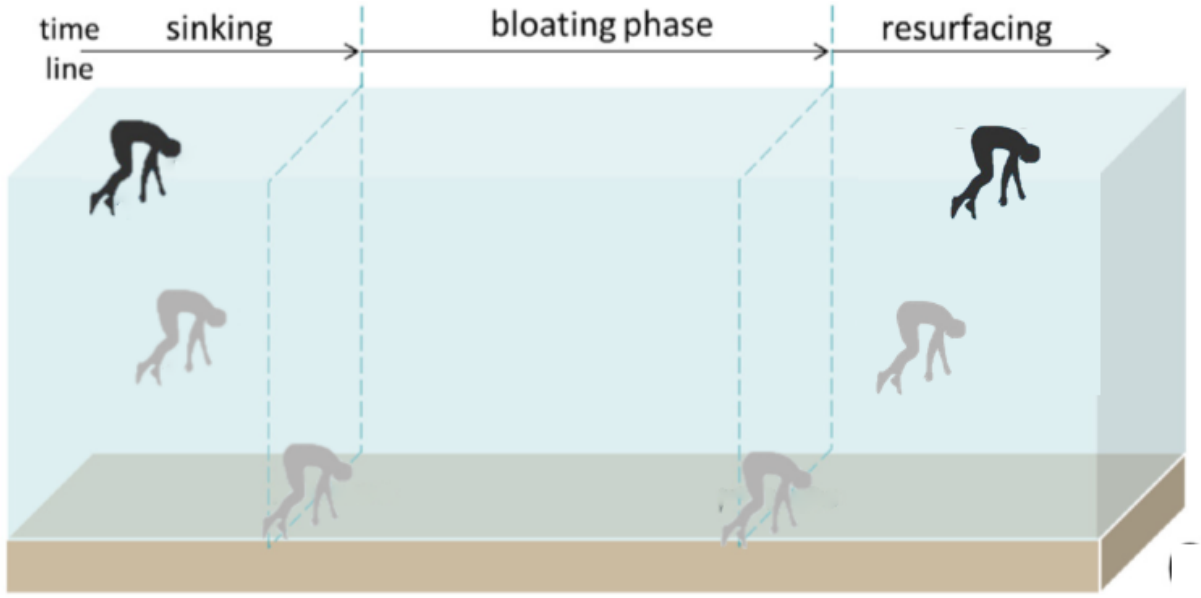

Figure 3.9: Body position as assumed in the experiments (modified from Matheus et al. (2013))

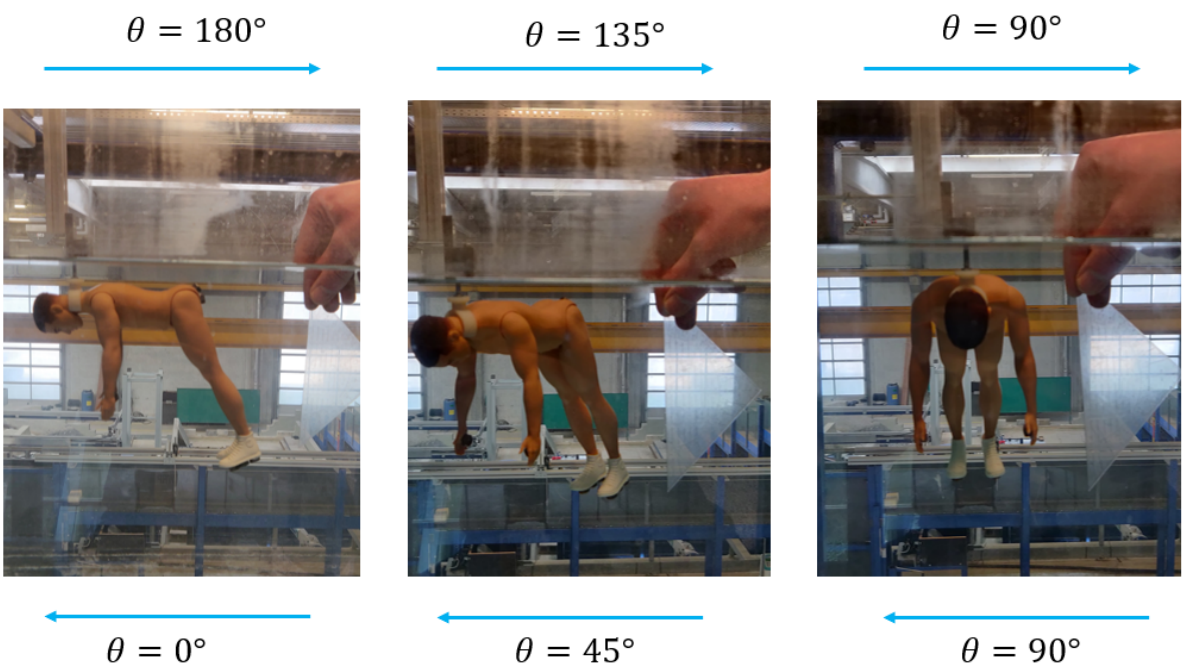

Figure 3.10: Position and orientation of models in lab

3.1.2.4 Determination of the frontal areas

The frontal areas of each body model for each studied yaw angle was determined with the image processing software *ImageJ*. A procedure which was repeated for each case is detailed below.

First, dimensions of a well known object were measured to check the distortion of the picture. A set square with a basis of 16 cm and a height of 8 cm for an area of 64 cm^2 is used as a reference. This set square is present on each picture at the same distance from the camera as the middle of the body model.

The procedure is the following:

1. take a picture of the model in landscape format;
2. take a picture of the model in portrait format;
3. take the first picture and surround the set square to determine the number of pixels to have 64 cm^2;
4. surround the model by hand (Figure 3.11) on the same picture twice and write the number of pixels;
5. repeat point 3 and 4 with the picture in portrait format;
6. take the average area of the model with the fixed yaw angle with the following formula in cm^2 with np = number of pixels:

$$A_p(\theta) = \sum_{i=1}^{4} 64 \frac{np_{model,i}}{np_{set\ square,i}} \tag{3.9}$$

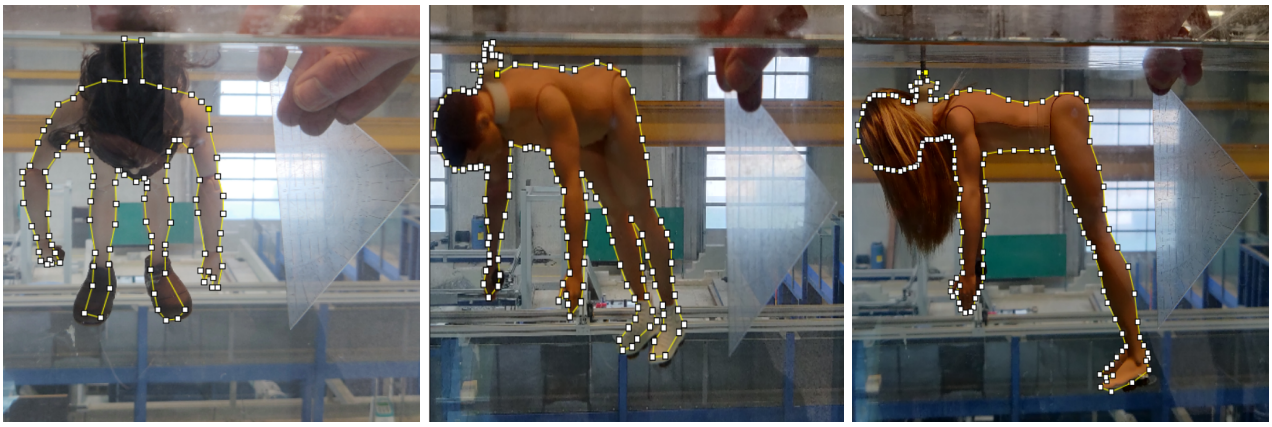

Figure 3.11: Surrounding of the models made by hand

3.1.2.5 Summary of model characteristics

All the characteristics mentioned in this section are the characteristics of a model filled with water. All the experiments are realised with this kind of model and so they are the only ones detailed.

The volumes, mass and bulk density of each models are presented in Table 3.1:

Model	Mass [g]	Volume [L]	Bulk density [kg/m³]
Hagrid	453 ± 1	0.54 ± 0.05	838.9 ± 87.6
Bruce	317 ± 1	0.485 ± 0.05	653.6 ± 77.4
Charlie	289 ± 1	0.32 ± 0.05	903.1 ± 167.3

Table 3.1: Volume, mass and volumic mass of each model

Accumulation of uncertainties lead to a relatively poor approximation of the bulk density. However, these results are not used for calculations of this work and deserve only to have a number in mind.

The length L from the top of the head to the base of the feet of each model, their width of shoulders l and the thickness of their chest e. Table 3.2 and Figure 3.12 summarise these length..

Model	L [cm]	l [cm]	e [cm]
Hagrid	30.5	8.7	5.8
Bruce	29	8.5	4
Charlie	29.5	7.8	3.5

Table 3.2: L, l and e of each model

Figure 3.12: Main dimensions of a body

Finally the length L and average diameter D of their arms, legs and head are detailed in Table 3.3.

(a) Arms

Model	L [cm]	D [cm]
Hagrid	10	1.3
Bruce	12.1	1.6
Charlie	10.5	1.2

(b) Legs

Model	L [cm]	D [cm]
Hagrid	15.4	1.6
Bruce	13.2	2.1
Charlie	15.1	1.5

(c) Head

Model	L [cm]	D [cm]
Hagrid	4.5	5.8
Bruce	4.6	4
Charlie	4.7	3.5

Table 3.3: Limbs dimensions

The most important one is the frontal area of each model for each studied yaw angle. Indeed, it is the only one which has a direct impact on the determination of the drag coefficients. Table 3.4 and Figure 3.13 present the measurements carried out with the procedure detailed in section 3.1.2.4:

Model\Orientation	0°	45°	90°	180°
Hagrid	76.01	113.65	144.93	76.01
Bruce	85.17	127.78	118.83	85.17
Charlie	82.29	117.45	109.5	82.29

Table 3.4: Frontal area of the models in cm^2

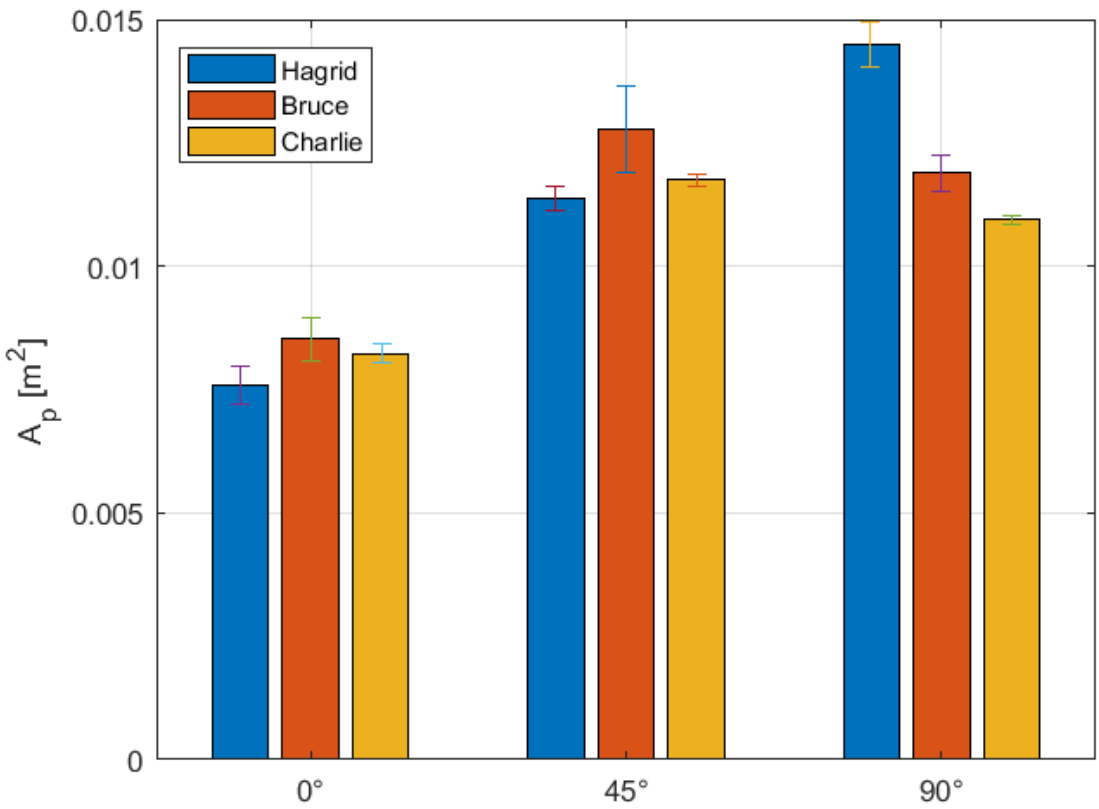

Figure 3.13: Frontal area of each model

A relevant point is that uncertainties are not linked to the position or the model.

However, two inconsistencies are seen in these table and graph: Hagrid's frontal area is lower than those of Bruce and Charlie at a yaw angle of 0° and 45°. The explanation is that Hagrid is not perfectly horizontal. His buttock is higher than his head and so a part of his body is hidden by his head and beard. Furthermore, at 45°, Hagrid has one of his arms aligned with one of his legs which is not the case for the two other models (Figure 3.14). This alignment results in an apparent decrease of the frontal area in the plane in which they are aligned.

(a) Hagrid $\theta = 45^o$ (b) Charlie $\theta = 45^o$

Figure 3.14: Models at $\theta = 45^o$

3.1.3 Measurement devices

3.1.3.1 Determination of the cross sectional velocity profile

The cross sectional velocity profile is determined thanks to the Acoustic Dopler Velocity Profiler (ADVP), the Vectrino Profiler (Figures 3.15 and 3.16). The ADVP operating principle is the following one: a pulse is transmitted from the centre transducer, and the Doppler shift introduced by the reflections from particles suspended in water, is picked up by the four receivers (Duma, 2010).

Figure 3.15: Scheme of the ADVP (Duma, 2010)

Each acoustic transducers must be submerged during data collection to get the best data. Another improvement of the conditions to have good results is that the main flow direction must be perpendicular to the transmit axis, the red receiver. Data is collected at a sampling rate of 100 Hz during 80 s on a cylinder of 2 cm height situated between 4 and 6 cm under the transducer (Duma, 2010). Cylinders are divided in 11 cells for which data are collected. That means that one data set is composed of $100*80*11 = 88,000$ values for each measured parameter. They are then averaged, with the outliers previously removed. This average of each collected velocity is considered as an approximation of the flow velocity at the point of interest.

Water profiles in the flume have been determined for the minimum and the maximum water discharge of the experiments. Measurements have been made with the ADVP fixed in height with a displacement of 1 ± 0.1 cm along flume's width between each measurement.

A second measurement is realised to analyse the variation of water velocity in height. These data have been collected following a similar procedure. The ADVP is placed at the centre of the flume and moved with a height step of 2 ± 0.1 cm.

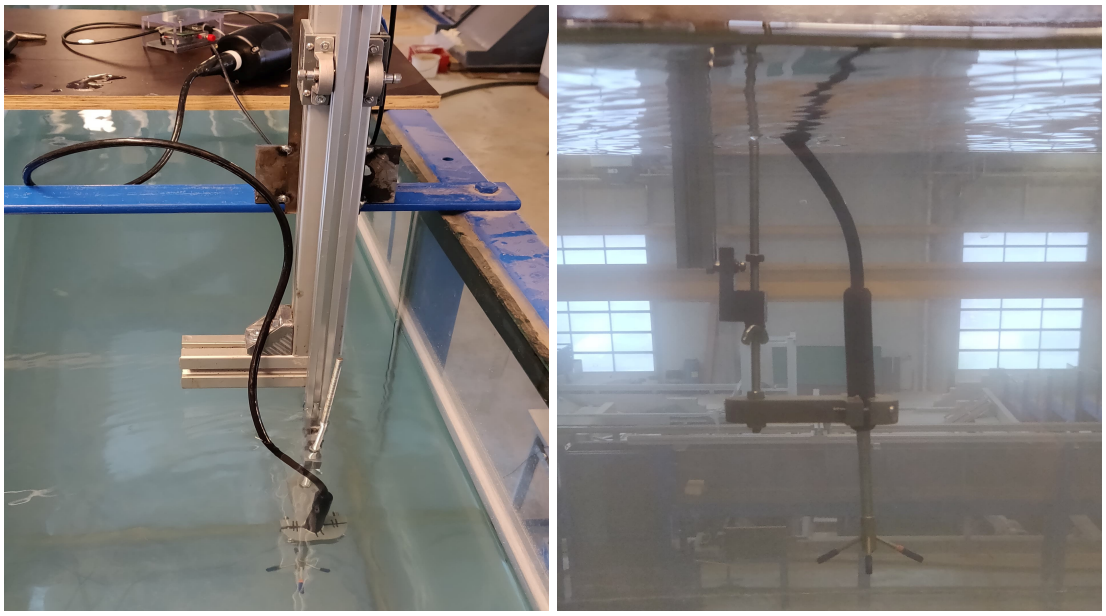

Figure 3.16: ADVP in the flume

A three-dimensional velocity is obtained for each sample. However, only the component along the main flow direction is kept due to the low level of other velocities. Indeed, cross-wise velocities are between 0 and 1 cm/s at maximum. These are considered small compared to the velocity in the streamwise direction.

The sampling conditions are the following one: flow depth in the flume is 62.5 cm at rest and 62 cm for each discharge. Measurements are taken at exactly $x = 16.35$ m.

The results are shown in section 3.3.1.

3.1.3.2 Measurement of drag with a Re_p between 10^4 and 10^5

First measuring system

The measuring system consists in a lever arm to which the model is hooked by the neck at one end and to the strain gauge force transducer at the other end. The analogue signal from the strain gauge is then amplified and converted into a digital signal via an analogue-to-digital converter (Figure 3.17). In our case, it has been decided to put the no-load value to 600. An increasing force decreases this digital value. This system registers has a sampling frequency of 20 Hz and records during 20 s for each experiment. This provides a time series of 401 values to analyse for each test.

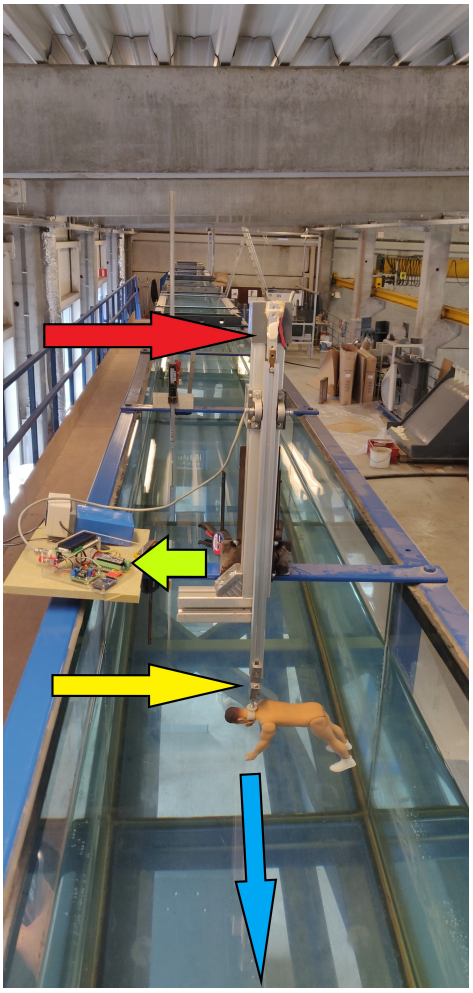

Figure 3.17: First measuring system

- Red arrow: Strain gauge force transducer
- Green arrow: Digital converter and reading of the digital signal
- Yellow arrow: Model tie
- Blue arrow: Direction of the main flow stream

The system has then been calibrated for each kind of strain gauge and each length of lever arm. Indeed, two strain gauges have been used: one with a maximum measurable weight of 5 kg and one with a maximum measurable weight of 1 kg but a better accuracy. The lever arm has been changed too to evaluate the influence of depth on the drag measurement.

The calibration is done as follows: a string is hooked at the end of the tie and passes through a pulley to convert the vertical force into an horizontal one. A known mass is then put at the end of this string and the read number on the digital converter gives the value corresponding to a known force (Figure 3.18).

Figure 3.18: Calibration method

A linear regression with each set of points can then be derived and an equation linking the read number and the applied force is obtained (Figure 3.19 and Table 3.5).

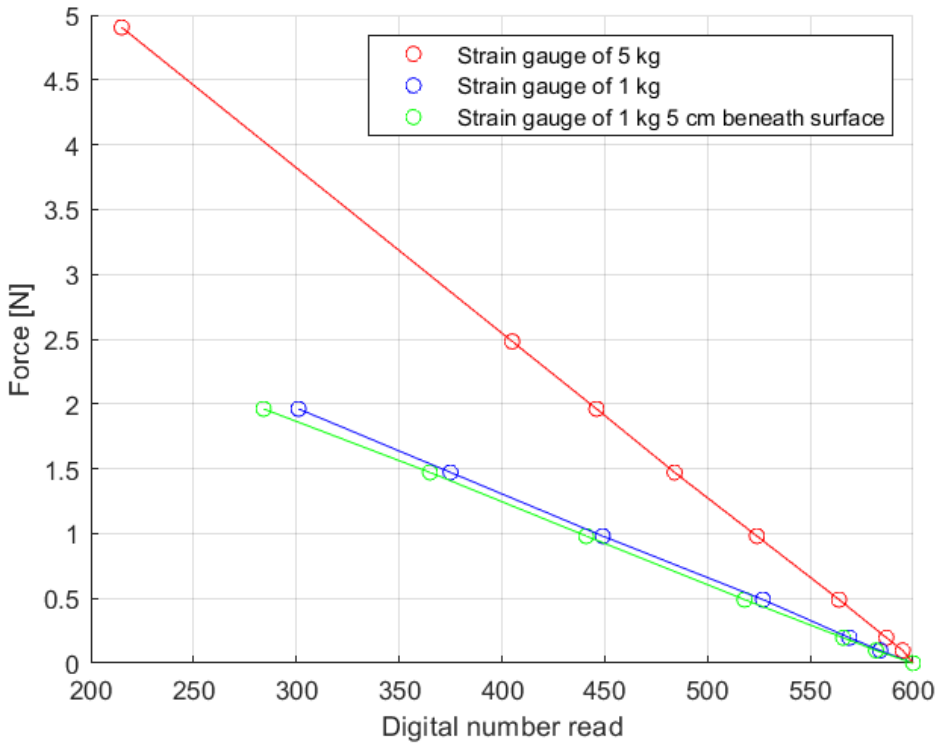

Figure 3.19: Calibration results

The equations of the different regressions are shown in Table 3.5:

Kind of strain gauge - depth	Equation	Correlation coefficient R^2
5 kg - at the surface	F [N] = -0.0127 x + 7.6177	0.9999
1 kg - at the surface	F [N] = -0.0066 x + 3.9339	0.9999
1 kg - 5 cm beneath surface	F [N] = -0.0063 x + 3.7448	0.9999

Table 3.5: Equations resulting of the calibration

The problem arising with this system of measurement is its sensitivity to variations of the ambient electric field. This variability in recorded data is shown on one set of measurements (Figure 3.20).

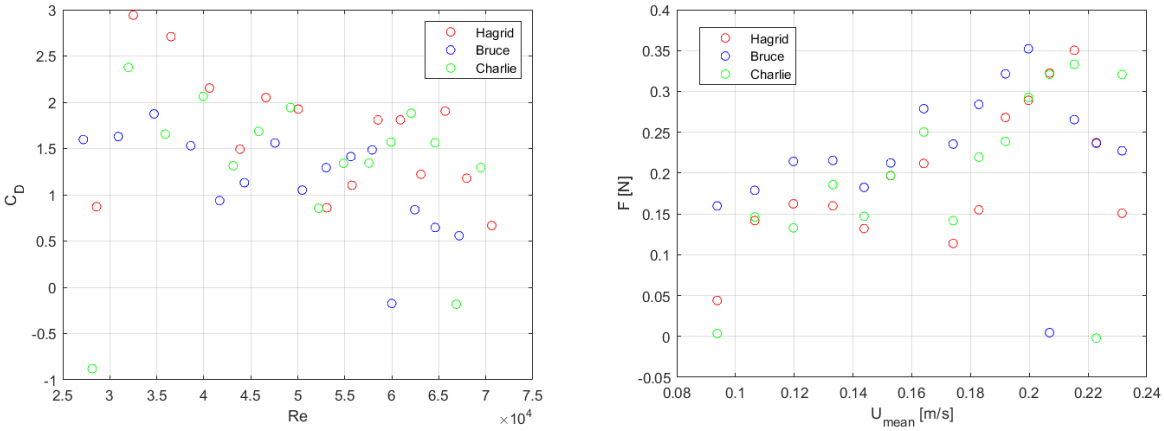

Figure 3.20: First system of measurement, $\theta = 180^o$, variable/unstable

Results are not stable enough to deduce any coefficient.

A solution to reduce the variability is to do the experiments in a stable electric field. A second set of experiments was made with absolutely no movement around the measuring system during the recording: the operator remained immobile next to the setup. Following results are obtained with this change (Figure 3.21).

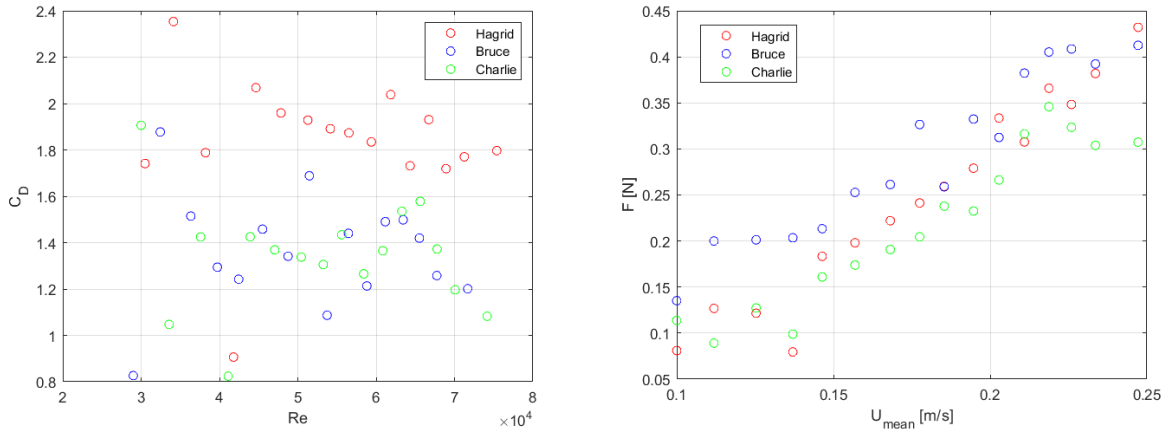

Figure 3.21: First system of measurement, $\theta = 180^o$, stable

This little modification in the experimental procedure lead to substantial improvements in the results and proves that the main problem was identified. However results were still too unstable to be analysed and the system had to be changed.

Second measuring system

The second measuring system works in exactly the same way as the previous one, except that the analogue-to-digital converter is now placed just next to the gauge. This modification greatly reduces the sensitivity of the system to variations of the electric field. This second system is not able to register data at the same frequency as the first one. It registers 401 values in about 36 s which means a sampling frequency of about 11.11 Hz with this system.

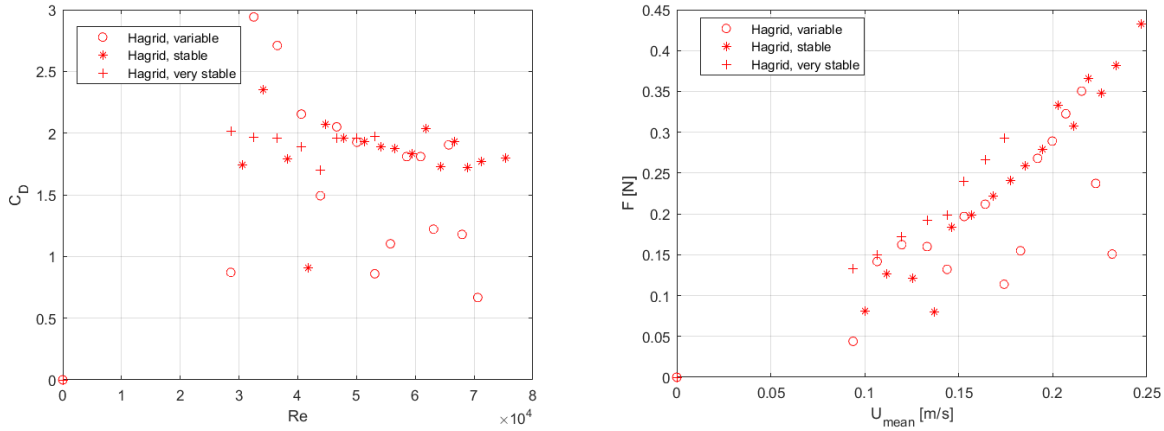

Figure 3.22: Comparison between kinds of measurements for Hagrid at $\theta = 180^o$

Results are more stable with the second measuring system (Figure 3.22) and the analysis is realised on these ones instead of those obtained with the first system of measurements. Results of each experiment are available in Appendix .1, .2, .3 and .4, and the most relevant ones are detailled in section 3.3.2.

Measurement procedure

The system registers data at a frequency 11.11 Hz during 36 s. These frequency and sampling duration are studied in section 3.3.2 and are adjusted to ensure the convergence. The procedure followed for each experiment is the following:

1. Start the pump at the minimum head of 1,5 m/m
2. Wait for 10 to 15 min to let the flow stabilise
3. Fix the position of the tie to a determined angle
4. Fix the first model to the tie by the neck, face down and with his arms and legs as vertical as possible
5. Start the measurement
6. Wait for 36 s to have the measurement done
7. Repeat the points 4 to 6 with the second and third models
8. Increase the head pump by 0,5 m/m
9. Let the flow stabilise
10. Repeat points 4 to 9 up to the maximum pump head

The choice of a head step instead of a speed step is justified. Indeed, first measurements and studies previously realised on simple shapes (Chu et al., 2018; Hölzer and Sommerfeld, 2008; Yang et al., 2015) conclude that drag coefficient is on a level for all the tested Re. The kind of spacing between each measurement has so no influence on the shape of the measured force. As only the head pump could be managed and then the discharge is read, it has been decided to proceed by head step for the sake of ease.

3.1.3.3 Measurement of drag at $Re = 0$ and lower R_p

The motivation for setting up this system was to reach lower relative velocity between the flow and the body (i.e. beneath the limit imposed by the minimum discharge of the pumping system), and hence lower particulate Reynolds Re_p. The automatic transverse system moves at a controlled velocity over the flume, carrying the body model, and the force induced by the relative motion between water at rest and the moving body model can be measured, so that in principle a corresponding drag coefficient may be calculated (Figure 3.23).

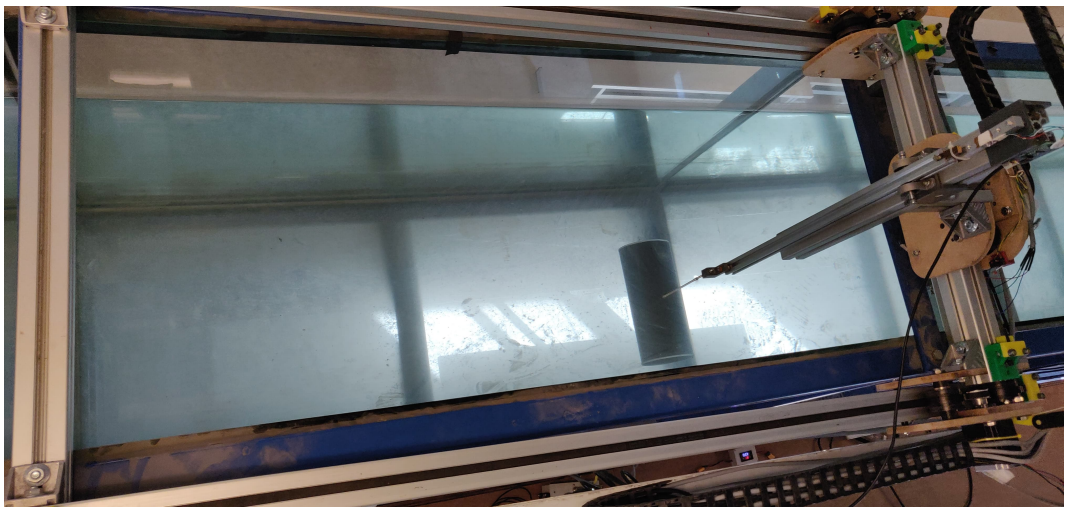

Figure 3.23: Automatic transverse system

However, the laboratory flume is reinforced with a transverse every 1.2 m. This distance and the automatic transverse system length limit us in the useful length for conducting the experiments (about 1 m).

This measuring system has been tested and the high variability of the obtained results lead to the conclusion that these results were not usable. These results and reasons of high variability are detailed in Appendix .5.

3.2 Towing tank

3.2.1 Experimental setup

Experiments at scale 1:1 were undertaken in the towing tank of the University of Liege. The towing tank is a basin with dimensions of 100x6x4 m³ and equipped with a towing carriage (Figure 3.24). The principle of operation is exactly the same as with the automatic transverse system in section 3.1.3.3. The differences are the scale and the fact that the available body model is not as articulated as the three smaller ones used for the experiments in the hydraulic flume.

These experiments allow obtaining results without any scale effects. The comparison between these results and the ones of the other experiments is not possible. Indeed, we attempt to work with the Reynolds similarity with small models at a scale of about 1/6. That means that to work at the same Re, velocities have to be about 6 times slower than the one of the flume which are already low.

$$\frac{U_{ch} * L_{mod}}{\nu} = Re = \frac{U_{real} * L_{real}}{\nu} \tag{3.10}$$

$$\frac{0.1 * 0.3}{10^{-6}} = Re = \frac{\frac{0.1}{6} * (0.3 * 6)}{10^{-6}} \tag{3.11}$$

The minimum velocity attainable was 0.1 m/s. For this difference of Re, the experiments are not comparable to the one made in the flume. Moreover, models, position and flow are also different from one scale to another which lead to different sources of error.

Figure 3.24: Towing tank

3.2.2 Models characteristics

This model is a modified clothing boutique display model of 1.8 m and 60 kg (Figure 3.25). Its legs are not movable and its arms have a weak resistance to motion. The studied position is the position showed in Figure 3.25, with the main direction of the body aligned with the main flow, legs and arms placed horizontally.

Figure 3.25: Model for the experiments at scale 1:1

As it is not possible to compare data from the towing tank with data from the flume due to the difference of Re_p, the influence of the clothing which was not studied in the flume are studied. It is decided to dress this model with a sweater and a pants. At real scale these clothes are easy to find because their composition is the true composition. However, at a smaller scale, clothes are made out of a different material and it should be investigated whether the interaction with the flow is scaled adequately (Figures 3.26 and 3.27).

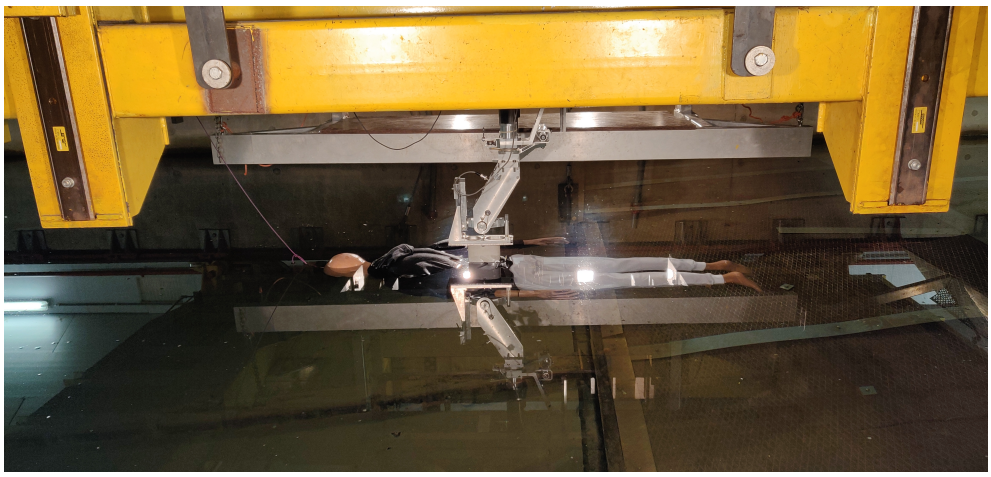

Figure 3.26: Body model dressed in the towing basin

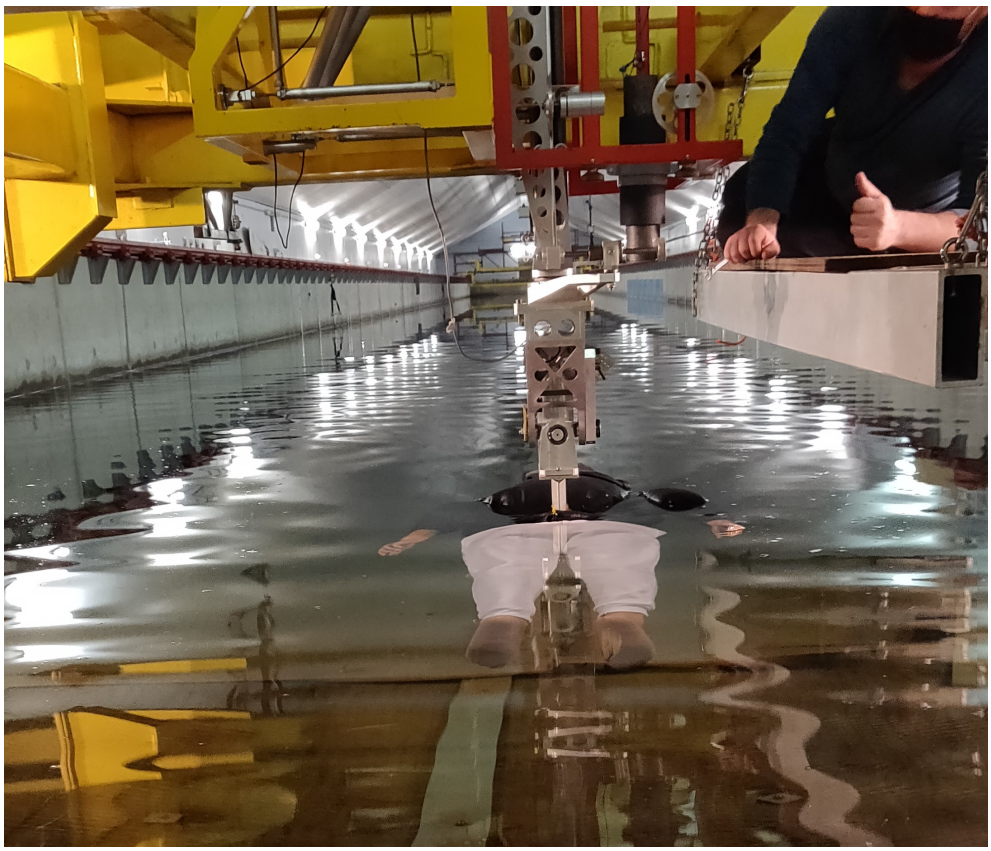

Figure 3.27: Body model dressed in the towing tank, seen from the back

3.2.3 Measurement devices

The towing tank measuring system consists in 6 strain gauges: one for the force in the streamwise direction, two for the force in the crosswise direction and 3 for the force in the vertical direction. This combinations of measurements allows to calculate the moment around each direction. The balance composed of the six strain gauges is presented in Figure 3.28.

Before realising a set of experiments, the balance is calibrated. This calibration is realised by putting four known weights alternately on each strain gauge and adjust the numerical result to the known force applied by each weight. This calibration method is indeed similar to the one used for the tests in flume.

Temperature in the towing tank is constant in time, $T = 15^oC$.

Figure 3.28: Balance used in the towing tank

Each test follows the same procedure of measurement, starting at $U = 0.10$ m/s:

1. dress or undress the body model;
2. start data registering;
3. wait for 20 s at least;
4. start the motion of the towing carriage at controlled velocity;
5. wait for 20 s at least;
6. stop data registering;
7. stop the motion;
8. repeat points 2 to 7 with controlled speed increased by 10 cm/s;
9. stop when $U > 50$ cm/s or $U = 0.44$ cm/s when going backward.

Data collected during step 3 are used for calibrating the zero of each measurement. Data collected during the last 20 s of step 5 are averaged and used as an estimation of the force during the process. The first ten seconds of this data set are not considered for the calculation of the force to avoid the acceleration phase.

Due to the range of measured forces in the crosswise directions (F < 1 N), only the one along the traction platform motion is analysed.

3.3 Results

3.3.1 Determination of the cross sectional velocity profile

3.3.1.1 Results

The first results were obtained with a discharge of 30 ± 0.3 l/s in the flume. Indeed, the only thing which can be controlled precisely is the head given by the pump to the water. In this experiment, the given pump head is 1.5 m/m.

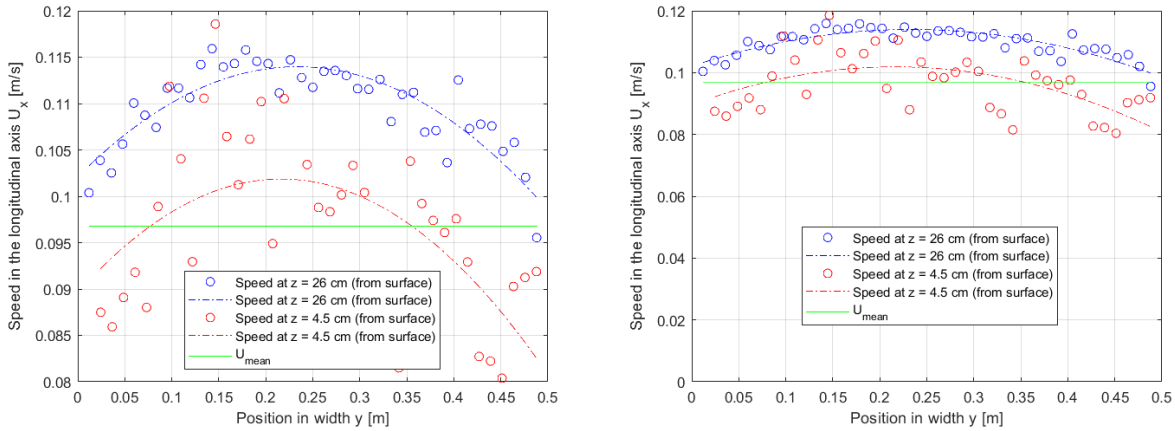

Figure 3.29: Crosswise profiles of the streamwise velocity component, measured with ADVP for a discharge of 55.7 l/s

Figure 3.29 shows that a linear regression is applied to these points using the least square method to get a second order polynomial. The equations got with these linear regressions write as follows:

$$U_{surface,30} = -0.2623y^2 + 0.1135y + 0.08958 \tag{3.12}$$

$$U_{mid\ height,30} = -0.2178y^2 + 0.1018y + 0.1021 \tag{3.13}$$

These equations are used to reproduce the flume in the numerical modelling to truly model the flume (section 4.3). Another utility of them is to confirm the accuracy of the measuring system comparing results to basic knowledge on drag coefficient.

Similarly, a vertical profile of the streamwise velocity components was measured along the centreline of the flume, for the same discharge as above (Figure 3.30).

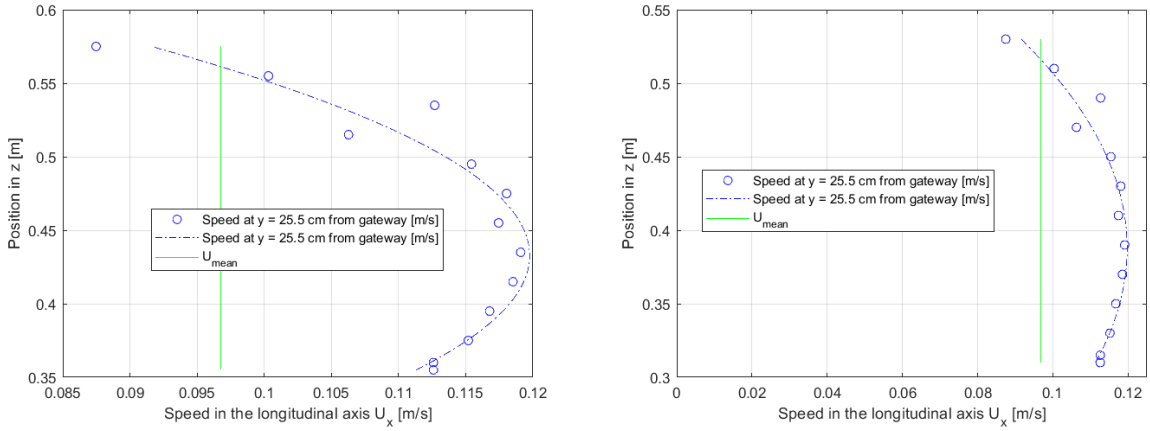

Figure 3.30: Vertical profile of the streamwise velocity component, measured with ADVP at the centreline of the canal, for a discharge of 30 l/s

In the same way as for the horizontal equations, equation 3.14 is written:

$$U_{height,30} = -1.394z^2 + 1.207z - 0.1414 \tag{3.14}$$

A similar procedure is followed for the seconds results with a discharge of 55.7 ± 0.6 l/s in the flume (Figures 3.31 and 3.32). In this experiment, the given pump head is 5 m/m. The obtained equations are:

$$U_{surface,55.7} = -0.6259y^2 + 0.3536y + 0.1549 \tag{3.15}$$

$$U_{mid\ height,55.7} = -0.5773y^2 + 0.2889y + 0.1673 \tag{3.16}$$

$$U_{height,55.7} = -1.128z^2 + 1.106z - 0.05556 \tag{3.17}$$

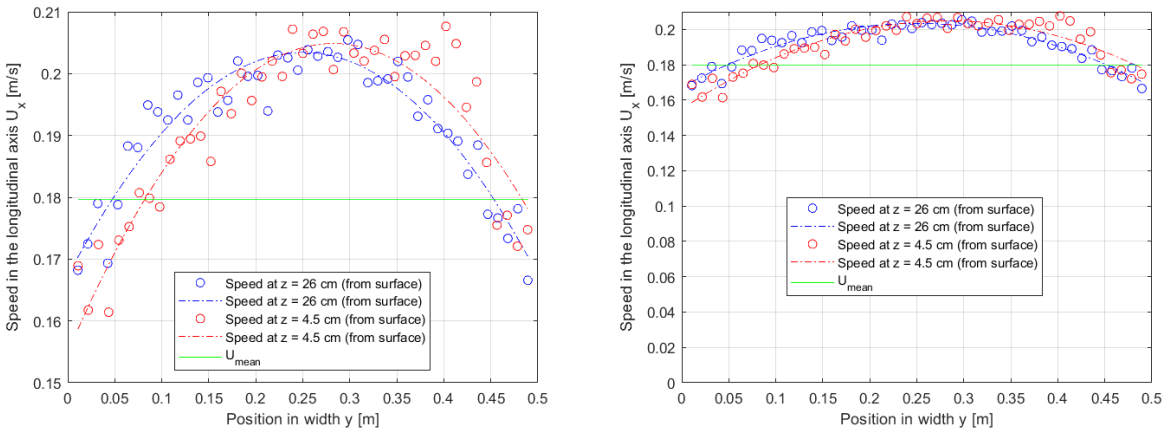

Figure 3.31: Crosswise profiles of the streamwise velocity component, measured with ADVP for a discharge of 55.7 l/s

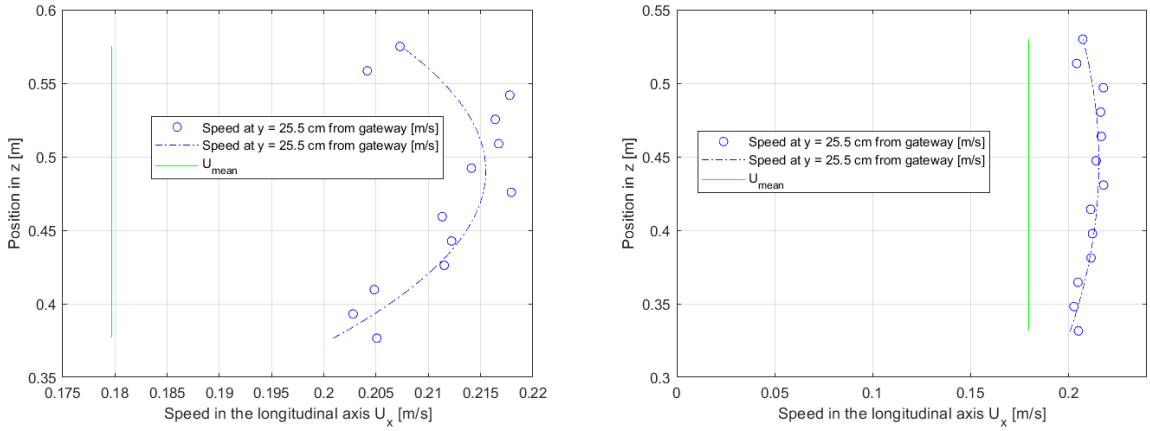

Figure 3.32: Vertical profile of the streamwise velocity component, measured with ADVP at the centreline of the canal, for a discharge of 55.7 l/s

3.3.1.2 Discussion

First, the velocity profile in width, U(y), is relatively uniform even if it is seen that water velocity increases while getting away from the walls. The water velocity measured at the closest points to the walls is about 80% of the maximum velocity in the flume for each discharge. This velocity is expected to decrease to 0 at the walls but it is not possible to measure it with the vectrino profiler.

First expectations were that the maximum velocity was at the surface of the flow because the velocity profile would have been a log-profile. In fact, that is not the case as the maximum velocity is at about 3/4 of the water depth. This phenomenon is called the dip phenomenon (Figure 3.33 and Equation 4.28 detailed in section 4.3.2.2). This dip phenomenon is due to secondary currents and is visible in narrow flumes. Research has already been made to take into account the dip effect in the logarithmic law (Dey, 2014; Yang et al., 2004).

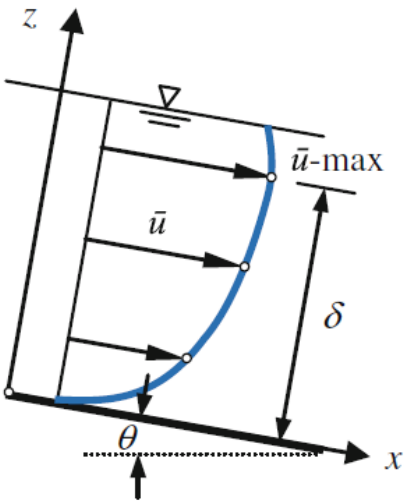

Figure 3.33: Velocity profile in the xz plane, showing the dip phenomenon (Dey, 2014)

$$\bar{u}^{+} = \frac{1}{\kappa}\left[\ln\frac{\tilde{z}}{\tilde{z}_0} + \alpha\ln(1-\tilde{z})\right] \tag{3.18}$$

3.3.2 Measurement of drag with a Re_p between 10^4 and 10^5

In section 3.1.3.2, it is shown that the measuring system is stable enough to measure an accurate force. Duration and sampling frequency can now be analysed, as well as their accuracy and finally the drag coefficient of a body could be deduced in the attainable range of Re_p. Furthermore, accurate tests are not realised with discharge $Q > 55.7$ l/s because these conditions are not adapted to our measurements (stability, sampling time, water velocity, etc.).

3.3.2.1 Convergence analysis

In order to be concise, only two representative tests will be analysed. These two are the two extremes (Table 3.6):

Test	h [m]	Q [l/s]	U_{mean} [m/s]	θ [^{o}]	z [m]	Amplification by the lever arm
Test 1	0.62	30	0.097	90	0.58	6.04
Test 2	0.62	55.7	0.18	0	0.3	9.1

Table 3.6: Tests for the convergence analysis

The convergence analysis of the sets is realised analysing first statistic moment, the average, and the square root of the second one, the standard deviation. Each one is studied with and without the amplification by the lever arm.

The goal is to determine if the data set allows to be stable. Moreover, inaccuracies of the first values have to be avoided. Indeed to start the measurements an operator has to come close to the system and generate a variation of the electrical field which could influence the results. As this interaction has to be realised, it has been decided to neglect first values to make sure that there is no effect of this interaction. Furthermore, problem of vortex detachment occurs and may influence the measurement. A quick calculation of the frequency of these oscillations due to our screw is the following (Katopodes, 2019):

$$\begin{aligned} f &= \frac{St * U_{w,min}}{D} = \frac{0.2 * 0.1}{0.003} = 6.67\ Hz \\ f &= \frac{St * U_{w,max}}{D} = \frac{0.2 * 0.2}{0.003} = 13.33\ Hz \end{aligned} \tag{3.19}$$

And the frequency of detachment is from 6.67 Hz to 13.33 Hz with our Re (influence the Strouhal number), velocity and screw diameter. If the amplitude of these oscillations are small compared to the one of the measured forces, they can be neglected.

The explanation of the following Figures is this one: they represent the statistic moments of the data set starting at the value in X to the end (Figures 3.34 and 3.35). Ex: the 100th element of Figure 3.34 represents the average value of the data set if we consider a data set going from the 100th measurement to the last one. Statistic moments can be analysed without considering the effect of the length of the lever arm on all the figures on the right.

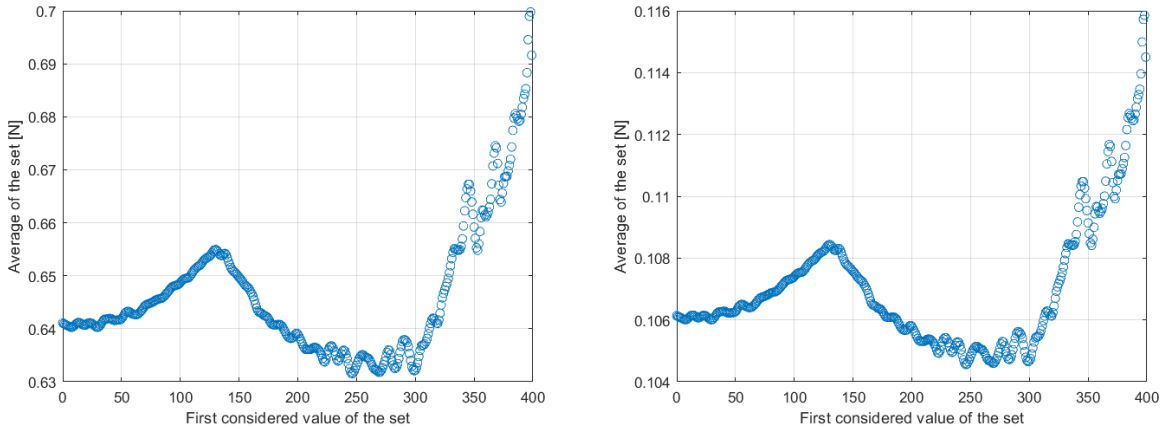

Figure 3.34: Average of Test 1 with and without the lever arm

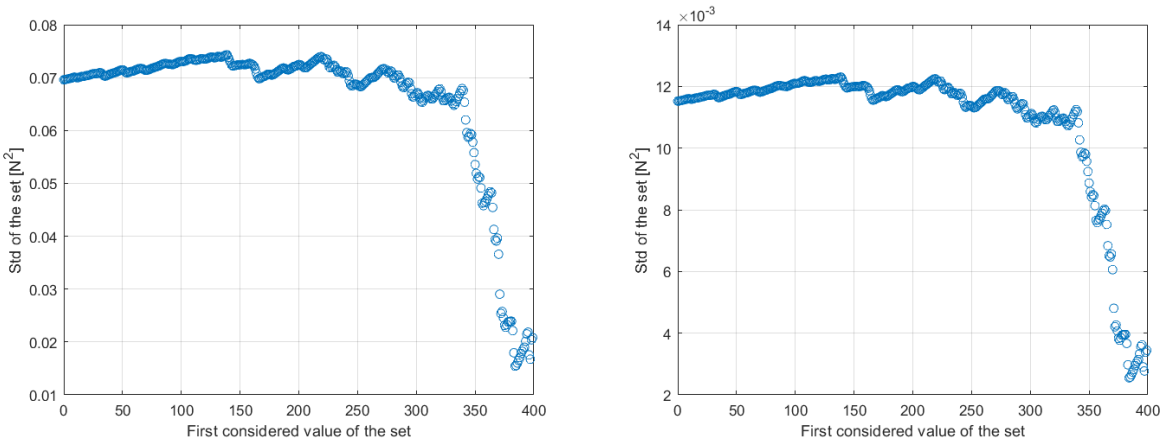

Figure 3.35: Standard deviation of Test 1 with and without the lever arm

At first, the average values of Test 1 vary of about 2% for the most data set. However, measured values are very small and the order of the instability is difficult to evaluate. Then, the standard deviation is very stable for a data set bigger than 200 elements. The interaction with the system seems to have no effect on the data set and the set may be considered from the start.

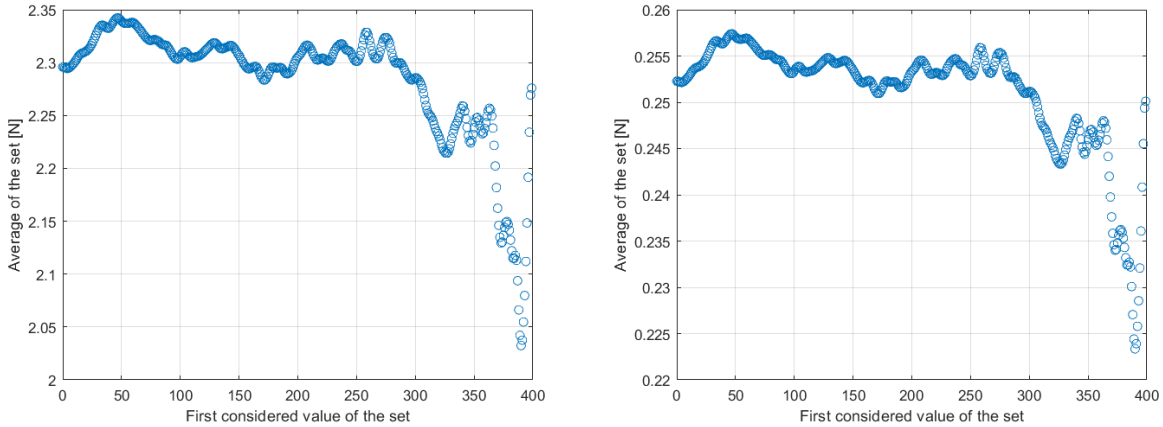

Figure 3.36: Average of Test 2 with and without the lever arm

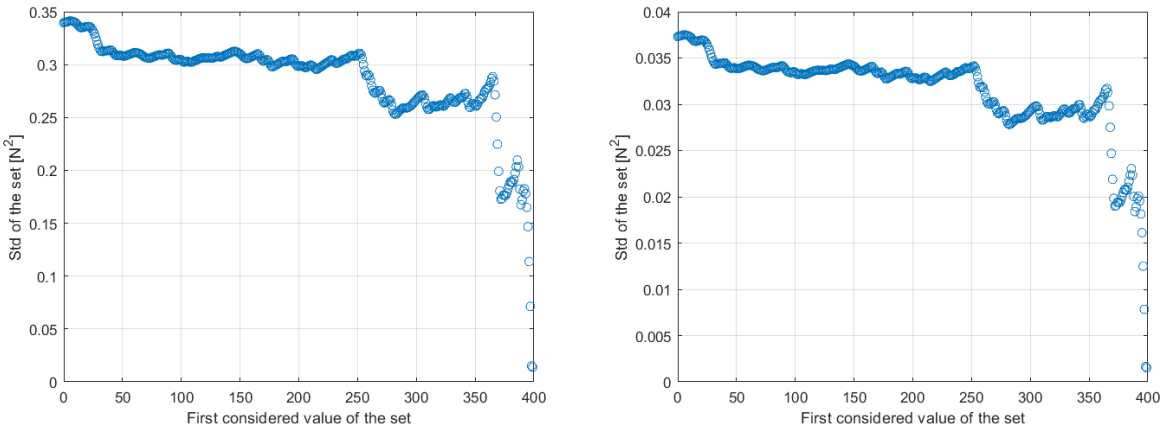

Figure 3.37: Standard deviation of Test 2 with and without the lever arm

In Figures 3.36 and 3.37, values seem to be abnormally higher than the ones of Test 1. Figures on the right show that this is not the case. Indeed, with this data set, water velocity is twice as high as the previous one, the position is different and the lever arm amplifies the force by 9.1 instead of 6.04. The standard deviation is very stable for a data set bigger than 150 elements. However the interaction with the system clearly has an effect on the statistic moments and it has to be taken into account.

It has been decided to take the 50th value of each experiment as the first value of each data set. This means that each experiment will be represented as the average of its values from the 50th to the 401th.

A way to convince oneself that this choice is robust is to compare each statistic moment with the one picked and to analyse the difference. Figures 3.38 and 3.39 are the same as the previous ones but divided by the 50th value of each. This allows to see the robustness of our choice. The average shows that the variability is of a very low order. The difference is only of 2% for a huge range of value (1st to $300^{t}h$ element). The standard deviation is once again very constant for each case and confirms our choice.

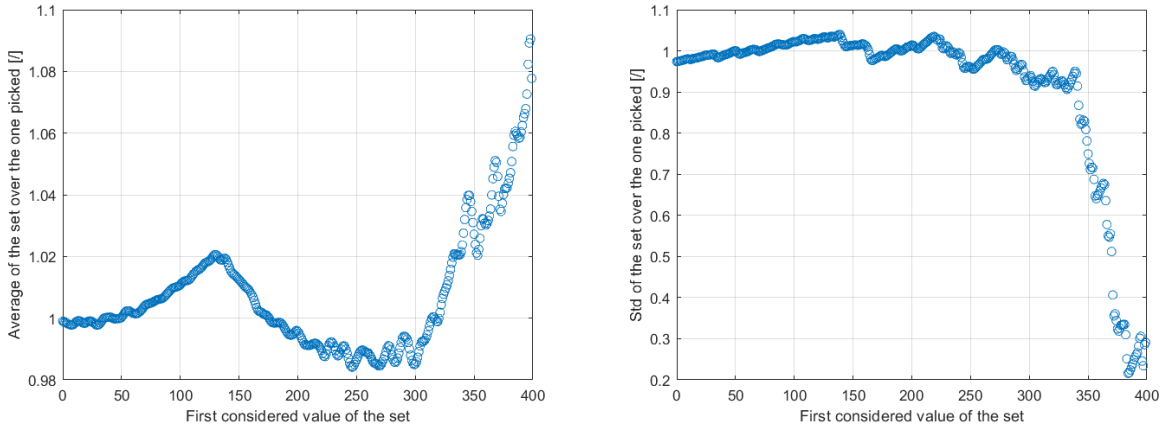

Figure 3.38: Average and standard deviation of test 1 normalised

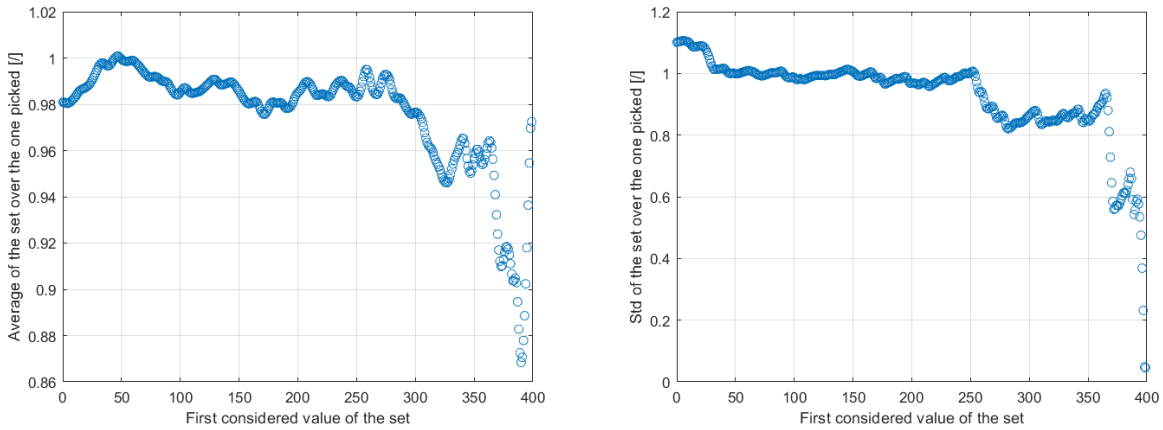

Figure 3.39: Average and standard deviation of test 2 normalised

3.3.2.2 Tests on a cylinder

The goal of these tests is to confirm that the measured force is the drag and that drag coefficient can be deduced. Given that the drag coefficient is very well known for a wide range of Re_p for simple shapes, the same procedure as for the models is followed but this time with a cylinder and the results will be compared to the references (Chu et al., 2018; Hölzer and Sommerfeld, 2008; Yang et al., 2015).

The cylinder used in the experiments is 24 cm long and has a diameter of 11 cm. Measurements are done with the cylinder oriented with his length perpendicular to the main flow direction, as shown in Figure 3.40.

First, the basic knowledge on drag coefficient of a cylinder does not say the depth of the cylinder in the flow. Some studies are made by Chu et al. (2018) to determine the impact of depth on the drag coefficient of a cylinder. Thanks to their observations, it is considered that for our range of Re_p, the classical drag coefficient is the one at $h/D \geq 2$ and the level is $C_D \approx 1.05$. We will also assume that the level is $C_D \approx 1.4$ (Figures 3.40 and 3.41) at $h/D = 0.2$. In this range of Re_p, drag coefficient C_D is constant and a C_D level is considered to express the drag coefficient independently from the Re_p. In our case, $h/D = 2$ corresponds to a cylinder placed at mid height of the water column Chu et al. (2018).

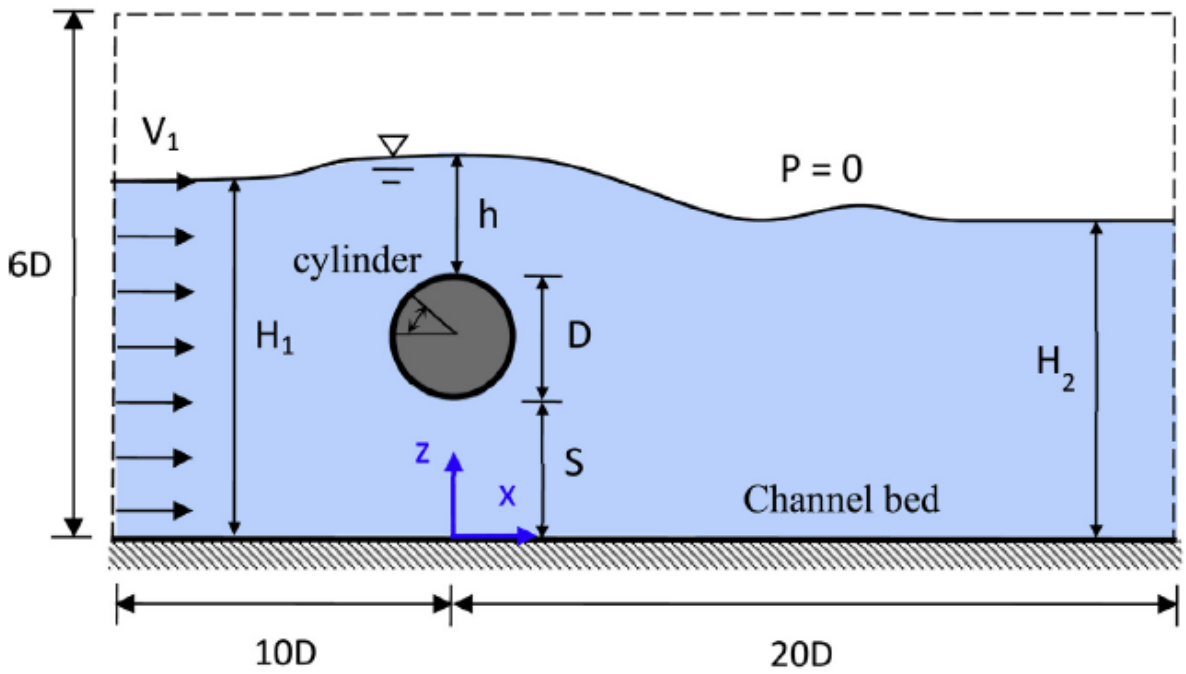

Figure 3.40: Scheme of the influence of depth (Chu et al., 2018)

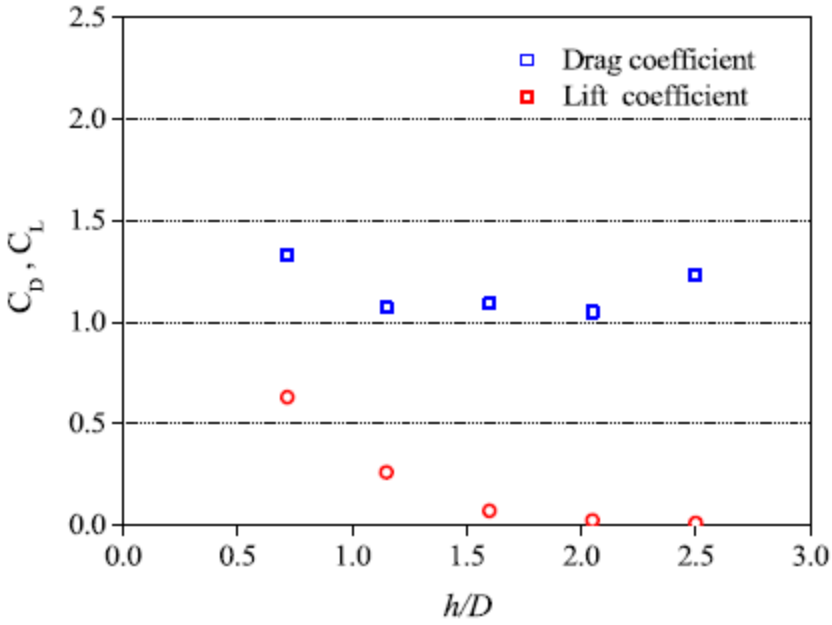

Figure 3.41: Results of the influence of depth on C_D (Chu et al., 2018)

The force measured at rest is the buoyancy on the cylinder. Our measurements are taken at a known velocity and the force at rest is subtracted from the other measurements. A drag coefficient is finally calculated with Eq. 3.20. The comparison between results and the ones from the literature is plotted with the equation found in Chu et al. (2018); Hölzer and Sommerfeld (2008). Nevertheless, there is a certain imprecision on the frontal areas A_p of our models. This is the reason why the coefficient $C_D A$ (Eq. 3.21) is used for the cylinder.

$$C_D = \frac{2F}{\rho_w A_p U_w^2} \tag{3.20}$$

$$C_D A = \frac{2F}{\rho_w U_w^2} \tag{3.21}$$

The last modification which has to be done to our data is removing the influence of the screw for the tests made at mid height of the water column. For that purpose, measurements of the lonely screw of 24 cm in water are taken at each velocity and then the measured force is removed from the others tests. The used screw has a diameter 3 mm and its influence is not negligible. At the surface, it is considered that the screw has no influence on the results because it is only 1 cm underwater.

The two following graphs show that our results are very close to the literature even if our measurement procedure and equipment are quite rudimentary (Figure 3.42). This confirms that the setup gives accurate results and that this procedure is efficient.

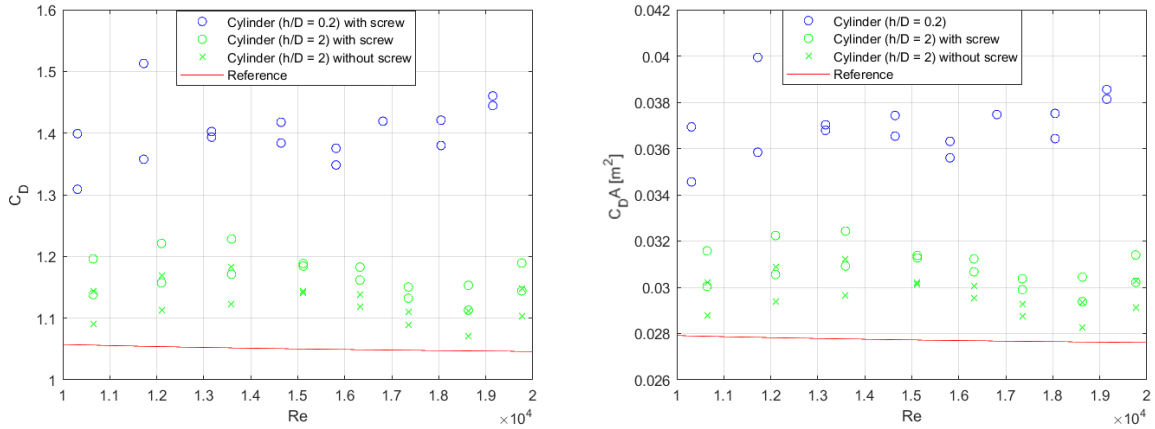

Figure 3.42: C_D and C_DA measured in our lab

Another way to confirm that our results are correct is to fit our data to a known shape. Indeed, equation 3.20 could be adapted to classical functions and see the proximity to $F = aU^2$ with $a = 1/2\rho_w A_p$ and in this case, $U = U_w$. It is even possible to go further while comparing results obtained with U_w taken as the average velocity on the cross section of the flume or the velocity measured with the ADVP (Figure 3.43).

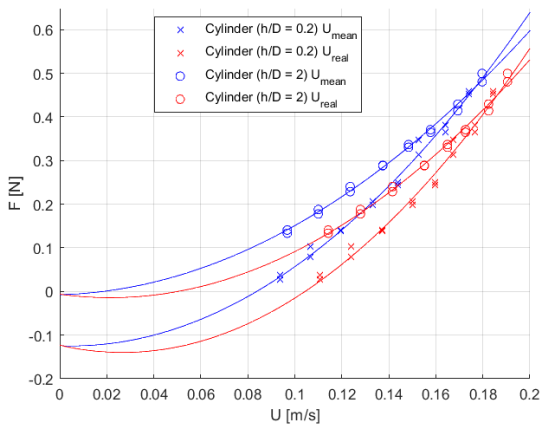

(a) $F = aU^2 + bU + c$

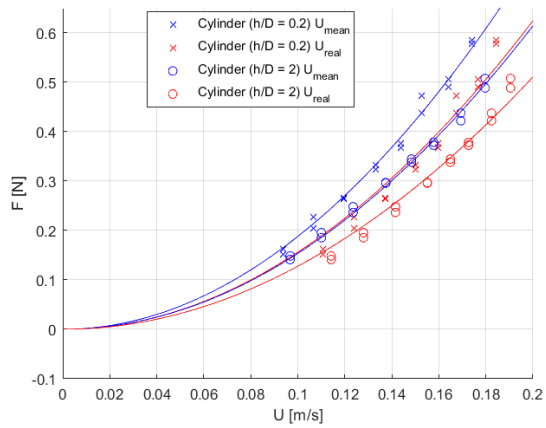

(b) $F = aU^2$

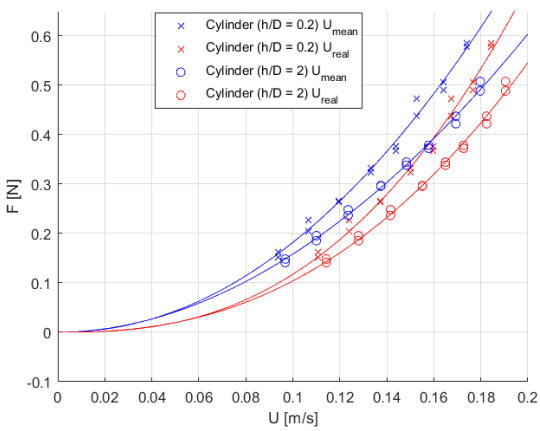

(c) $F = aU^b$

Figure 3.43: Equations fitted

As it can be seen on the graphs, data set had to be modified to fit equations of types (b) and (c). Indeed, the buoyancy is added to all the collected data in order to avoid the ordinate at the origin which is zero with these two kinds of equations.

Equations and correlation R^2 is computed and is shown in the following Tables 3.7, 3.8, 3.9 and 3.10:

Equation type	Equation	R^2
$F = aU^2 + bU + c$	$F = 20.07U^2 - 0.1969U - 0.1243$	0.9951
$F = aU^2$	$F = 18.77U^2$	0.9945
$F = aU^b$	$F = 21.8U^{2.079}$	0.9952

Table 3.7: Equations with average velocity on the flume at the surface

Equation type	Equation	R^2
$F = aU^2 + bU + c$	$F = 23.21U^2 - 1.242U - 0.1232$	0.9922
$F = aU^2$	$F = 15.59U^2$	0.9719
$F = aU^b$	$F = 44.39U^{2.578}$	0.9937

Table 3.8: Equations with velocity determined with the ADVP on the flume at the surface

Equation type	Equation	R^2
$F = aU^2 + bU + c$	$F = 14.41U^2 + 0.1423U - 0.007475$	0.9976
$F = aU^2$	$F = 15.34U^2$	0.9972
$F = aU^b$	$F = 13.54U^{1.933}$	0.9976

Table 3.9: Equations with average velocity on the flume at mid height

Equation type	Equation	R^2
$F = aU^2 + bU + c$	$F = 17.11U^2 - 0.7332U - 0.006394$	0.9949
$F = aU^2$	$F = 12.76U^2$	0.986
$F = aU^b$	$F = 25.65U^{2.393}$	0.997

Table 3.10: Equations with velocity determined with the ADVP on the flume at mid height

Even if the shape which interests us the most, $F = aU^2$, is the worst, the correlation is of very good quality ($R^2 > 0.9$). Furthermore, the use of the precise velocity in the flume decreases the quality of the correlation. This point, added to the fact that this velocity is though to use, led us to the decision that the average velocity on the cross section should be used in the determination of the drag coefficients C_D and $C_D A$.

The conclusion based on the two manipulations of our data is that the measured force is actually drag with a very low impact of other forces.

3.3.2.3 Drag coefficients on human shape

In this section, the influence of various factors on the drag coefficients, C_D and C_DA, of a human body shape are studied. Re_p, the orientation, the depth and the body shape are the studied factors.

First of all, the comparison is done with the drag of a cylinder found in the literature. The work is realised with an average water velocity between 0.09 m/s and 0.18 m/s which gives Re_p between $2.8 * 10^4$ and $5.2 * 10^4$ with a static model. It is already known from the previous section that the drag coefficient of a cylinder in this range of Re_p is at a level of $C_D \approx 1.4$ at the surface and $C_D \approx 1.05$ at 25 cm of the surface for our flow conditions.

A thousand samples have been taken. The only ones shown in this chapter are some representative tests but you can find all the results in appendix.

Four coefficients/forces to analyse our results are shown. First one is the drag coefficient C_D which is the final wanted result. However it is shown that there are some uncertainties on the determination of the frontal areas. On account of that, drag coefficient C_DA of the models is studied but it must be kept in mind that multiplying the drag by the frontal area involves an impossibility to study the influence of the body shape. Secondly, measured force are analysed. The problem with this measurement is that Archimedean's thrust might be positive or negative and the analysis between each data set is complicated because each measurement depends on the measured force at $U = 0\ m/s$. To avoid this complication, each data set is corrected by removing the Archimedean's thrust from the measurement. This allows to analyse each data set starting from $F = 0\ N$ when $U = 0\ m/s$. However this manipulation involves that it is not possible to see the measured force at rest and compare it to the other forces.

The conclusion can finally be drown assuming that it is wanted to analyse one coefficient and one force which are C_D and the true force. But as they have some flaws, two more coefficient and force are analysed to overcome these specific flaws.

All of the following analysis is summed up in Table 3.11.

The analysis focuses on the influence of depth as previously done with the cylinder in section 3.3.2.2. The four coefficients and forces are studied for the case of a model placed at 90° in the flume. As a reminder, the orientation 90° means that the model is oriented perpendicularly to the main flow direction. It is expected to have a higher drag coefficient for a human body shape than for the cylinders because of limbs hanging vertically.

On the following graphs, set 1 is for measurements taken at the surface while set 2 is for measurements taken 25 cm bellow the surface and so, at mid height of the water column (Figures 3.44 and 3.45)[1].

[1]We invite you to return to Figure 3.5 if you want to identify clearly each model.

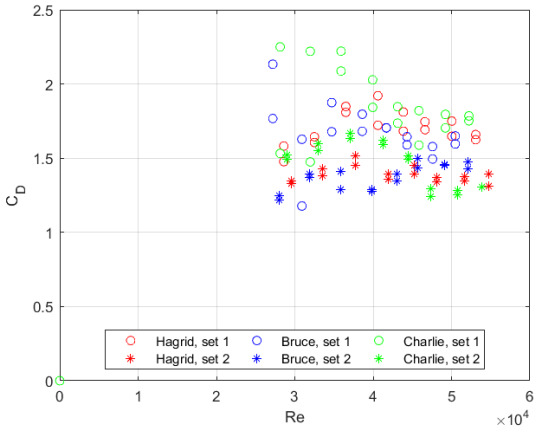

(a) C_D

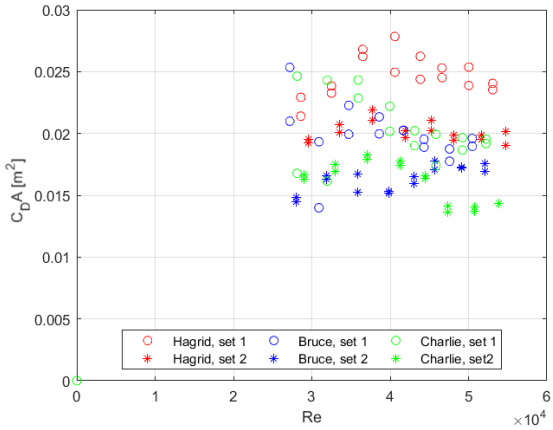

(b) C_DA

Figure 3.44: Drag coefficients of each body at an orientation of 90°, set 1 = measurements taken at the surface, set 2 = measurements taken 25 cm bellow the surface

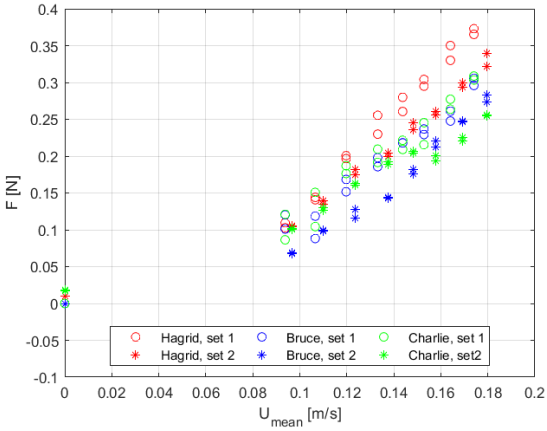

(a) F measured

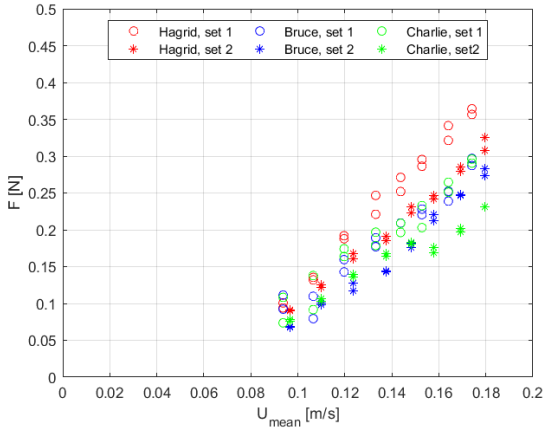

(b) F corrected

Figure 3.45: Force on each body at an orientation of 90°, set 1 = measurements taken at the surface, set 2 = measurements taken 25 cm bellow the surface

What stands out first is that a level is present for each model and depth except for a few inaccuracies. Another obvious point is that measured forces are higher near the surface than in the middle of the water column. That leads to higher drag coefficients near the surface. Then, the deeper you are, the more stable the measurements. Concerning the body shape, Hagrid's data are useful to explain what is said with the two drag coefficients because he is the most corpulent. Indeed, his C_DA is higher than the ones of the two other models. However, when taking a look at his C_D, it is not the case and Hagrid's drag coefficient C_D is in the same range as the two others. These graphs perfectly show one of the utility of a two drag coefficients analysis instead of one. C_DA proves that the measured force is higher for Hagrid than for the two others but his frontal area is higher too and so the same observation can not be made with the C_D.

Taking a look at forces, it is seen that the measured forces at a low velocity are very small, of the order of the tenth of a Newton. Because of that, data collected at low velocity are more subjected to noise. It is a point which has to be considered when taking conclusions. This is the reason why first points of C_D of Bruce and Charlie are not considered for the level in the first graphs.

Knowing that there is a level for each drag coefficient in the range of Re, the influence of the orientation of the body at different submersion depths and velocities was analysed. The results are plotted as a function of the orientation of the body at the minimum and maximum water velocity (Figures 3.46 and 3.47).

In Figures 3.46, 3.47, 3.48 and 3.49, set 1 is for measurements taken at $U = 0.94\ m/s$, the minimum velocity, and $Re_p = 2.8 * 10^4$ while set 2 is for measurements taken at $U = 0.175\ m/s$, the maximum velocity, and $Re_p = 5.2 * 10^4$.

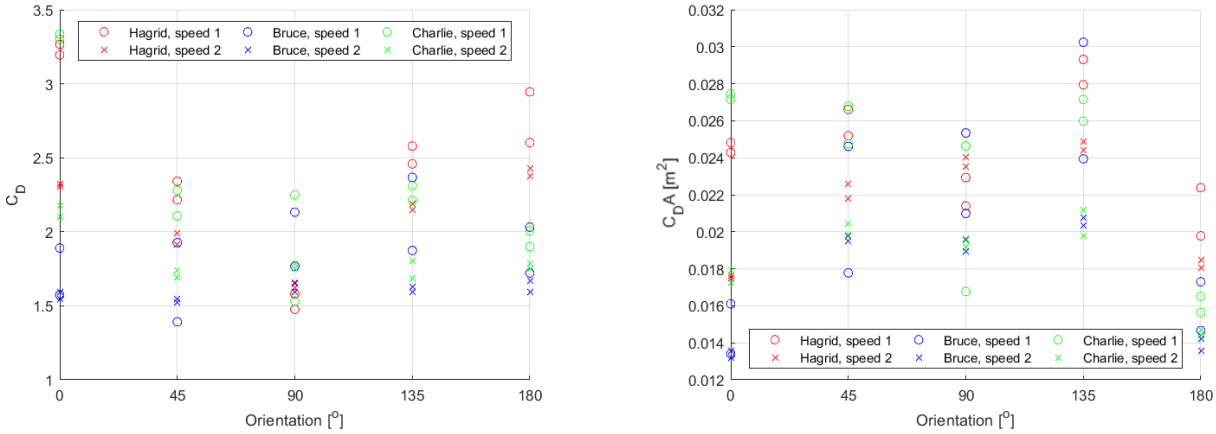

(a) C_D (b) $C_D A$

Figure 3.46: Drag coefficients at the surface, speed 1 = measurements taken at $U = 0.94\ m/s$, speed 2 = measurements taken at $U = 0.175\ m/s$

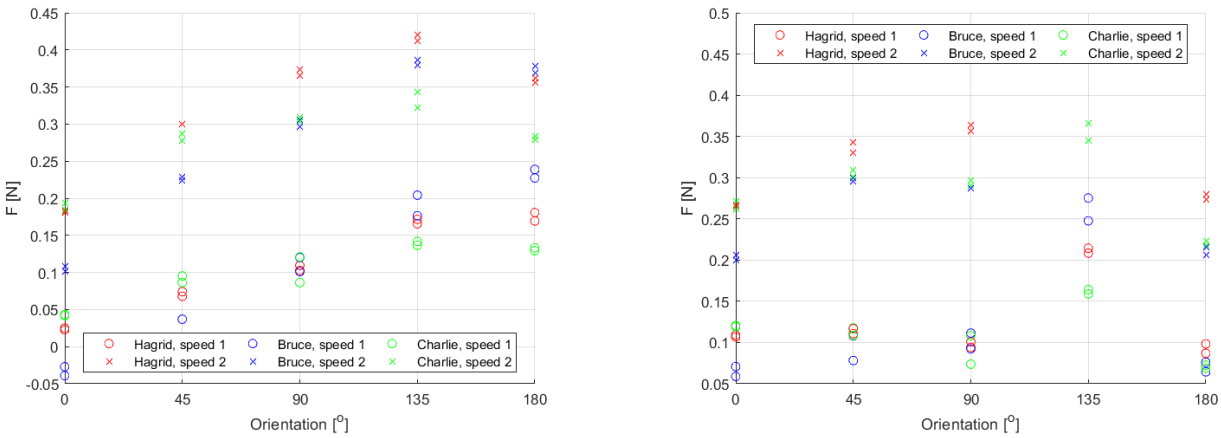

(a) F measured (b) F corrected

Figure 3.47: Force on the body at the surface, speed 1 = measurements taken at $U = 0.94\ m/s$, speed 2 = measurements taken at $U = 0.175\ m/s$

The collected data show that there is a minimum of drag coefficient C_D for Hagrid when $\theta = 90^o$. This is not the case for the C_DA. On the contrary, the drag coefficients are very close, if not the same, for each orientation of Bruce and Charlie. That suggests that the orientation seems important when the body is corpulent like Hagrid but the orientation might have less effect when the body is thin. Indeed, C_DA is higher when the body perpendicular to the main flow direction but the frontal area compensates this raise of force when evaluating the drag coefficient.

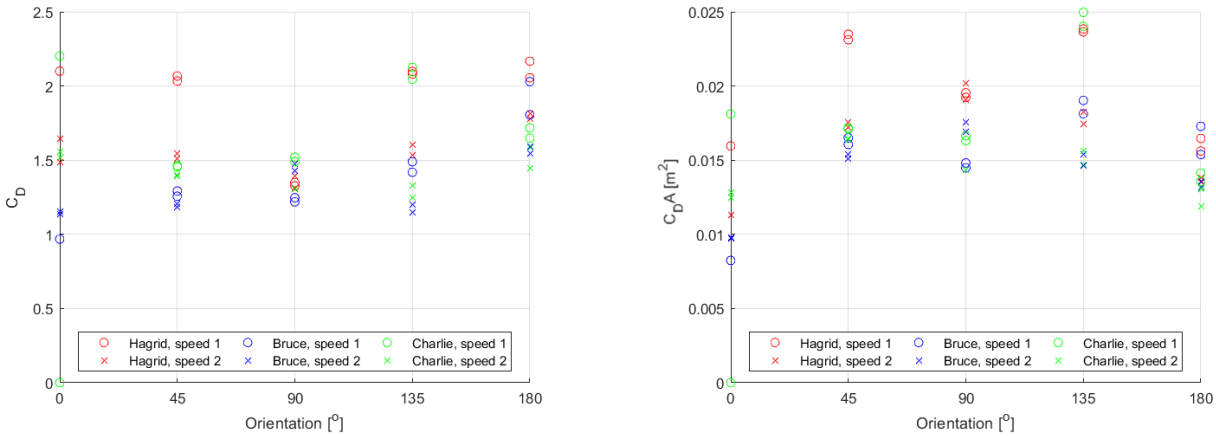

(a) C_D (b) C_DA

Figure 3.48: Drag coefficients at the mid depth, speed 1 = measurements taken at $U = 0.94\ m/s$, speed 2 = measurements taken at $U = 0.175\ m/s$

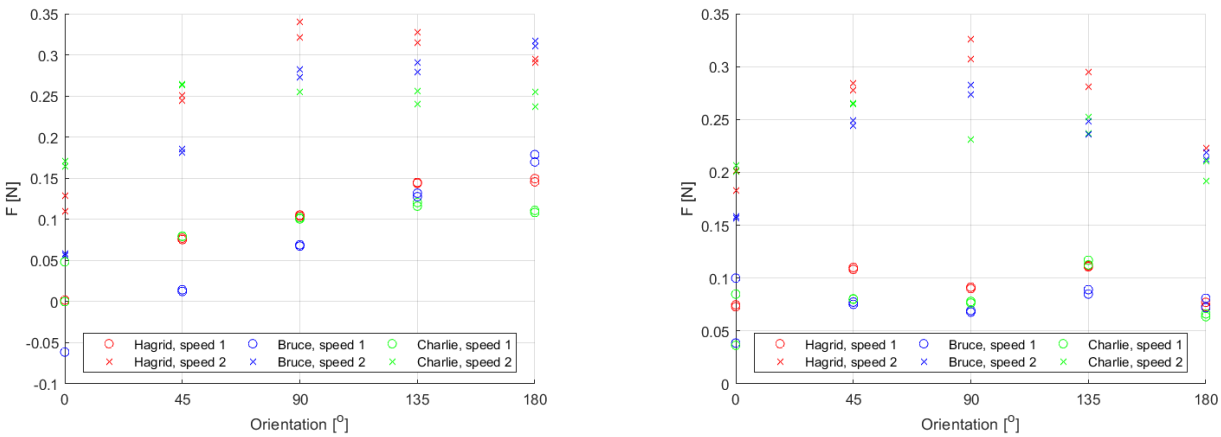

(a) F measured (b) F corrected

Figure 3.49: Force on the body at the mid depth, speed 1 = measurements taken at $U = 0.94\ m/s$, speed 2 = measurements taken at $U = 0.175\ m/s$

First, drag coefficients are as expected lower than the one measured at the surface and are both more stable even if low velocity measurements are less reliable. Then, once again, a level is observed for all orientations for Bruce and Charlie while Hagrid's orientation has still influence on both coefficients but of less pronounced than at the surface.

These results are summarised in the two Tables 3.11.

(a) Surface, $\frac{h}{D} = 0.2$

Model	θ [^{o}]	C_D	$C_D A$ [m^2]
Cylinder	90	1.4	0.037
Hagrid	0	2.25	0.0165
	45	2.25	0.025
	90	1.7	0.025
	135	2.25	0.027
	180	2	0.015
Bruce	0	1.7	0.015
	45	1.9	0.023
	90	1.65	0.0205
	135	1.65	0.0235
	180	1.7	0.015
Charlie	0	2.25	0.019
	45	2	0.019
	90	1.75	0.021
	135	1.65	0.023
	180	1.8	0.015

(b) Mid height of the water column, $\frac{h}{D} = 2$

Model	θ [^{o}]	C_D	$C_D A$ [m^2]
Cylinder	90	1.1	0.03
Hagrid	0	1.65	0.013
	45	1.6	0.02
	90	1.45	0.02
	135	1.75	0.02
	180	1.9	0.015
Bruce	0	1.15	0.095
	45	1.25	0.0155
	90	1.4	0.0165
	135	1.25	0.0155
	180	1.5	0.013
Charlie	0	1.65	0.014
	45	1.4	0.0165
	90	1.5	0.016
	135	1.4	0.0165
	180	1.5	0.013

Table 3.11: Summary of the measured drag coefficients level

These two tables summarize around one thousand experiments and allow comparing each orientation and models with themselves and with a cylinder when $Re_p \approx 10^4$. They highlight the fact that both drag coefficients are needed to understand the force on the body and to be aware that the final C_D strongly depends on the estimation of the frontal area. As an example, Hagrid's results on the first table are analysed. As a result, $C_D = 2.25$ for three orientations but their $C_D A$ differ greatly[2]. They highlight the fact that drag is higher when the body is not aligned with the stream.

[2]Values in the two tables resume previous graphs and the ones in appendix. This is the reason why $C_D = 2.25$ for Hagrid at $\theta = 0^o$ while this not the case looking only at graphs in the body of this work. The same observation can be generalised with all data from Tables 3.11

We will now explain the $C_D A$ maxima at $\theta = 45^o$ and $\theta = 135^o$. The only data set which is kept is the one at the maximum velocity and mid height of the water column. This choice of keeping only one data set is make for the sake of clarity. The evaluation of $C_D A$ with the body orientation is examined and compared to the measured frontal areas A_p (Figure 3.50).

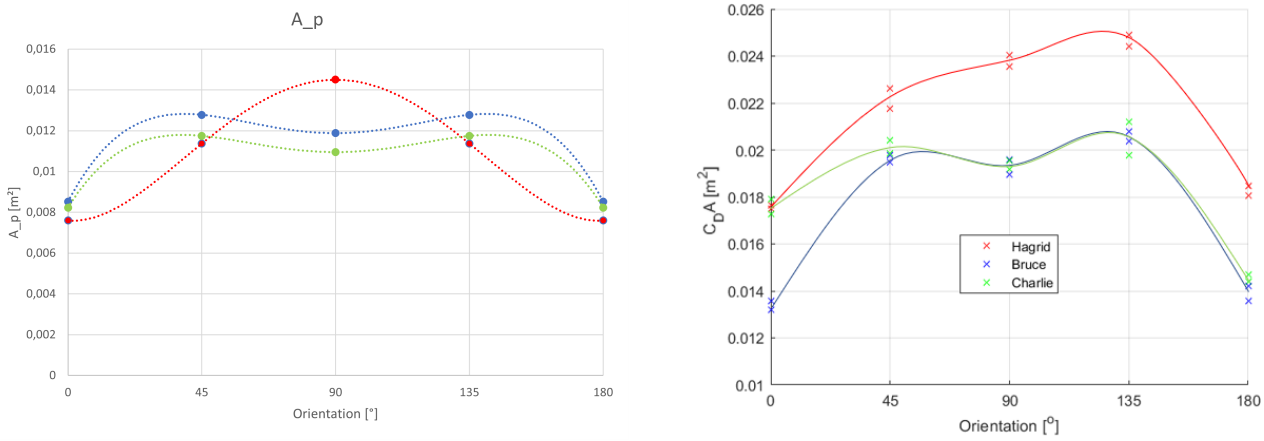

(a) A_p

(b) $C_D A$

Figure 3.50: Analysis of A_p and $C_D A$

$$C_D A = \frac{2F}{\rho_w U^2} \tag{3.22}$$

Even if this drag coefficient is not dependent on the frontal area, its evolution is similar to that of A_p for Bruce and Charlie. That means that drag is influenced by the real frontal area. Indeed, the accurate frontal areas are not known but their range are. This kind of representation clearly shows that drag varies similarly to A_p for Bruce and Charlie. Concerning Hagrid's case, the link between $C_D A$ and A_p is less obvious. It is needed to go back to section 3.1.2.4 to understand their link. It has been observed that at 45° and 135°, one of his legs is aligned with one of his arms. This alignment, considerably reduces the frontal area of the model. However, at 47° or 133° for example, arms and legs are not aligned and the frontal area increases. That means that results obtained for Hagrid have the same shape as Bruce's frontal area if the orientation is not perfectly the one mentioned. While it has the same shape as his frontal area if his orientation is exactly the one mentioned, $\theta = 45^o$. This precision depends on the water velocity and the initial orientation of the body as it is not a perfectly rigid assembly between the model and the measuring system. Two examples showing what is said with the perfect alignment and the one a little bit shifted are highlighted in Figures 3.48 and 3.51.

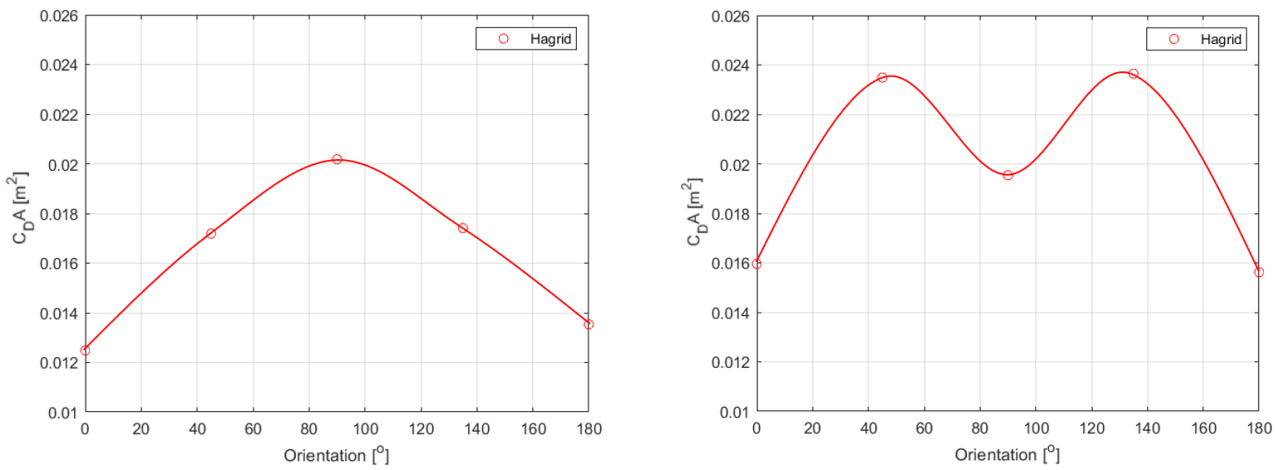

(a) Perfectly oriented

(b) Small shift

Figure 3.51: Shape of the C_DA depending on the precision of the orientation

They clearly show that not only the drag coefficient C_DA depends on the frontal area but the measured force too. Indeed, a study of the area independent coefficient C_DA showed that drag itself depends on the perfect alignment between legs and arms and so data collected near this point of alignment are very though and have to be considered as an average between a perfect alignment and a little shift. Furthermore it shows that drag strongly depends on the body shape as this phenomenon does not apply with Bruce and Charlie for the tested orientations. However, the same phenomenon is expected with these two other models but at different orientations.

Considering this analysis, a final level of drag coefficient C_D can then be found for each model as an average of all levels (Table 3.12). This final level allows an analogy with simple shapes. Indeed drag coefficient C_D of a cylinder is constant for all orientation θ but the cylinder area changes and is easily calculated knowing θ. In this case, the C_D level is determined independently from θ too but it depends on some parameters like the body shape, hair, etc. However, the determination of the frontal area is less straightforward than for a cylinder and its variation influences a lot the drag.

(a) Surface, $\frac{h}{D} = 0.2$

Models	CD level
Cylinder	1.4
Hagrid	2
Bruce	1.7
Charlie	1.75

(b) Mid height of the water column, $\frac{h}{D} = 2$

Models	CD level
Cylinder	1.1
Hagrid	1.65
Bruce	1.45
Charlie	1.45

Table 3.12: Drag coefficients level

3.3.3 Towing tank

In the towing tank, tests were conducted at velocities from 0.1 m/s to 0.5 m/s which gives Re_p between 10^5 and $8 * 10^5$. The data sets are treated exactly as with the other measuring system. A force is measured and then two drag coefficients $C_D A$ and C_D are deduced from this force. The area of the model is estimated following the same procedure as for the three scale models and $A_p = 0.059\ m^2$.

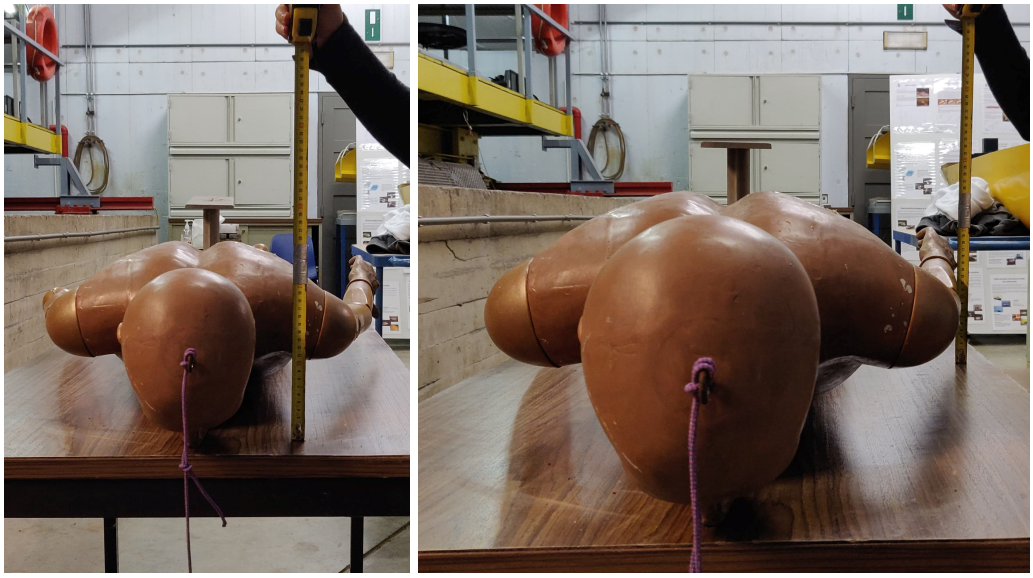

Figure 3.52: Pictures used for the estimation of the frontal area

The issue with this model and orientation is that it is longer than the previous ones and the image distortion is more important. Indeed, if the meter is placed at the shoulders of the model, the estimated area is $A_p = 0.059\ m^2$. But if it is placed at the pelvis, the frontal area is $A_p = 0.196\ m^2$ (Figure 3.52). The estimated area can change by a factor of 3. For this reason, the estimated area with the meter at the shoulders is kept as a reference area instead of averaging all the measurements. However, this makes the analysis of drag coefficient C_D is almost impossible and the analysis is realised on the comportment of coefficients instead of on their value (Figure 3.54).

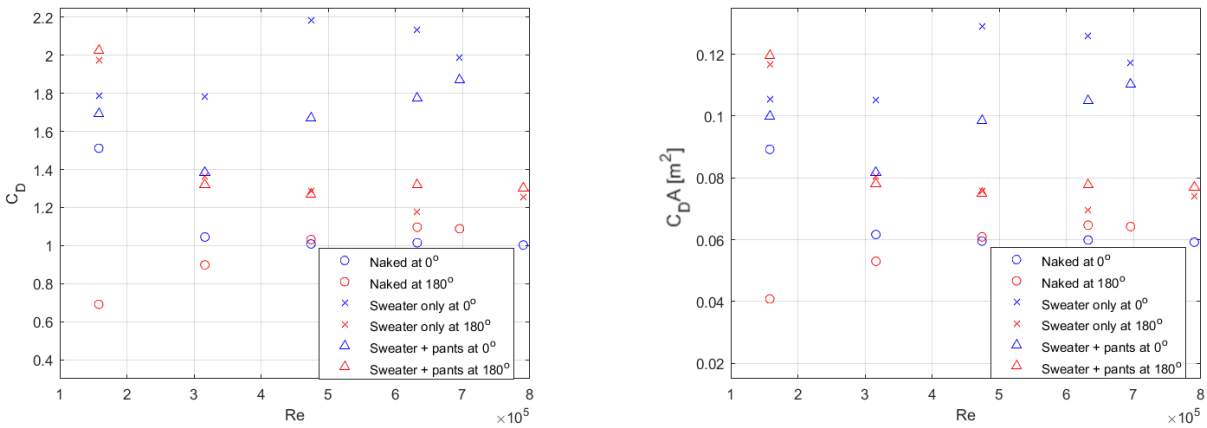

(a) C_D (b) $C_D A$

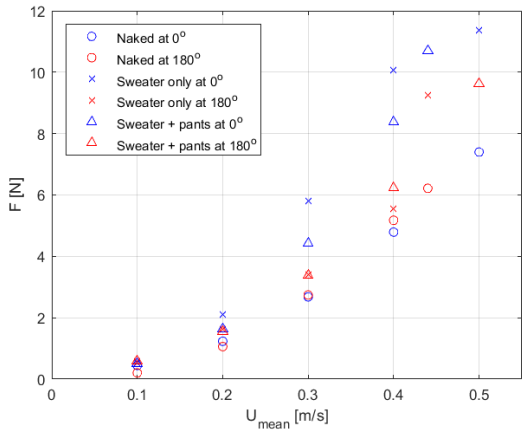

(c) $F_{measured}$

Figure 3.53: Results of the experiments in the towing tank

The movable structure is not able to go faster than 0.44 m/s when going backward. That is the reason why the last points are not aligned with all tests.

Forces measured at a velocity of 10 cm/s are not usable due to the range of the measured force which is lower than the accuracy of the system ($F_{measured} < 1$ N). Other results show limited scatter.

As in section 3.3.2, Table 3.13 is generated to summarise these figures.

Clothes	θ [°]	C_D	$C_D A$ $[m^2]$
None	0	1.05	0.062
None	180	1.05	0.062
Sweater	0	2.1	0.12
Sweater	180	1.25	0.074
Sweater and pants	0	1.8	0.105
Sweater and pants	180	1.25	0.074

Table 3.13: Drag coefficient levels

First, it is reminded that the estimation of C_D is challenging considering uncertainties on the estimated frontal area. These values are shown with the chosen $A_p = 0.059\ m^2$ but may change a lot with another estimation of the frontal area.

The level of drag coefficients for a naked model is the same for each direction of the motion, $C_D A \approx 0.06\ m^2$ and $C_D \approx 1.05$. Clothes raised the level by 20% when the head is upstream (180°) but their effect is more visible when the model's head is downstream (0°), drag coefficient increase by 70%. Indeed, water rushes in the sweater by the belly and back and the resistance to the motion raises. This effect is called "a parachute effect". Resistance is higher without a pants than with it. The presence of pants reduces drag of 15%. The main reason is that flow is disturbed when coming close to the pants and so the boundary layer is different. Furthermore, pants decreases the area available for water to enter in the sweater.

Future research is need for analysing the dependence of drag coefficient on velocity when the body is dressed.

3.3.4 Comparison between the different scale tests

The comparison between results of section 3.3.2 and 3.3.3 is not straightforward. The results are obtained with different models, of different material, in different flumes and flow conditions, and with different errors on the estimated areas.

This means that the comparison has to be done with all those differences in mind.

In order to reproduce conditions of the towing tank at best in the flume, tests have been undertaken with a body model in a similar position. They were realised with only one model, Bruce (Figure 3.54). It is the most similar model with the model used at real scale.

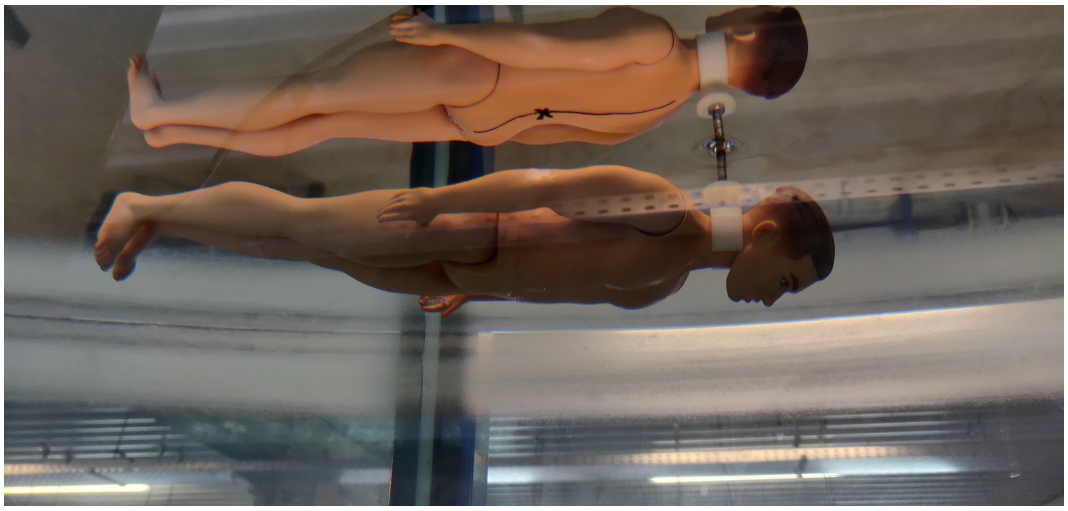

Figure 3.54: Bruce in the same position as in the towing tank

The frontal area is estimated exactly as in section 3.1.2.4 (Figure 3.55). The averaged area is $A_p = 0.003188\ m^2$ with horizontal limbs. The reference object is placed at the thickest part of the model in order to mitigate the distortion effects.

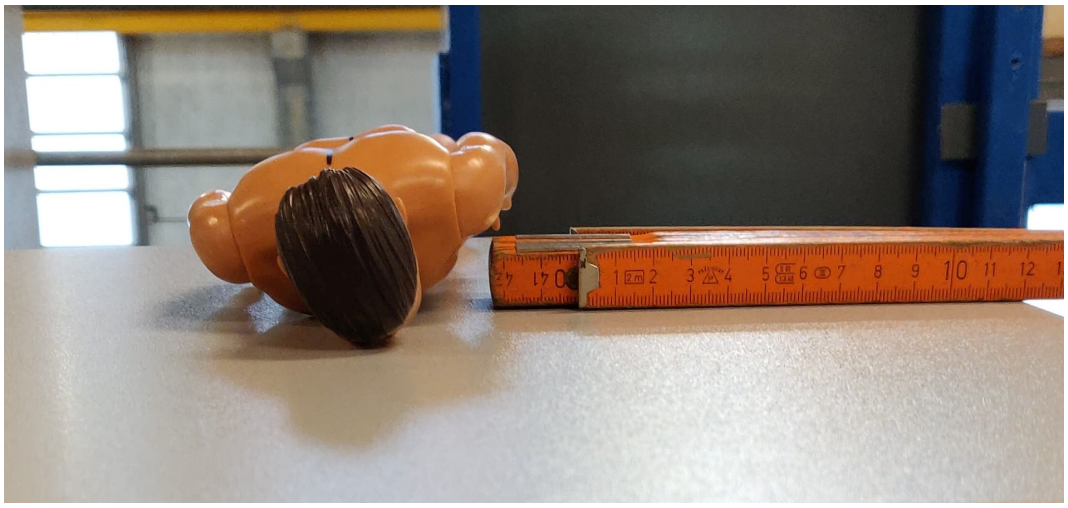

Figure 3.55: Bruce in the same position as in the towing tank, frontal area

The same procedure as in section 3.1.3.2 is followed to determined the two drag coefficients C_D and C_DA (Figure 3.57).

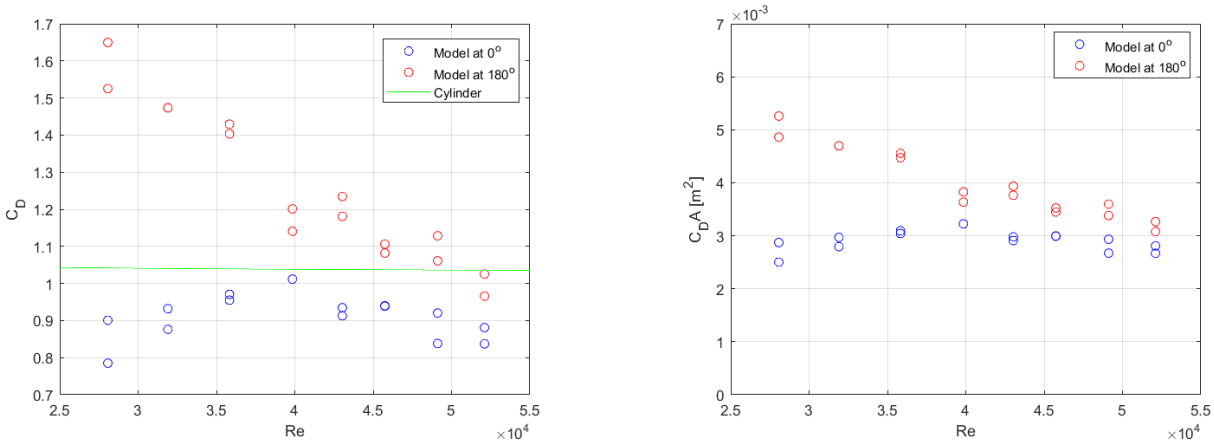

(a) C_D (b) C_DA

Figure 3.56: Drag coefficients in the towing tank position

The measurements with the model oriented at $\theta = 0^o$ show little variations while this is not the case for the other one. This variation is probably due to the importance of the buoyancy and vertical forces. Indeed, in this position, this buoyancy is the highest ever registered with our models (about 0.155 N). That means that it has a lot of importance on the measurement and a small error on its determination influences even more small forces like those at slow velocity.

The observation of the two levels of $C_D \approx 0.95$ and $C_D \approx 1.05$ are very close to what was observed in the towing tank.

C_DA are compared for the cases of a naked model in a similar position as in the towing tank and the studied position in the flume. The study is realised with Bruce. Levels of C_DA of this model are compared in Table 3.14.

Bruce	C_D	C_DA $[m^2]$
Vertical limbs	1.7	0.015
Horizontal limbs	1	0.0031

Table 3.14: Influence of limbs hanging down

For this comparison, the conditions are exactly the same except for the model's position. This comparison is more robust than the one made with test at scale 1:1. However, it comes to the same conclusion that limbs hanging down increase the drag. Limbs hanging down increase drag by 70%. A further study should provide quantitative results in addition to the qualitative ones.

Consequently, tests with clothes were realised. The goal is the same by confirming the observed phenomenon in the towing tank but this time in the same flume. These tests faced a practical problem. To work with the same body shape as at real scale, the chosen model is Bruce. However, his clothes are very opened and there is not enough matter to observe their influence. As a result, Bruce has thus been dressed with Hagrid's sweater, which was over-sized for him (Figure 3.57). It has been decided to keep this configuration as the goal is to show the parachute effect, which is amplified by over-sized clothes.

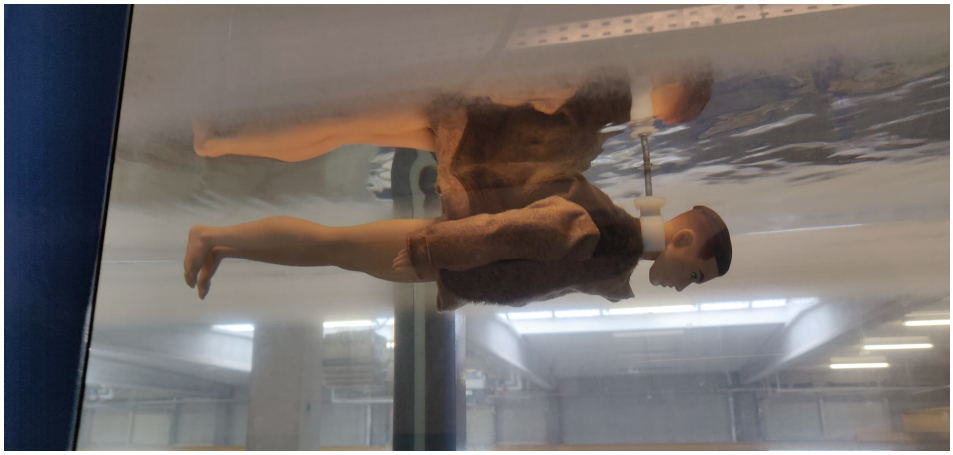

Figure 3.57: Bruce dressed with Hagrid's clothes

Considering the goal, less tests are realised in the above mentioned conditions. However, results are exactly as expected (Figure 3.59).

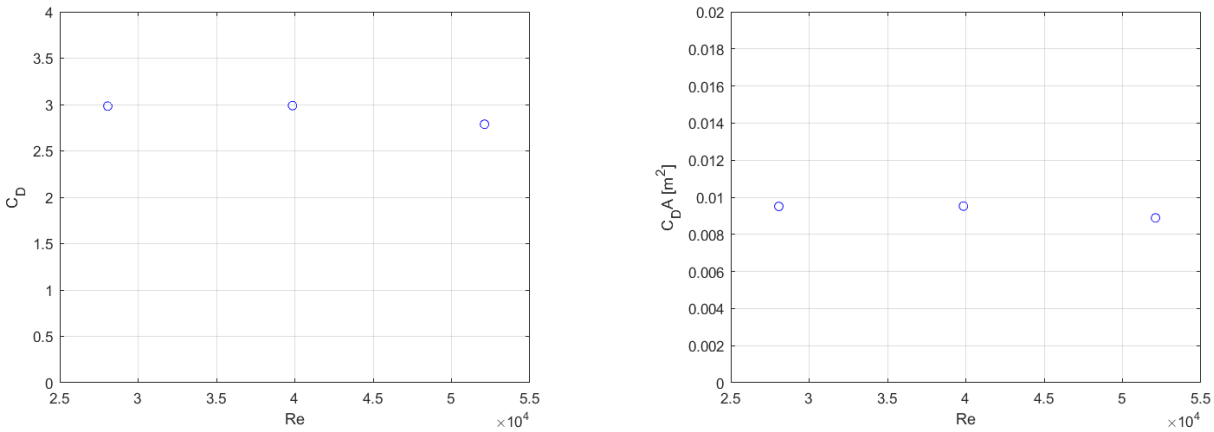

(a) C_D (b) $C_D A$

Figure 3.58: Parachute effect on drag coefficients

Clothes have an effect on drag. $C_D A$ is almost tripled by the presence of the sweater (Figure 3.60). The same influence is observed on C_D considering that clothes do not change the frontal area. These results combined to Figure 3.59 show that the parachute effect can be observed in the flume and it can be studied.

Figure 3.59: Parachute effect on the model

What comes out of this comparison is the need of taking into account limbs position and clothes on drag. They could be taken into account by modifying the frontal area or considering another drag coefficient C_D. Both have to be considered for the influence of limbs because area is changed but interaction flow-body is changed on the flow too. However, the influence of clothes should only be considered on drag coefficient because frontal area is not constant with time. A modification of only drag coefficient C_D depending on the type of clothes is easier.

3.4 Conclusion

The work is realised with 3 models at a scale of about 1/6 from the real size of a human body and one at real scale with the objective of establishing a drag coefficient for a drifting body. The 3 small body models are placed in a position determined from the literature and all characteristics are taken with some uncertainties which were quantified. The Re in the flume is between $6.8 * 10^4$ and $1.3 * 10^5$ with a particle Reynolds between $Re_p = 2.8 * 10^4$ and $Re_p = 5.2 * 10^4$ for the models. The Fr is very low and always stays below 0.07 in our cases while the measured height is about the same on all the flume for each discharge and is $h = 0.64\ m$.

The cross sectional velocity profile of the flume is determined thanks to the ADVP. The velocity is almost constant along the flume's width and a dip phenomenon is identified.

Some measuring systems are used to finally find one system which is accurate enough. The measuring system consists in a lever arm connected to a strain gauge to get a force.

The frequency and duration of sampling are determined by doing a convergence analysis. It has been shown that taking 401 values at a frequency of about 11.11 Hz and neglecting the first 50th measurements allows considering the average of the data set as representative.

The efficiency of our measuring system is tested with a cylinder. The results from the measurement system on the cylinder matched the results from the literature. It has been decided to evaluate the drag coefficients with the average water velocity even if the precised water velocity is known.

It is shown through our measurements done with 3 body models that there is a level of drag coefficients for our range of Re_p at some inaccuracies due to the low forces ($F \approx 0.1$N) with a strain gauge designed for forces around 5N. The importance of knowing accurately the frontal area of each model is highlighted. It has been deduced that the orientation has not a lot of influence on the drag coefficient C_D, conversely to the coefficient $C_D A$. It is highlighted in Table 3.12 that drag depends on the body shape but is greater than the one of a cylinder for each body shape.

A automatic transverse system is tested to attempt lower Re_p but forces are so small that results are impossible to analyse.

Experiments at scale 1:1 were done at an attainable range of Re_p which is different from the one tested in the flume. The orientation of the body influences a lot its drag if the body is dressed (raise by 70%) because water enters in the clothes. These results were reproduced in the flume and the hypothesis on influencing parameters are confirmed.

4 | Numerical modelling

In this chapter, a first simple drift model is presented. It can be seen as a toy-model, discretised in 1D, and applied to the case of the drift of body models (dummies) in the laboratory flume considered in Chapter 3. The modelling approaches discussed in this chapter are very exploratory. They aim mainly at investigation directions which would deserve further analysis in future modelling initiatives. As such, extending the toy model to real-world, multidimensional flow configurations is part of future work, and it lies beyond the scope of the present master thesis.

A three-step procedure was followed:

- schematisation of the body models (section 4.1),
- formulation of equations of motion (section 4.2),
- determination of the flow characteristics in the laboratory flume (section 4.3).

The results are presented and discussed in section 4.4.

4.1 Schematisation of the body models

Drift of a complex shape has not been studied and a first step is to determine how it has to be discretised. In this study three different kinds of discretisation and their influence on the body motion are compared.

4.1.1 Pointwise approximation

The first discretisation of the body is considering the body as its centre of mass. However, bodies are considered with homogeneous repartition of mass and so the centre of mass is the geometric centre (GC). The goal of this representation is to simplify the body at the maximum while gathering the properties of the actual body shape into coefficients. This simplification allows us to consider only one point in motion but the density, drag coefficients and frontal areas of the whole body are considered in the equations.

The problem with this is that a rotation can not be generated. Indeed, even if the inertia of the body is kept, forces are considered only at the mass centre and a moment can not be computed. This may be a real problem. Our study on drag coefficients C_D and $C_D A$ showed that even if the drag coefficient C_D seemed to be constant, this is not the case for the $C_D A$. This emphasizes that the applied force on the body by the fluid depends on its orientation.

In other words, the position of the body depends on its orientation at all time and a pointwise discretisation can not characterise the orientation.

4.1.2 Simplified shape

This discretisation consists in an idealisation of the body by means of a combination of simple shapes. Indeed, a human body may be compared to such a combination with reasonable similarities. Both arms and legs can be approximated as vertical cylinders while the chest resembles to a box with a determined pitch angle of 30° in the present case and, finally, the head can be idealised as a cylinder aligned with the chest.

In such an idealisation, cylinders representing the arms are fixed to the chest in a suitable way to represent the shoulders. The back of the box combined with the legs position enables representing the buttocks of the body and the head is considered as thick as the chest. Each shape is placed considering the position of the geometric centre. Then, the position of the geometric centre of each of them depends on the different dimensions of the human shape.

Length of chest, head and limbs are computed as a percentage of the total body length. A similar study to this one was already realised by many searchers and the similarity can be done with our dummies as they have the same proportions as a human body (Hora et al., 2017; Muhammad Saqlain et al., 2020). Furthermore, these lengths are similar to the one measured on the 1:6 scale models.

The result of this simplification is displayed in Figure 4.1:

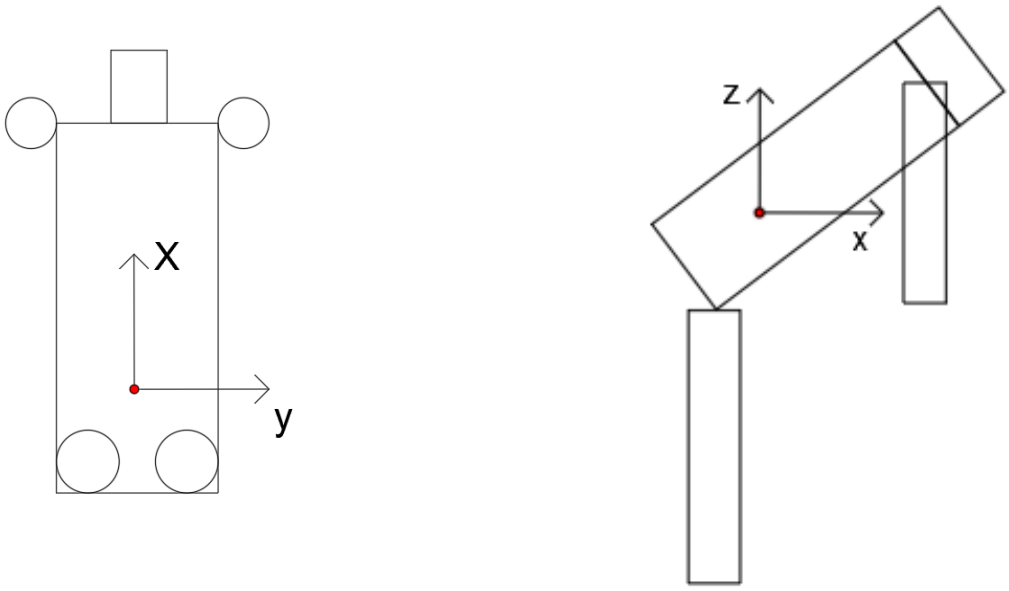

Figure 4.1: Idealisation of a human body as a combination of simple shapes

The points considered in the modelling are the geometric centre of each shape, as represented in Figure 4.2:

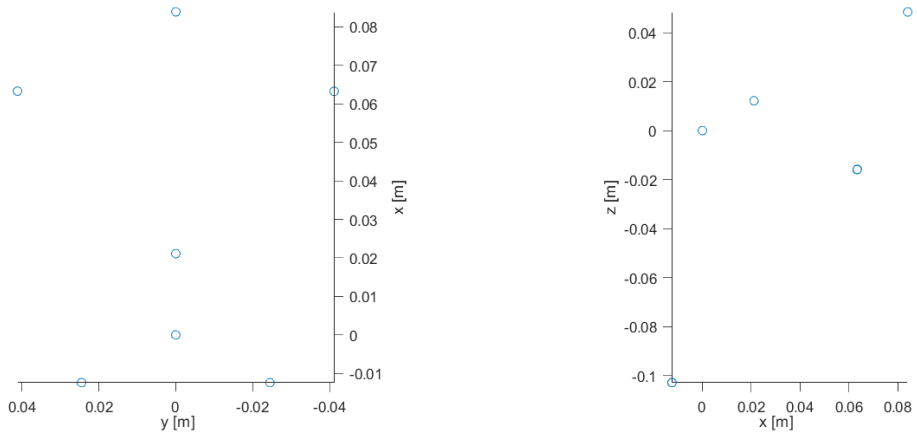

Figure 4.2: Geometric centres of simple shapes

The goal of this simplification is to calculate a resulting applied force $\overrightarrow{F}$ at each time step knowing that each shape is submitted to a different force. This is due to the fact that they move at a different velocity (non-uniform flow and $\dot{\theta} \neq 0$ rad/s) and they have different frontal areas. Indeed, a rigid body can have its parts moving at a different velocity. An simple example can be the example of a non-slip rolling wheel (Figure 4.3) where three points have a different velocity due to the linear velocity and the angular velocity $\dot{\theta}$.

- Red arrow: Point of contact, $\overrightarrow{U} = \overrightarrow{U}_{linear} - \overrightarrow{R} \wedge \overrightarrow{\dot{\theta}} = \overrightarrow{0}$
- Green arrow: Geometric centre, $\overrightarrow{U} = \overrightarrow{U}_{linear}$
- Blue arrow: Top of the wheel, $\overrightarrow{U} = \overrightarrow{U}_{linear} + \overrightarrow{R} \wedge \overrightarrow{\dot{\theta}} = 2\overrightarrow{U}_{linear}$

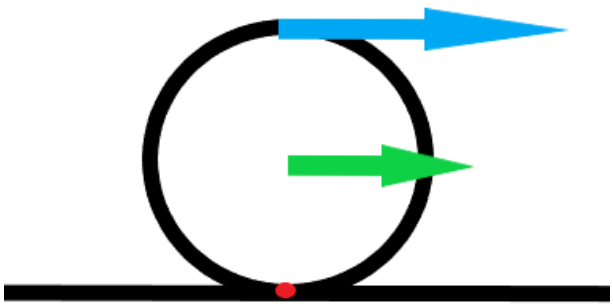

Figure 4.3: Example of a non-slip rolling wheel

Then, the resulting forces on the whole body can be deduced at each time step and compared to what was measured in the laboratory.

$$\overrightarrow{F}_{body} = \sum_{shape} \overrightarrow{F}_{shape} \tag{4.1}$$

In contrast with a pointwise representation, this discretisation allows the characterisation of the body rotation.

To predict the rotation motion, the body inertia around *z*, I_z, needs to be calculated. To this end, the mass of each part of the body needs to be determined. As a simplification, it was considered that the body density is homogeneous and the ratio of limb, chest and head mass and body mass is the same as the ratio of limb volume and body volume. This is contradictory to the assumption of different density made in section 3.1.2.3 but as the quantitative density of each limb, chest and head are not known for a dead body, the assumption of equal densities is kept for the estimation of inertia.

$$\frac{m_{limb}}{m_{body}} = \frac{V_{limb}}{V_{body}} \tag{4.2}$$

As we work with simple shapes to represent limbs, the volume of each of them and the total volume of the body can be easily calculated. It can be seen in table 4.1 that estimations are very close to measurements.

Model	V estimated in lab [L]	V calculated with simple shapes [L]
Hagrid	0.54 $\pm$ 0.05	0.59
Bruce	0.485 $\pm$ 0.05	0.54
Charlie	0.32 $\pm$ 0.05	0.39

Table 4.1: Comparison between the measured and estimated volumes

The inertia around the *z* axis can now be easily evaluated when the distance R between each point and the geometric centre in the xy plane is known.

$$I_z = \sum_{shape} m_{shape} R^2_{shape} \tag{4.3}$$

This simplification has plenty of advantages. It allows the pitch angle of the chest to move in time while keeping arms and limbs verticals and it changes the study of a very complex shape to simple shapes with the only requirements of estimating a limited number of dimensions of the real body.

Such a body modelling could be achieved with only basic data of a real drowning victim. Indeed Nucara et al. (2012), Tanabe et al. (2000) and Tikuisis et al. (2001) calculated the Body Surface Area (BSA) of a body as a function of its mass and height only. A similar procedure could be followed with the work of Muhammad Saqlain et al. (2020) to derive all the properties of the model proposed here, based on height and weight of the victim.

4.2 Equations of motion

4.2.1 Translation

The dynamic equilibrium is currently written with only one kind of force, drag due to primary and secondary flows. Indeed, other forces have not been studied and are not known yet, Equation 2.5 is taken with $C_S = 0$ in a stationary flow.

$$(m_b + \frac{1}{2}C_{AM}m_f)\ddot{\overrightarrow{X}} = \sum_s \frac{1}{2}\rho_w(\overrightarrow{U_w} - \dot{\overrightarrow{X}}_s) \cdot |\overrightarrow{U_w} - \dot{\overrightarrow{X}}_s| C_{D,s}A_{p,s} \tag{4.4}$$

with m_b the body mass, C_{AM} the added mass coefficient, m_f the mass of the fluid, $\overrightarrow{X}$ the general position in $(x; y; z)$, $\overrightarrow{U_w}$ the water velocity, C_D the drag coefficient and $A_{p,s}$ the frontal area.

Index s is used to show the kind of discretisation that is used, as developed in section 4.1. This index s stands for the shape on which you apply the force. So s is useless for the point-wise discretisation (Geometric Centre as the chosen point, GC) as $\overrightarrow{X}$, C_D and A_p are the one of the whole body. But the index s is useful for the Simplified Shape Discretisation (SS) and it refers to each shape.C_{AM} is not known and is put to zero in each simulation of section 4.4 but not for the simulations where $C_{AM} = 1$.

$\ddot{X}_0$ can then be deduced with initial conditions of X_0 and $\dot{X}_0$.

$$\ddot{\overrightarrow{X}}_0 = \frac{\sum_s \rho_w(\overrightarrow{U_w} - \dot{\overrightarrow{X}}_{s,0}) \cdot |\overrightarrow{U_w} - \dot{\overrightarrow{X}}_{s,0}| C_{D,s}A_{p,s}}{2m} \tag{4.5}$$

$\overrightarrow{X_i}$ and $\dot{\overrightarrow{X}}_i$ with the assumption of a uniformly accelerated rectilinear motion over the duration of one time step Δt.

$$\overrightarrow{X_i} = \overrightarrow{X}_{i-1} + \Delta t \dot{\overrightarrow{X}}_{i-1} + \frac{1}{2}\Delta t^2 \ddot{\overrightarrow{X}}_{i-1} \tag{4.6}$$

$$\dot{\overrightarrow{X}}_i = \dot{\overrightarrow{X}}_{i-1} + \ddot{\overrightarrow{X}}_{i-1}\Delta t \tag{4.7}$$

$$\ddot{\overrightarrow{X}}_i = \frac{\sum_s \rho_w(\overrightarrow{U_w} - \dot{\overrightarrow{X}}_{i,s}) \cdot |\overrightarrow{U_w} - \dot{\overrightarrow{X}}_{i,s}| C_D A_{p,s}}{2m} \tag{4.8}$$

With the set of Equations 4.6, 4.7, 4.8 and initial conditions on position and velocity, it is an explicit scheme of motion.

This scheme can be adapted to the simulations realised in section 4.4. In this section, motion in *y* and *z* are blocked as much as rotation. The set of Equations 4.4, 4.6, 4.7, 4.8 and initial conditions are solved with $\overrightarrow{X} =$ the motion along the streamwise direction:

$$\overrightarrow{X} = \overrightarrow{x} \tag{4.9}$$

4.2.2 Rotation

To determine the evolution of the angle θ over time, a moment balance has to be done.

$$I_z\ddot{\theta} = \sum_s \overrightarrow{F}_s \wedge \overrightarrow{R}_s \tag{4.10}$$

with I_z the inertia of the body around *z*, $\ddot{\theta}$ the angular acceleration of the body, s the considered point, $\overrightarrow{F}_s$ a force applied on the point and $\overrightarrow{R}_s$ the translation between the geometric centre and the studied point s.

The inertia of the body and $\overrightarrow{R}_s$ are approximated thanks to the simplification in simplified shapes developed in section 4.1.2.

Once again, the only forces used in this equilibrium are drag forces due to primary and secondary flows.

The moment balance can be repeated for the initial conditions of position and velocity.

$$\ddot{\theta}_0 = \frac{\sum_s \overrightarrow{F}_{s,0} \wedge \overrightarrow{R}_{s,0}}{I_z} \tag{4.11}$$

$$\overrightarrow{F}_s = \frac{1}{2}\rho_w[\overrightarrow{U}_w - (\dot{\overrightarrow{X}} + \dot{\theta} \wedge \overrightarrow{R}_s)]^2 C_{D,s} A_{p,s} \tag{4.12}$$

As for the equations of motion, the use of the index s enables to consider each kind of discretisation used as in section 4.2.1.

Finally θ_i and $\dot{\theta}_i$ are obtained with the assumption of a uniformly accelerated rectilinear motion over the duration of one time step Δt.

$$\theta_i = \theta_{i-1} + \Delta t\dot{\theta}_{i-1} + \frac{1}{2}\Delta t^2\ddot{\theta}_{i-1} \tag{4.13}$$

$$\dot{\theta}_i = \dot{\theta}_{i-1} + \ddot{\theta}_{i-1}\Delta t \tag{4.14}$$

$$\ddot{\theta}_i = \frac{\sum_s F_{s,i-1} \wedge R_{s,i-1}}{I_z} \tag{4.15}$$

With the set of equations 4.13, 4.14, 4.15 and initial conditions on position and velocity, it is an explicit scheme of determination for the angle θ.

As the rotation is blocked in section 4.4, these equations are not used in the analysed simulations. However, they are applied when the rotation is released (section 5.1.2).

4.3 Flow characteristic

In this section, we describe how the water surface profile in the considered laboratory flume was approximated based on a backwater calculation (section 4.3.1), as well as the selected parametrization of the velocity profile in each cross-section of the flume (section 4.3.2).

4.3.1 Flow depths

As a first approximation, the shallow water equations are assumed to apply to the gradually varied flow observed in the continuous straight laboratory flume. Neglecting lateral inflow or outflow , the equations are as follows.

$$\begin{aligned} &\frac{\partial \Omega}{\partial t} + \frac{\partial Q}{\partial x} = 0 \\ &\frac{\partial Q}{\partial t} + \frac{\partial \left(\beta \frac{Q^2}{\Omega}\right)}{\partial x} + g\Omega \frac{\partial z}{\partial x} + g\Omega J = 0 \end{aligned} \tag{4.16}$$

with Ω the cross section area, Q the discharge, t the time, β the Boussinesq coefficient, g the acceleration of gravity, *z* the free surface elevation and J the friction slope.

In the following, the Boussinesq coefficient is set to unity ($\beta = 1$) because the velocity profile is fairly close to uniform (see section 3.3.1). This is discussed in the next section.

Steady flow in the flume is assumed, as small fluctuations in the discharge are neglected. For instance, when a nominal discharge of $Q = 30$ l/s is set, the actual flow was measured at $Q = 30 \pm 0.3$ l/s. This corresponds to fluctuations of about 1% of the target value, which are ignored in the present model. Equation 4.16 reduces to:

$$\frac{dh}{dx} = \frac{-\frac{dz_b}{dx} - J + \left.\frac{Q^2}{g\Omega^3}\frac{d\Omega}{dx}\right|_h}{\cos\alpha \left[1 - \frac{U^2}{g\cos\alpha \frac{\Omega}{l}}\right]} \tag{4.17}$$

with h the flow depth, z_b the flow bottom elevation and α the mean slope of the channel.

Considering: flat bottom ($\alpha = 0$, z_b constant) and uniform cross section, Equation 4.17 further reduces to:

$$\frac{dh}{dx} = \frac{i - J}{1 - Fr^2} \tag{4.18}$$

To determine the friction slope J, Manning-Strickler's formula was used:

$$U_w = K J^{\frac{1}{2}} R_h^{\frac{2}{3}} \tag{4.19}$$

with U_w the mean flow velocity, K the friction coefficient and R_h the hydraulic radius.

From previous experiments in the same laboratory flume, the value of the friction coefficient K is estimated at $K = 114\ m^{1/3}/s$. To solve Equation 4.18, the flow discharge needs to be presented, as well as a boundary condition on the flow depth, either upstream or downstream, depending on the flow regime.

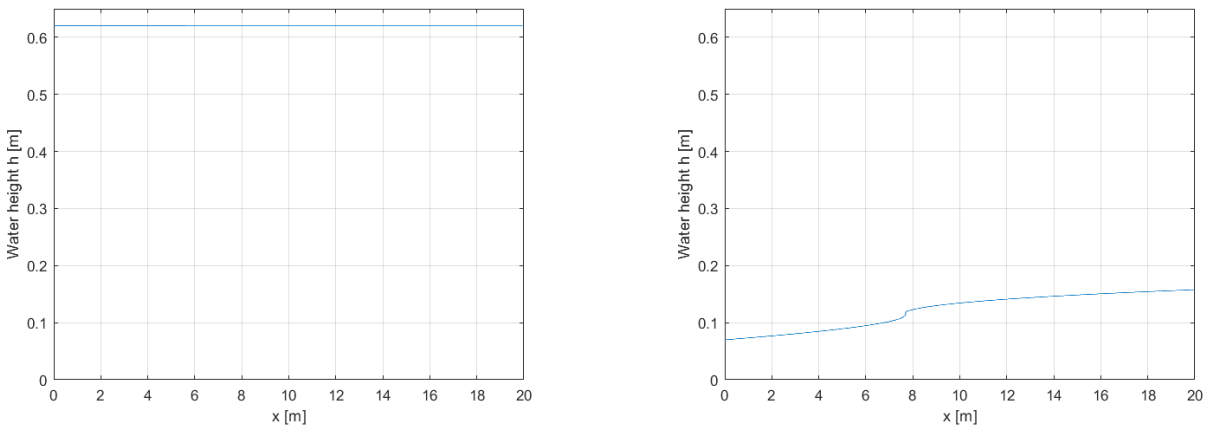

(a) $Q = 30$ l/s, $h_{down} = 0.62$ m

(b) $Q = 60$ l/s, $h_{up} = 0.07$ m

Figure 4.4: Results of the model of water lines calculation

Figure 4.4 shows two examples of computation. This computation is realised with a discharge of $Q = 30$ l/s, a downstream condition on depth $h_{down} = 0.62$ m and a slope $\alpha = 0\%$. This case is with little variation in the flow depth due to the limited flow resistance in the glass flume. This is consistent with the experimental observation. The second case is a passage from the supercritical regime (Fr>1) to the subcritical one (Fr<1) imposed with a discharge of $Q = 60$ l/s, an upstream condition on depth $h_{up} = 0.07$ m and a slope $\alpha = 0\%$. This case shows bigger variations in the flow depth due to the hydraulic jump. The flow depths and position of the hydraulic jump are consistent with the experimental observation.

4.3.2 Flow velocity

Since the flow computation described in section 4.3.1 is one-dimensional, it cannot be used to predict the velocity profile in the flow cross section. Hence this profile needs to be parametrized since it influences the body motion. The velocity profiles are discussed here for a particular discharge Q and prescribed flow depth h_{down}. $Q = 30$ l/s and $h_{down} = 0.62$ m. The focus is set on abscissia $x = 10$ m. We investigate first the velocity profile along the crosswise direction, and not along the vertical direction.

4.3.2.1 Assumed velocity profile in the crosswise direction

First, the kind of velocity profile that is used along *y* has to be determined. It is decided to compare three velocity profile: the average one, the Poiseuille one and the one fitted from the ADVP data. In the following, each kind of velocity profile, how it is computed, and its advantages and disadvantages are developed.

The goal of this comparison is to get the most realistic velocity profile because it rules the motion of a body. Indeed, each streamline is straight in our flume the motion of a big object is ruled by the differences in velocity between each of them (see figure 4.6). Indeed, the non uniformity of the velocity profile is linked to secondary currents, turbulence and wall friction and a good characterisation of the main flow results in a good approximation of the secondary ones. It is then tried to get the most realistic velocity profiles, avoiding inconsistencies between assumptions used for flow depth approximation and for flow velocity parametrization.

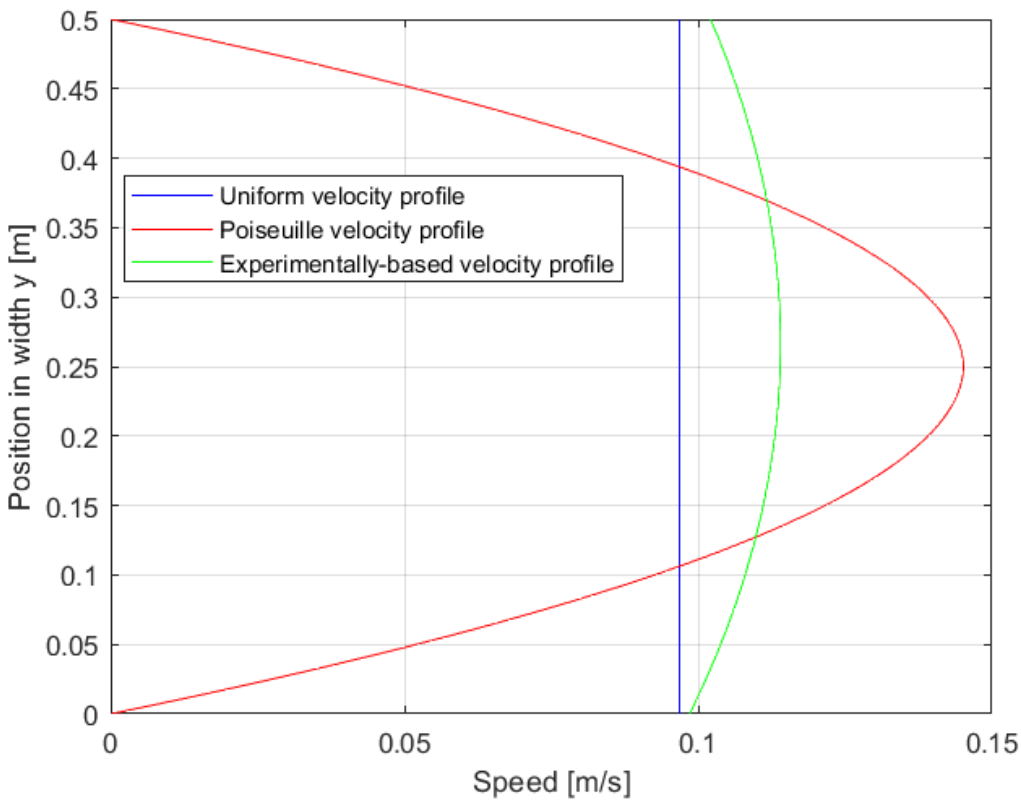

Figure 4.5: Three kinds of velocity profile along *y*

Three options are tested here for the parametrization of the velocity profile along the crosswise direction, as shown in Figure 4.5: (i) a uniform velocity profile corresponding to the cross-section averaged velocity, (ii) a Poiseuille-type profile and (iii) a profile based on a regression on the ADVP data.

The uniform velocity profile is simply calculated with the following formula:

$$U = \frac{Q}{lh_x} \tag{4.20}$$

with h_x the flow depth at position *x* and l the flume width.

The second considered velocity profile is the Poiseuille profile. This is a well known profile used for a laminar flow. This means that it is less suitable for this application because of the turbulent flow. Nonetheless we look at it for the sake of testing the sensitivity of the model predictions to strong variations in the crosswise profile of streamwise velocity. The Poiseuille profile writes:

$$U_P(y) = U_{\max}\left(\left|\frac{4y}{l}\right| - \frac{4y^2}{l^2}\right) \tag{4.21}$$

with U_{max} the maximum velocity along the flow at the width centre of the flume.

The parameter U_{max} can be easily related to the cross-sectional average of streamwise velocity, given that the discharge is constant and that a zero transverse slope is assumed. Following development is obtained from Equations 4.20 and 4.21:

$$\begin{aligned} Q &= \int_0^l h_x U_P(y) dy \\ lh_x U &= h_x U_{\max}\left[(\frac{4y^2}{2l} - \frac{4y^3}{3l^2})\right]_0^l \\ lh_x U &= \frac{2}{3} lh_x U_{\max} \\ U_{\max} &= \frac{3}{2} U \end{aligned} \tag{4.22}$$

The third considered velocity profile was determined in section 3.3.1. It is based on a linear regression of the measured data:

$$\begin{aligned} U_{30} &= -0.2178y^2 + 0.1018y + 0.1021;\ Q = 30\ l/s \\ U_{30} &= a_1 y^2 + b_1 y + c_1 \end{aligned} \tag{4.23}$$

$$\begin{aligned} U_{55.7} &= -0.5773y^2 + 0.2889y + 0.1673;\ Q = 55.7\ l/s \\ U_{55.7} &= a_2 y^2 + b_2 y + c_2 \end{aligned} \tag{4.24}$$

The measurements performed at mid-height were used here. The variations in the velocity profile with the elevation *z* are discussed in the next subsection.

Since the experimentally-based velocity profiles were determined for only two particular values of discharge, most numerical simulations will be conducted for these discharges. It is also possible to adapt the velocity profiles using linear interpolation:

$$\begin{aligned} d &= \frac{Q-30}{57.7-30} \\ a &= (1-d)*a_1 + d*a_2 \\ b &= (1-d)*b_1 + d*b_2 \\ c &= (1-d)*c_1 + d*c_2 \\ U &= ay^2 + by + c \end{aligned} \tag{4.25}$$

In order to improve the accuracy of this parametrization, additional ADVP measurements would be needed. For instance, measurements for a third discharge would allow us to perform a non-linear regression, such as a second-order polynomial.

It is now possible to analyse the motion along *x* of a cylinder placed in these 3 kinds of flow but considered constant in height (Figure 4.6).

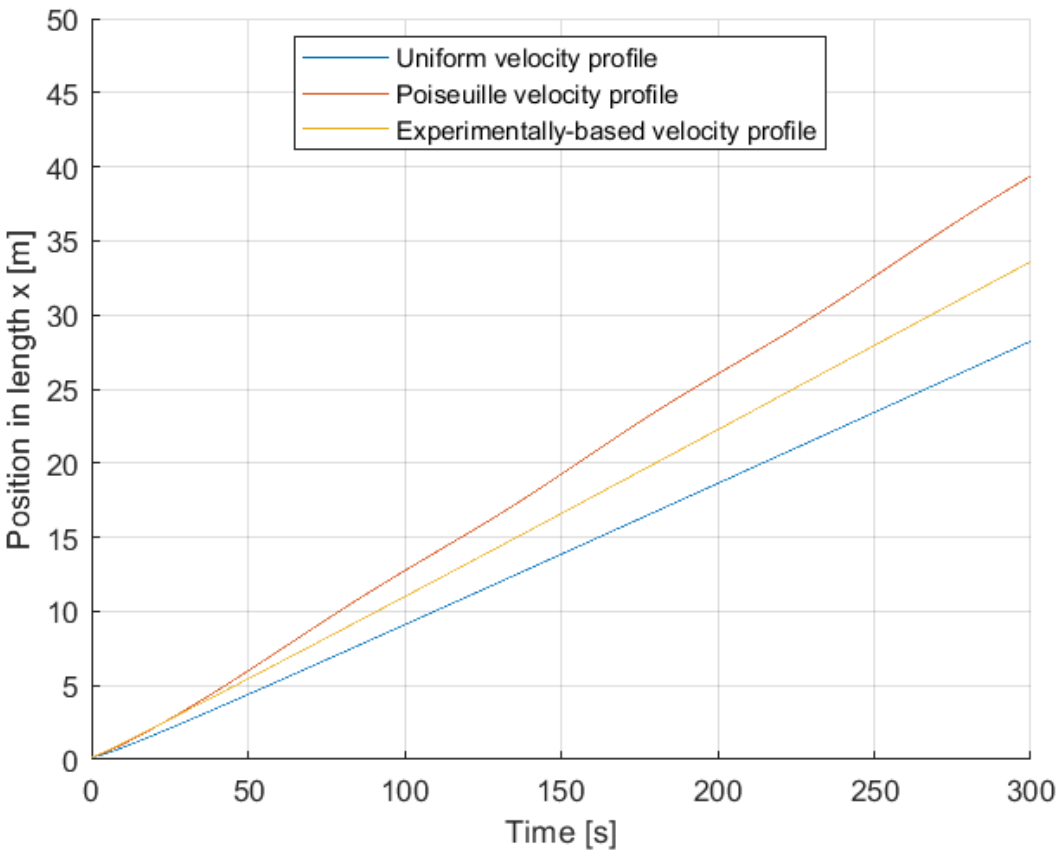

Figure 4.6: Comparison of the motion of a cylinder for each kind of flow with $\theta_0 = 0^o$

As expected, motions are very different from one velocity profile to another. An observation made on few tests realised in the laboratory confirmed that the motions with the Poiseuille flow do not correspond, as well as the uniform velocity flow. However, it is not possible to confirm that the motion generated by the realistic flow is the real one. As highlighted by Ghaffarian et al. (2020), the uncertainties on one motion are not insignificant and it is possible to have a different motion from one test to another with the same conditions. A way to proceed to get rid of these variations is to analyse the motion of the cylinder with a calibrated camera and to repeat the tests multiple times. Given that most of our time was spent to determine different coefficients of a human shape, time to follow their procedure of repeating multiple filmed tests has not been taken. Nevertheless, an observation made on a few tests leads us to the conclusion that the most suitable velocity profile along y is the one determined thanks to the ADVP.

4.3.2.2 Assumed velocity profile along the vertical direction

The velocity profile in height can now be determined. It has been decided to compare four velocity profiles (Figure 4.7): the uniform one, the logarithmic one, the dip phenomenon velocity profile found in literature and finally the adapted dip phenomenon velocity profile. Even if the velocity profile along y is already chosen, our simulations are realised with a uniform velocity profile along y in order to study only the influence of the vertical velocity profile.

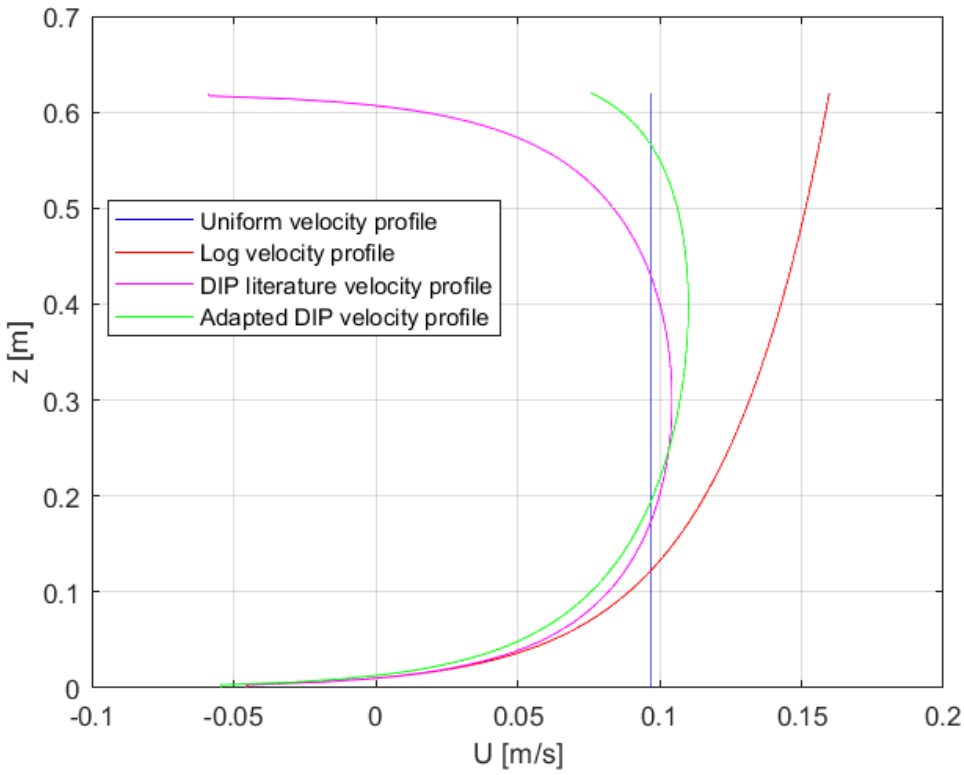

Figure 4.7: Four kinds of velocity profile along z

As in the velocity profile along y, the first analysed velocity profile is uniform in height. Its calculation is once again very easy but not exactly the same as the previous uniform profile.

$$U_z(x, y, z) = U_y(x, y);\ \forall z \tag{4.26}$$

Doing this calculation instead of eq. 4.20 gives us the opportunity to have any velocity profile along *y* and an averaged one along *z*.

This profile may be used if only the motion at the surface was needed with a precise determination of the velocity at this position. In this case, water velocity could be considered as uniform in height to simplify the model. However, our goal is to work beneath the surface at the border of this one and deeper. In addition to that, it is tried to model the motion of a human body shape which is not symmetric in height and takes up space along this axis because of its legs and arms. This is the reason why validation tests are done with a cylinder of large dimensions compared to the flume's one (reminder: $D = 0.11$ m, $L_{cyl} = 0.24$ m while $l_{flume} = 0.5$ m and $h \approx 0.62$ m).

The second velocity profile is the logarithmic profile with of following Equation 4.27:

$$U_{log} = \frac{1}{\kappa} \ln \frac{z}{z_0} \tag{4.27}$$

with $\kappa = 2.5$, the Von Karman constant and z_0 the height at which velocity is considered to be zero.

z_0 characterises the roughness of the bottom: the rougher the bottom, the higher the z_0 (Dey, 2014). In present case $z_0 = 1 * 10^{-2}$ which is higher than what was expected for a smooth plexiglass bottom. This value results of a regression with the experimental data. The fact that z_0 is different from zero explains why negative speeds are computed in Figure 4.7. Indeed, the logarithm of a value smaller than one is negative. In this case, when *z*$< z_0$, the computed speed is negative, which is a physical error due to mathematical analysis. However, in this work, we never work close to the bottom so this physical error is not problematic.

This profile would be the one used if we did not notice a dip phenomenon in our flume.

Research have been made to take into account the dip effect in the logarithmic law. Their results are compared to our adaptation of the dip phenomenon (Dey, 2014; Yang et al., 2004). Measurements showed that $U_y \approx \pm 10^{-3}$ m/s and $U_z \approx \pm 10^{-3}$ m/s but they are not relevant. It is considered that we are not able to determine them reliably because of their range compared to the accuracy of the ADVP and they are neglected. Nevertheless, they are linked to the dip phenomenon.

In the literature, the dip phenomenon is described as follows (Equation 4.28 and Figure 4.8):

$$\bar{u}^+ = \frac{1}{\kappa} \left[\ln \frac{\tilde{z}}{\tilde{z}_0} + \alpha \ln(1 - \tilde{z}) \right] \tag{4.28}$$

with $\bar{u}^+$ the log velocity divided by the shear velocity (obtained for us with Manning equation), $\kappa = 2.5$ Von Karman constant, z_0 the position at which $U = 0$, $\tilde{z}_0 = \frac{z_0}{h}$, $\tilde{z} = \frac{z}{h}$ and α the dip coefficient.

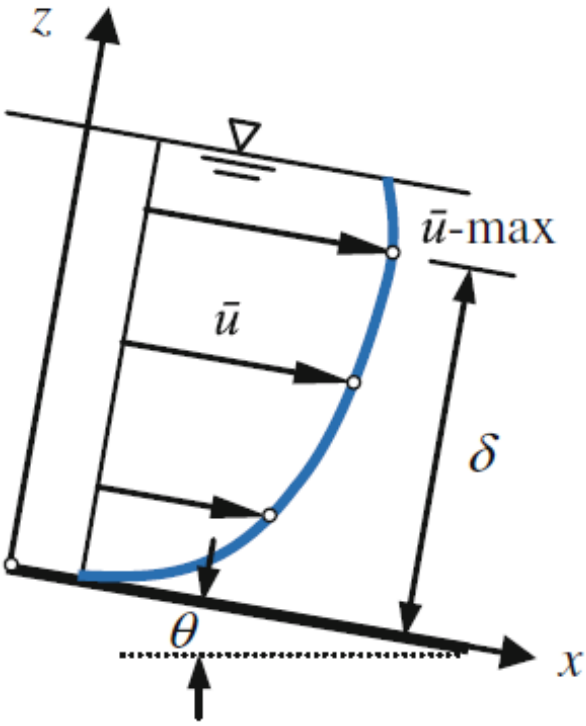

Figure 4.8: Velocity profile in the xz plane, dip phenomenon (Dey, 2014)

Equation 4.28 is the shape of the velocity profile considering the dip effect. This shape depends on two coefficients which are $\tilde{z}_0$ and α. These two are determined in order to have the same position and value of the maximum velocity as the measured one of section 3.1.3.1.

The dip coefficient has the following form:

$$\alpha = aexp(-\frac{y}{h}) \tag{4.29}$$

with a the coefficient which is adjusted, y the distance from the closest wall and h the flow depth.

In our case, $a = 0.95$ and $z_0 = 1.17 * 10^{-2}$. z_0 is different from the one obtained with the log ($z_0 = 1 * 10^{-2}$) and literature dip profile once again to fit at best our measurements. Furthermore, the term $\ln(1 - \tilde{z})$ is replaced by $\ln(1.05 - \tilde{z})$ to avoid the convergence to $-\infty$ when $\tilde{z} = 1$. In the studies from Yang et al. (2004) and Dey (2014), $a = 1.3$ but the position of the maximum velocity is about at mid height while our measurements showed us that this is not the case here. This is why it has been decided to adapt this coefficient α. Our flume is very smooth and so it is expected to have a z_0 closer to 0 than this one. Meaning that the bottom has a roughness of the order of 1 cm. However it is decided to keep this value as our area of study is far from the bottom and it is better to fit at best the measurements made with the ADVP.

Another point is that the eq. 4.28 is not correct close to the boundaries. Due to the two logarithm terms in this equation, $U = -\infty$ when $z = 0$ and $z = h$, where the equation does not apply.

The velocity profile obtained with our modified equations are shown in Figure 4.9. It can be seen that the equations are overall accurate at the lower discharge while it is less precise for the higher one. Results obtained with the ADVP show that the dip coefficient needs to be adapted with the discharge as the position of the maximum changes. However, the goal of this work is not to study the dip phenomenon in detail, so a constant dip coefficient is considered.

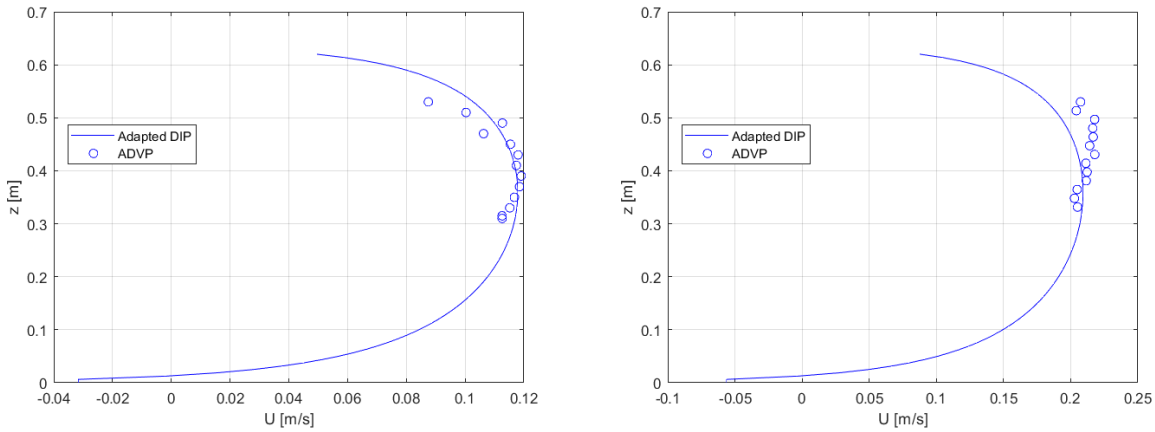

Figure 4.9: Dip phenomenon equations with ADVP measurements

It is now possible to analyse the motion of a cylinder placed in these 4 kinds of flow and decide which one to keep and why. Once again the motion along x is compared for an identical period of time in Figure 4.10.

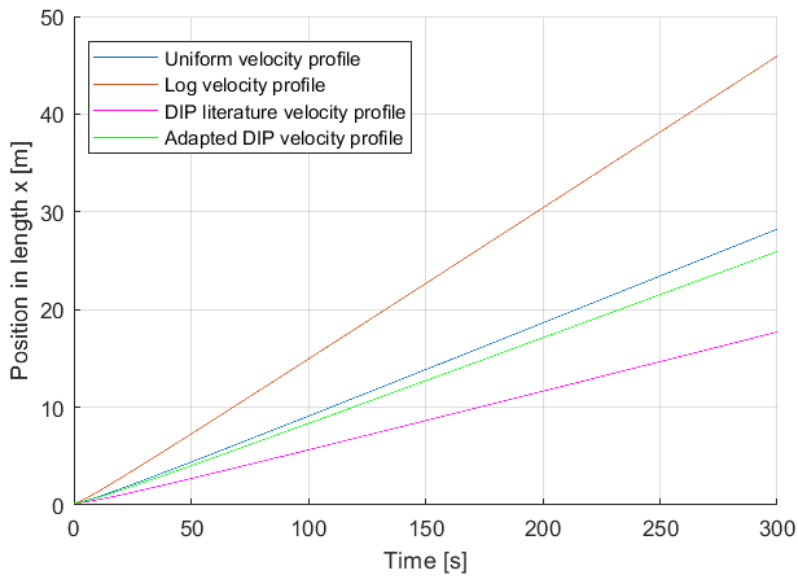

Figure 4.10: Comparison of the motion of a cylinder for each kind of flow with $\theta_0 = 0^o$

The above figure shows that each velocity is different. A bad choice of flow discretisation can lead to a difference of 25 m in the streamwise position of the body in only 300 s (150% of the actual motion). This demonstrates that a realistic 3D model of the flume flow is needed to model the motions at best.

It may be thought that these results are different only because water velocity at the surface is different. This is the reason why one more comparison is realised with two simple cases in Figure 4.11: average velocity profile and log profile which has its surface velocity equals to the average velocity.

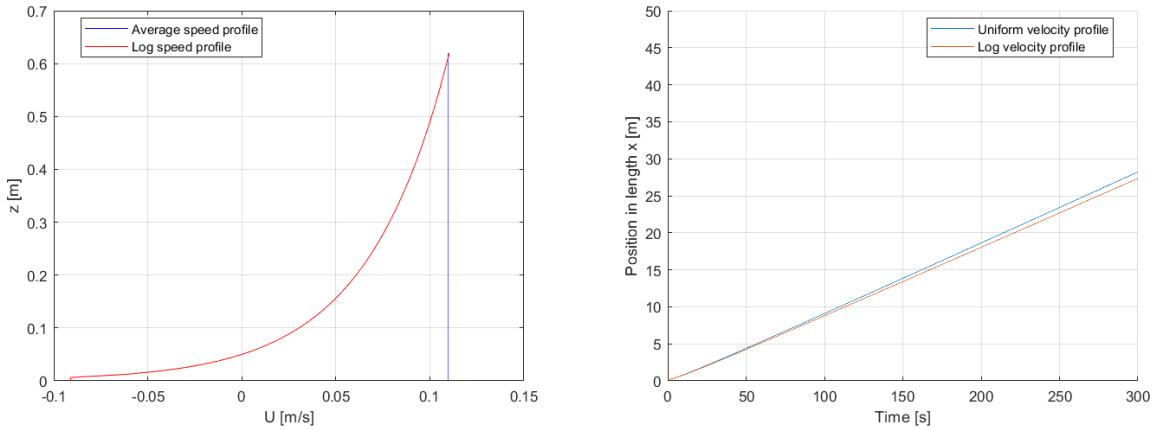

Figure 4.11: Comparison between two simple cases with the same velocity at the surface

This confirms that even if the velocity is the same at a point of interest, the motion of the body is different. Of course, the differences between the two of them are small but the fact that the final position differs of one meter confirms the need for an realistic profile.

To sum up, it is desirable to use the ADVP velocity profile along *y* with the adapted dip velocity profile along *z*. Nevertheless, this can not be done. The equation of the dip phenomenon depends on *y*, like the ADVP equation along *y*. The use of both of them would mean a repetition of the treatment of each data along width of the flume and so the model would be wrong. Taking a look at what is done with the adapted dip profile computed on an average profile along *y*, it is clear that only the dip treatment of data is enough (Figure 4.12).

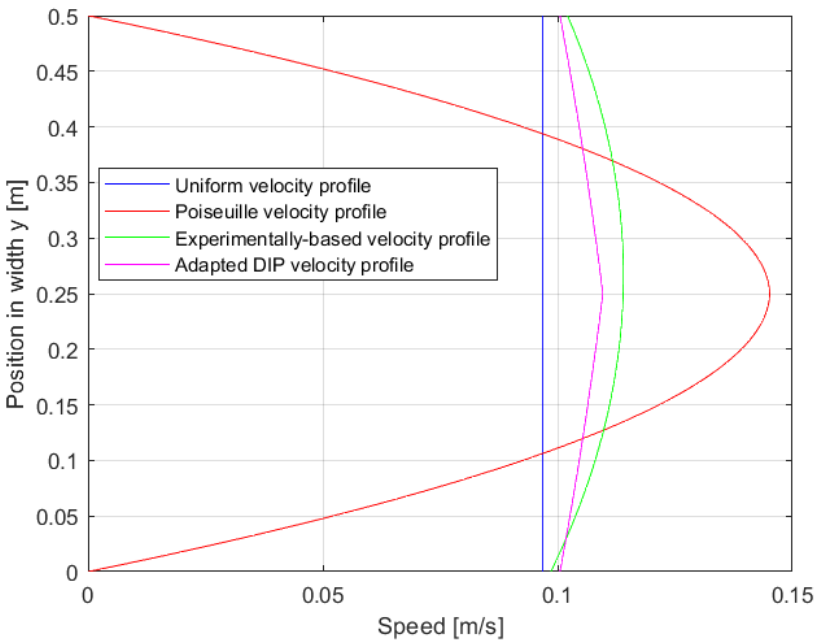

Figure 4.12: Comparison of the dip phenomenon with the speed profile along *y*

In conclusion, for our model, the adapted dip velocity profile is kept as the velocity profile in the *yz* plane; it is known that to be more accurate, measurements should be done on the whole velocity profile as well as at the surface thanks to a method of tracing particles.

Note that, while the shape of the streamwise velocity profile was analysed, the two other velocity components are simply set at zero.

$$\begin{aligned} U_{w,x} &= U_{DIP} \\ U_{w,y} &= 0 \\ U_{w,z} &= 0 \end{aligned} \tag{4.30}$$

4.4 Results

4.4.1 Streamwise body motion

Different motions are compared for each model and kind of discretisation. The motion along *y* and rotation θ are blocked because it is a one-dimensional study.

The simulation is realised with a discharge of $Q = 30$ l/s, a prescribed downstream flow depth $h_{down} = 0.62$ m, spatial step $(dx; dy; dz) = (0.02; 0.025; \approx 0.0062)$[1], $t_{simulation} = 300$ s, a time step $dt = 0.015$ s and a cylinder placed at the following position (Figure 4.13):

$$\begin{aligned} x_{GC} &= 0.2\ m \\ y_{GC} &= 0.15\ m \\ z_{GC} &= z_{surface} - \frac{D}{2} = 0.565\ m \\ \theta &= 0^o \end{aligned} \tag{4.31}$$

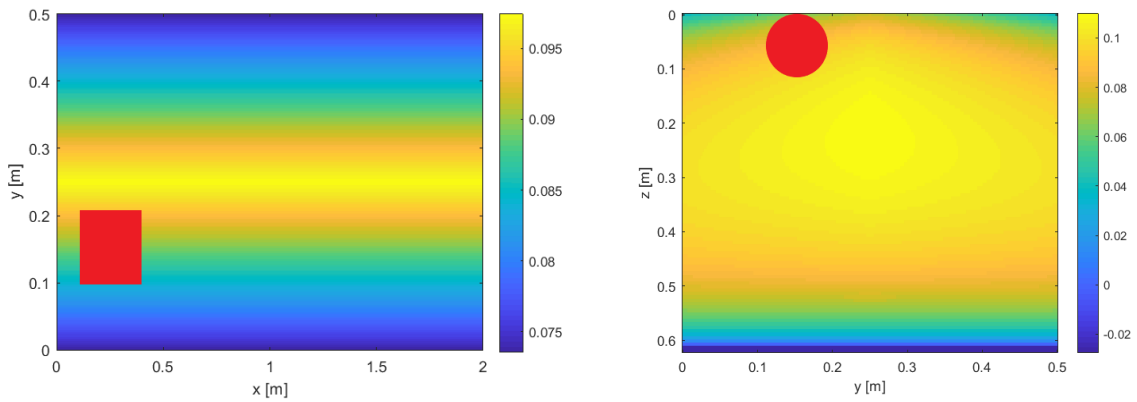

Figure 4.13: Initial conditions

Two cases are compared:

- The pointwise discretisation considering only drag
- The pointwise discretisation with $C_{AM} = 1$ (Ghaffarian et al., 2020)

The goal of the second case is to determine if the added mass C_{AM} has a big influence on a long term motion.

Of course, the case of a simulation by simplifying the shape into more simple ones is impossible to reproduce with a cylinder as it is already a simple shape.

[1]The different spatial steps are determined deciding the number of element by dimension. Along *x* and *y*, this value is constant because length and width are constant. However flow depth changes along *x* and so dz changes too.

We are now able to analyse its motion along x in Figure 4.14.

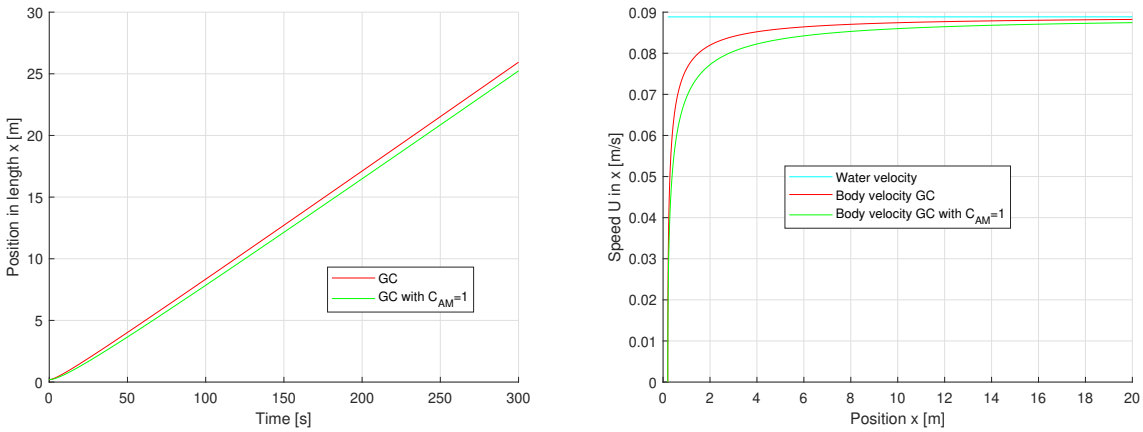

Figure 4.14: Position and velocity of the cylinder

The influence of the added mass is analysed. This influence decreases when the cylinder reaches water velocity. The first graph shows that at low water velocity the distance between the two cases is smaller than 1 m after 500 s. Furthermore, the other graph shows that both cylinders quickly reach water velocity and so the difference between the two positions will stay of about 1 m or less.

The same analysis can now be done with our human shapes. The flow and initial conditions (Figure 4.15) are the same as for the cylinder:

$$\begin{aligned} x_{GC} &= 0.2\ m \\ y_{GC} &= 0.15\ m \\ z_{GC} &= z_{surface} - \frac{L}{4} \approx 0.565\ m \\ \theta_0 &= 0^o \end{aligned} \tag{4.32}$$

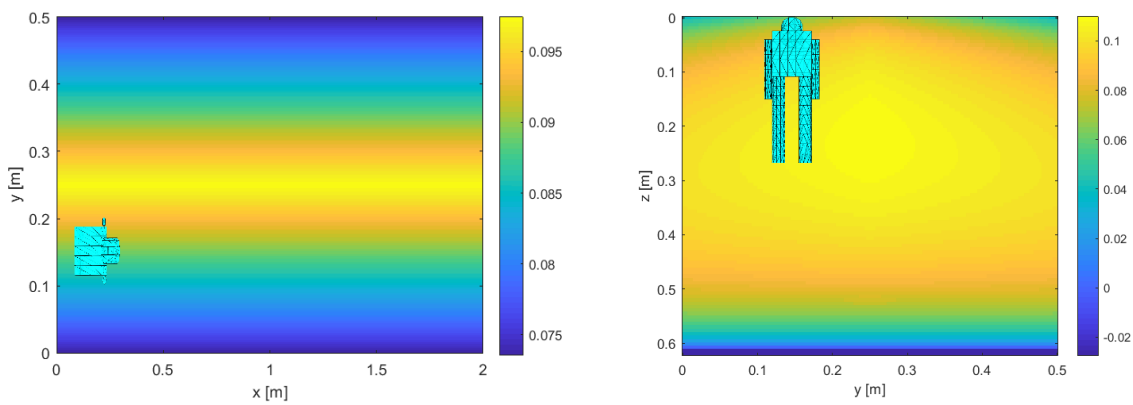

Figure 4.15: Initial conditions

Each model is compared to the others and to the cylinder. GC is used for geometric centre discretisation while SS means Simplified Shapes. The results are displayed in Figure 4.16[2]:

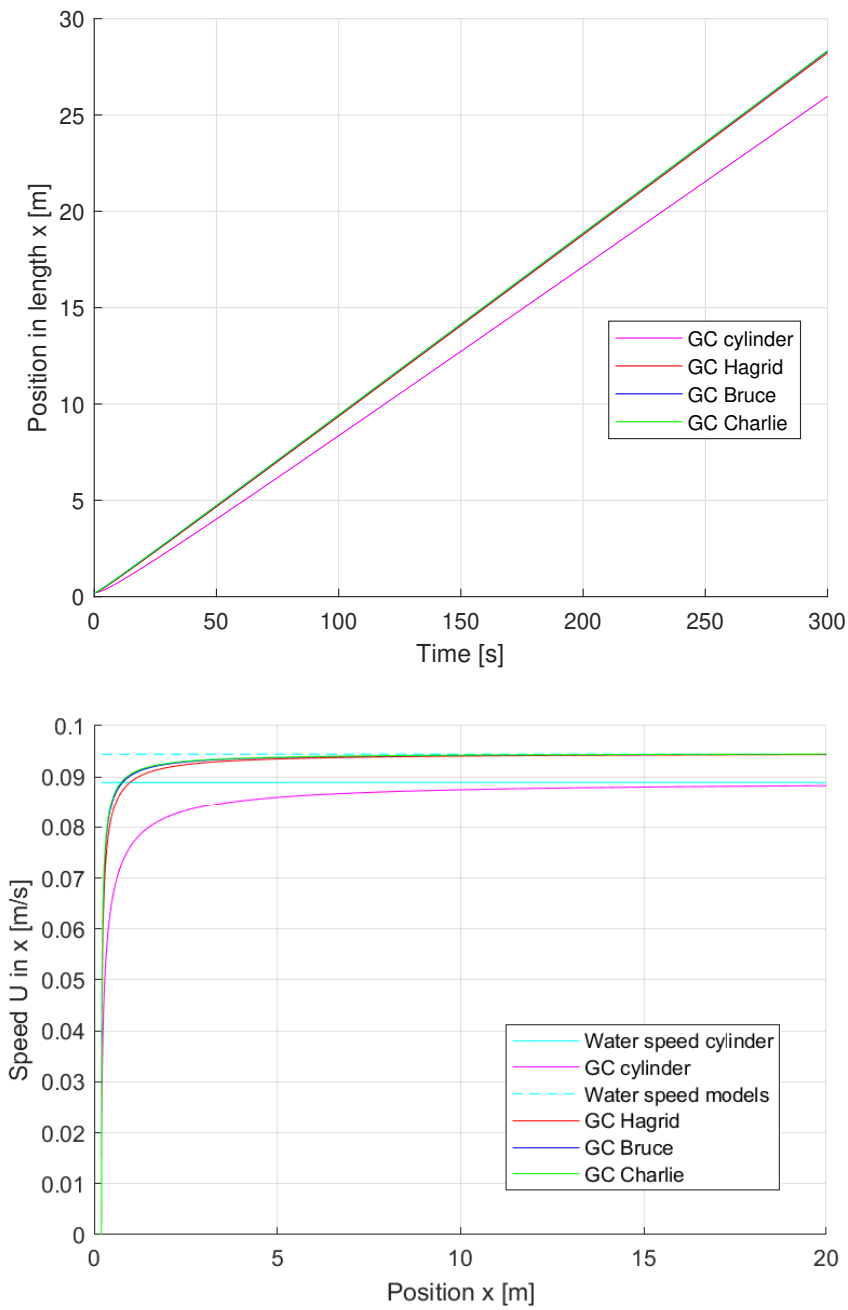

Figure 4.16: Simulation with pointwise discretisation (GC)

Since the flow velocity differs for the cylinder and for the models, their motion through time changes too. This is explained by the different position of the geometric centre in height. Indeed, the cylinder near the surface has its geometric centre higher than each of the models. This, coupled to the fact that there is a dip phenomenon and all GC are higher than the point of maximum velocity, leads to the fact that water velocity is lower for the cylinder (see Figure 4.15 for the positions of the maximum velocity and geometric centre).

[2]Body velocity are hidden for $x > 20\ m$ because it is considered that these data do not show anything useful.

Moreover, models have a higher drag coefficient than the cylinder. This leads to a stronger acceleration and so body velocity reaches faster water velocity. In this case, it could be said that velocities are approximately the same after 3 m for each model. Indeed, at an orientation of $\theta = 0^o$, all bodies have approximately the same velocity through time.

The following Figure 4.17 shows the same simulation but with the Simplified Shapes discretisation.

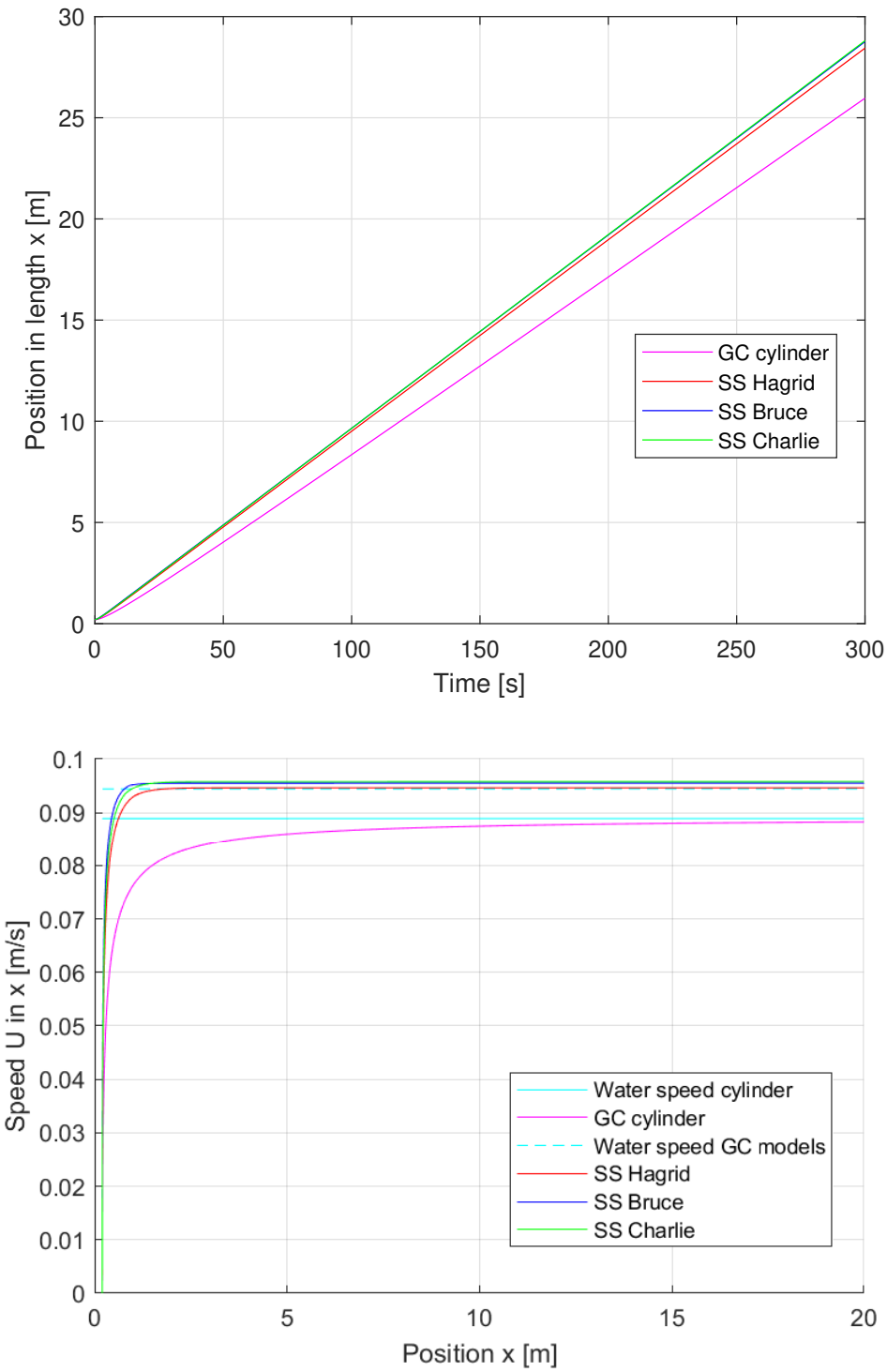

Figure 4.17: Simulation with Simplified Shapes discretisation (SS)

Once again, in Figure 4.17, water velocities are different because of the different height of the GC. However, it can be seen that body velocities are higher than the ones calculated for the water at their geometric centre height. This means that the most influential parts of the body for the motion are legs and arms. Indeed, the chest and head are higher than the limbs and in our flume, at these heights, water velocity is higher closer to the bottom. It is considered that the GC is about at the mid-thickness of the chest. That means that another point linked to the shape rules the motion in this kind of model and its position is linked to limbs and their length. This point is the thrust centre.

Bodies reach water velocity about 3 times faster than in the GCD. The explanation is that the global drag of the body is higher and the acceleration phase lasts for 1 or 2 m maximum.

Moreover, the differences between body shapes are more visible with the SSD. In this case of a SSD, Hagrid's velocity is about 1% smaller than the velocity of the thinner models while it is not the case with the GCD. The explanation is that Hagrid is wider and so his left arm and leg are closer to the wall, which means a lower water velocity. The result is that the sum of each drag is lower than the drag of a thinner body for this orientation.

Finally, body velocities are not so different from the velocities calculated with the GCD. However, a small difference in velocity (1% from the actual velocity in this case of error due to the kind of body discretisation) can lead to a huge difference in the positions when we calculate the motion for days. This small analysis demonstrates the utility of a good determination of the mass and thrust centre position. Indeed, a body for which the position results of a variation of its density (hypostasis with blood accumulating in the ends) has a centre of mass at a different position from its geometric and thrust centres. GC is used to calculate the rotation of the body and its position while thrust centre is used to estimate a water velocity at the level of the body. Our GC is the one of a body in a wheelchair because the position on a wheelchair is close to ours and precised data are available for this case (Wieczorek et al., 2021). However, this simple case of a 1D motion in a non-uniform flow shows the necessity of a precise estimation of the centre of mass, geometric centre and the centre of thrust for a dead body in our position.

4.4.2 Influence of the initial orientation of the body

The simulation is realised with a discharge of $Q = 30$ l/s, a downstream condition on height $h_{down} = 0.62$ m, spatial step $(dx; dy; dz) = (0.02; 0.025; \approx 0.0062)$, $t_{simulation} = 300$ s, a time step $dt = 0.015$ s and a cylinder placed at the following initial position:

$$\begin{aligned} x_{GC} &= 0.2\ m \\ y_{GC} &= 0.15\ m \\ z_{GC} &= z_{surface} - \frac{L}{4} \approx 0.565\ m \\ \theta &= \theta_0 \end{aligned} \tag{4.33}$$

The only difference with the tests of the previous section is that this time the initial orientation is different.

3 orientations are compared:

- $\theta_0 = 0^o$
- $\theta_0 = 45^o$
- $\theta_0 = 90^o$

The motion of three models are simulated: the cylinder, Hagrid and Charlie. The cylinder is used as a point of comparison. However it has been decided that only Hagrid and Charlie is studied because Charlie and Bruce have the same motion and Hagrid has a particularity due to his body shape.

The fact that Hagrid has one of his arms perfectly aligned to one of his legs when he is oriented at $\theta = 45^o$ is interesting to compare with a different body shape such as Charlie's. At $\theta = 45^o$, Charlie has none of his limbs aligned and his frontal area is higher than the one of Hagrid with a smaller drag coefficient C_D[3].

The two kinds of discretisation are compared this time again.

[3]See section 3.1.2.4 for the frontal areas.

The Motion and velocity of a cylinder are plotted in Figure 4.18:

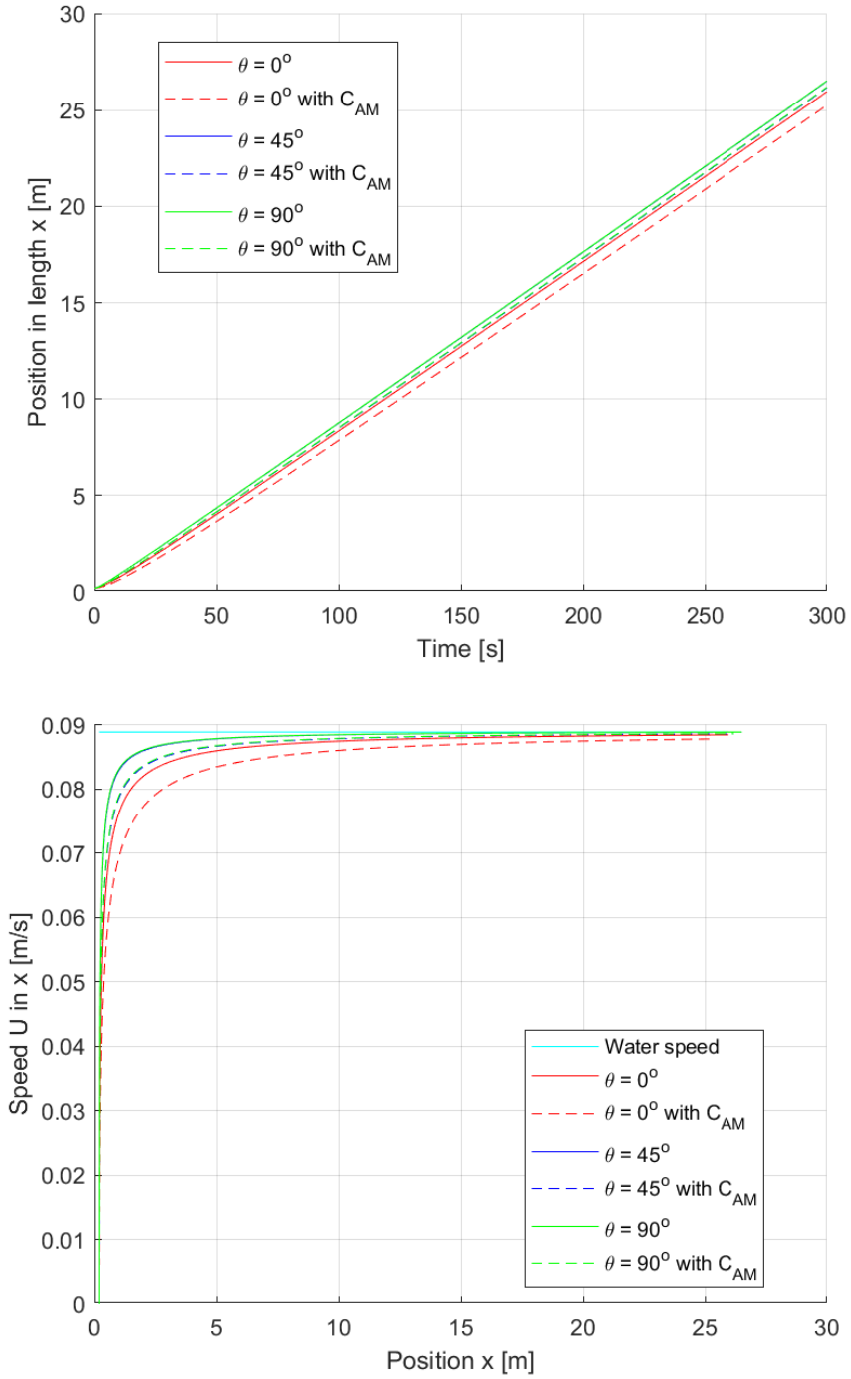

Figure 4.18: Position and velocity of the cylinder

The influence of the added mass is limited. Indeed, the case when the cylinder is aligned with the flow ($\theta = 0^o$) is the one where its influence is the highest. For the two other cases, drag is higher and so the acceleration phase is shorter and the influence of the added mass is reduced. In these cases, the added mass changes the final position of about 0.5 m. As its influence is ruled by the duration of the acceleration phase, this difference should remain constant for our velocity range.

Then, velocity and motion of the cylinder at 45° and 90° are almost the same. This is why the result is at 45° is not visible, it is hidden by the one at 90°. That is due to the fact that their areas are very similar. Indeed, since the models are exposed to the same water velocity and have the same drag coefficient, the difference can only come from the frontal areas. These areas are calculated with the general formula 4.34 with our cylinder of $D = 0.11$ m and $L = 0.24$ m.

$$A_{p,\theta} = \pi(\frac{D}{2})^2 * \cos\theta + L * D * \sin\theta \tag{4.34}$$

$$\begin{aligned} A_{p,0} &= \pi(\frac{0.11}{2})^2 * \cos 0 + 0.24 * 0.11 * \sin 0 = 0.0095\ m^2 \\ A_{p,45} &= \pi(\frac{0.11}{2})^2 * \cos 45 + 0.24 * 0.11 * \sin 45 = 0.0275\ m^2 \\ A_{p,90} &= \pi(\frac{0.11}{2})^2 * \cos 90 + 0.24 * 0.11 * \sin 90 = 0.0193\ m^2 \end{aligned} \tag{4.35}$$

Thanks to this simulation, a point of comparison is available for the simulations with a human shape.

GC discretisation and SS discretisation are compared for each angle and with the areas previously determined in section 3.1.2.4 for the areas of GCD (Figures 4.19 and 4.20). This time again for the models, body velocities are not displayed for a travelled distance beyond 20 m. Due to their importance in this study, frontal areas are reminded here (Figure 3.13 is still linked to this table):

Model\Orientation	0°	45°	90°	180°
Hagrid	76.01	113.65	144.93	76.01
Bruce	85.17	127.78	118.83	85.17
Charlie	82.29	117.45	109.5	82.29

Table 4.2: Frontal area of the models in cm^2

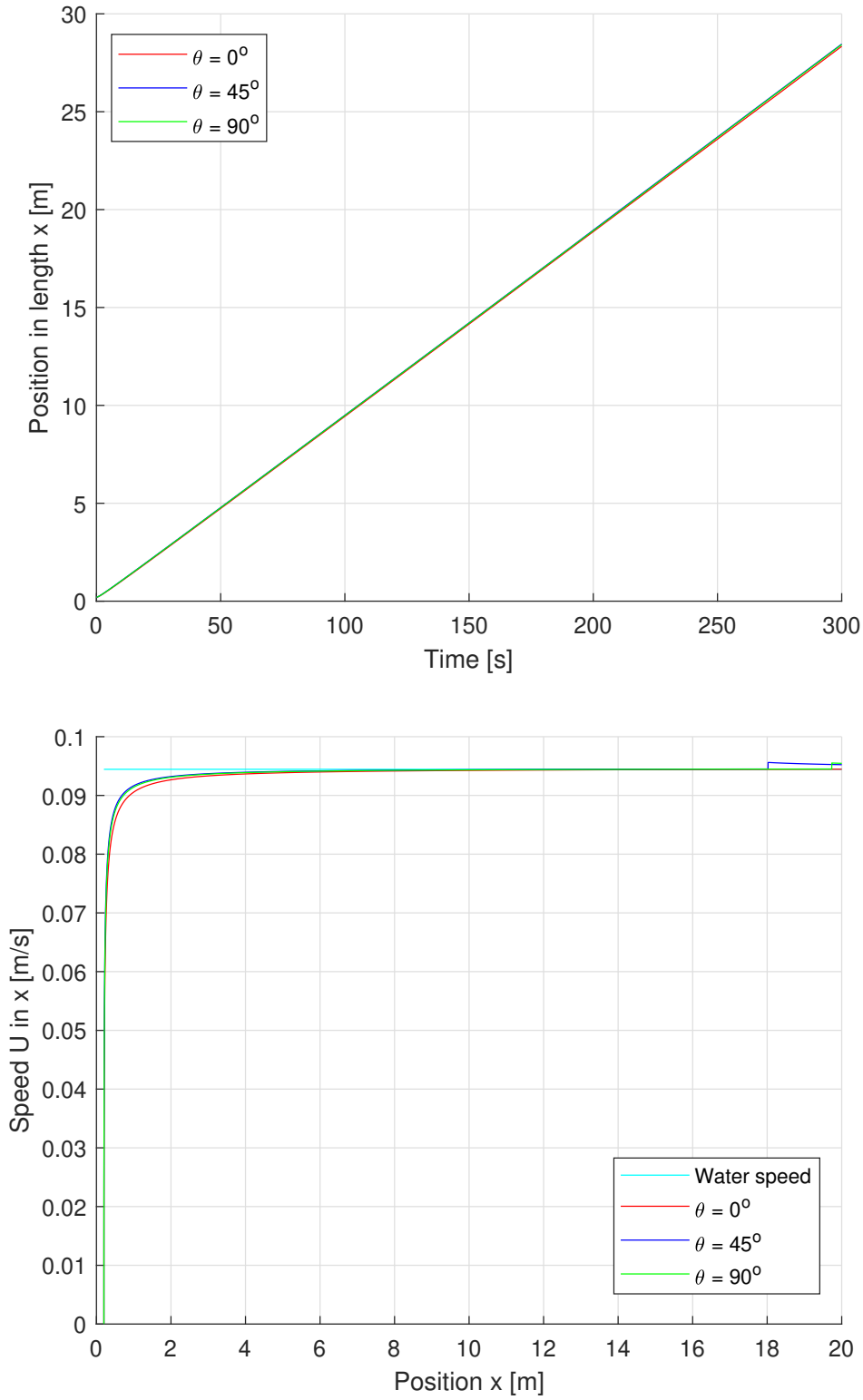

Figure 4.19: Simulation of Charlie with GCD

The jump in Charlie velocity at about $x = 18$ m is due to a numerical instability. Indeed at this distance, the difference between water and body velocity is around 10^{-5} m/s squared for the calculation of the acceleration. This leads to a step in the body velocity. Anyway, this step is of 10^{-3} m/s and we expect it to disappear in an unsteady flow. This numerical jump in the body velocity is also observed for the two other models but occurs at $x > 20$ m and is not shown in the studied figures.

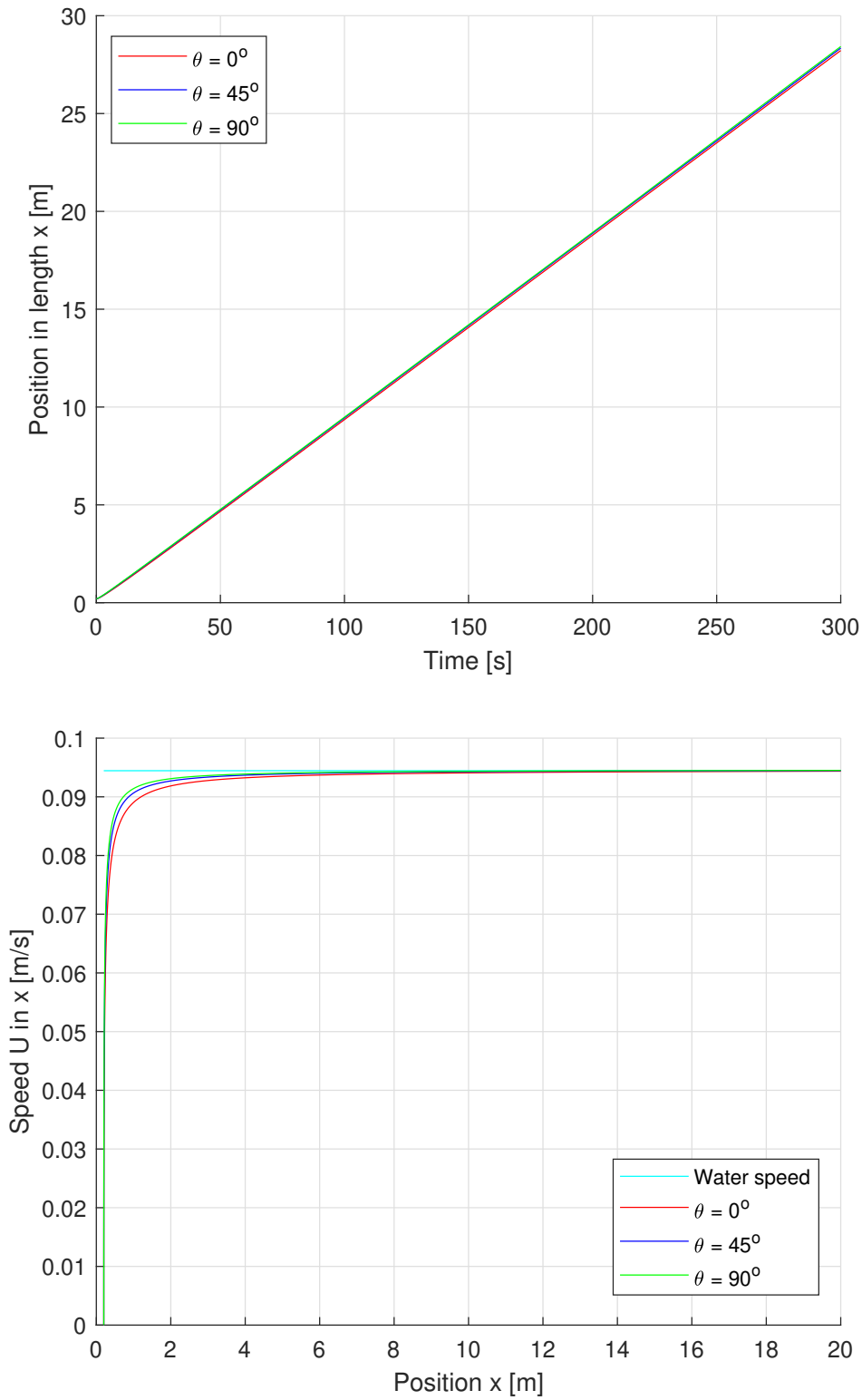

Figure 4.20: Simulation of Hagrid with GCD

These graphs can be compared to the SSD simulations. These simulations are computed with exactly the same conditions and water velocity is took at the geometric centre of the bodies (Figures 4.21 and 4.22).

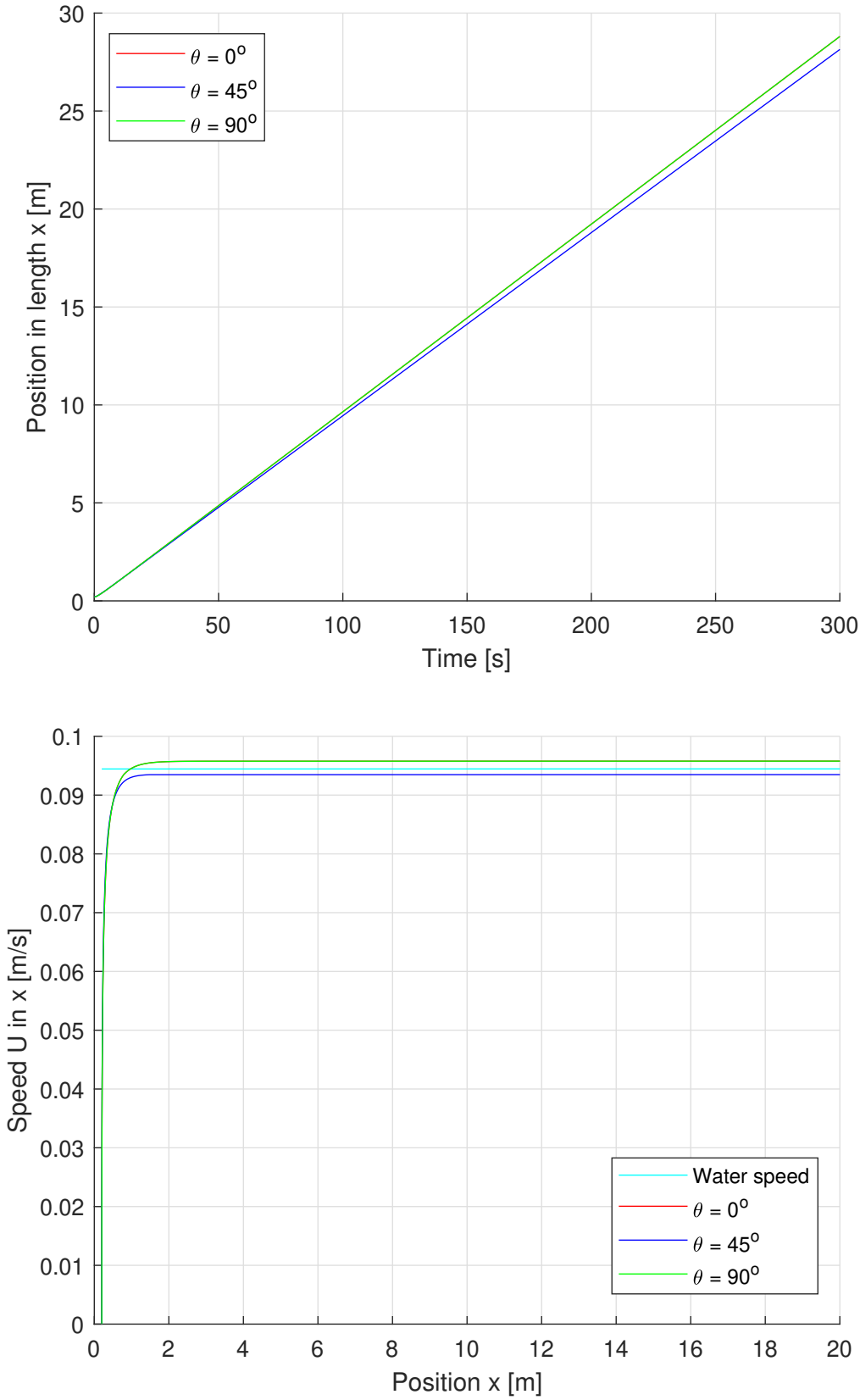

Figure 4.21: Simulation of Charlie with SSD

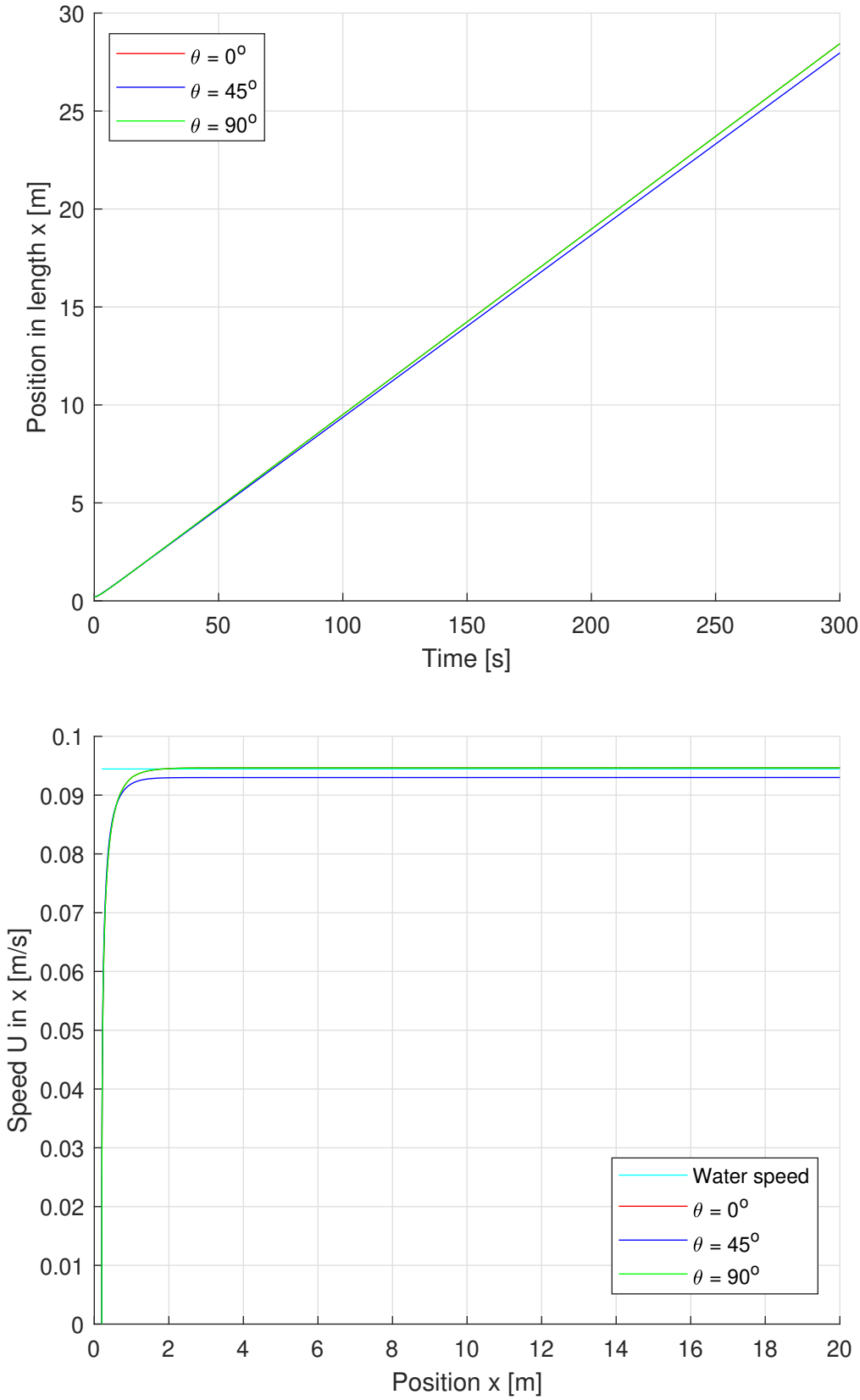

Figure 4.22: Simulation of Hagrid with SSD

Important to note is that each simulation starts with the same position for the geometric centre of the body.

In contrast to the GCD simulation, the acceleration phases are similar for each orientation but the final velocity is different. That means that with the SSD simulation, the areas are almost constant despite the different orientations but the thrust centre is on a different position.

The fact that the bodies move slower when oriented at $\theta = 45^o$ is very interesting. That clearly shows that the thrust centre is orientation dependant and is not a fixed point for the position like the geometric centre. Furthermore, with our kind of flow, it is known that water velocity increases when getting closer to the centre of the flume. So even if the body has a linear variation of its yaw rotation, this is not the case for the thrust centre. This is schematised in Figures 4.23, 4.24 and 4.25:

- Geometric centre
- Thrust centre

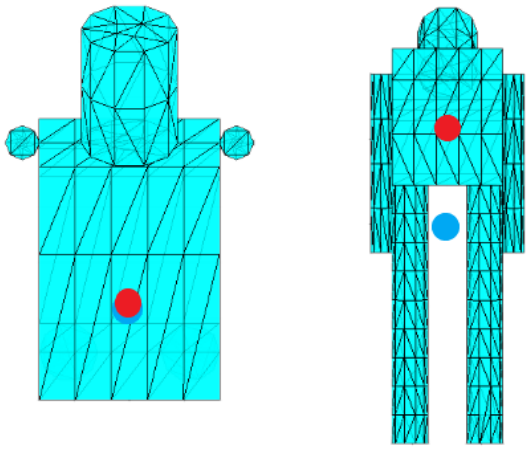

Figure 4.23: Scheme of the centres at an orientation of $\theta = 0^o$

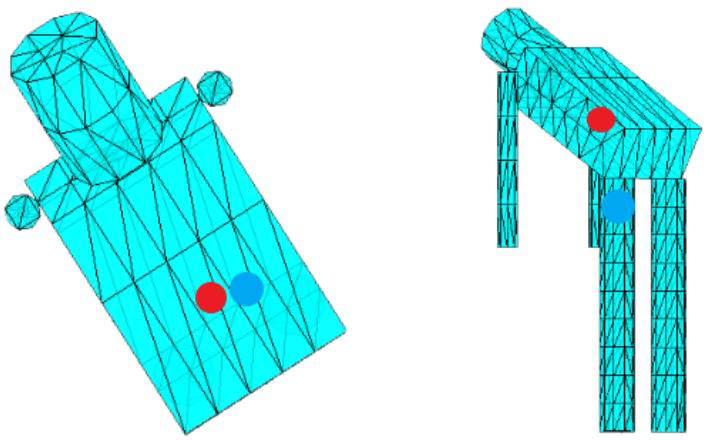

Figure 4.24: Scheme of the centres at an orientation of $\theta = 45^o$

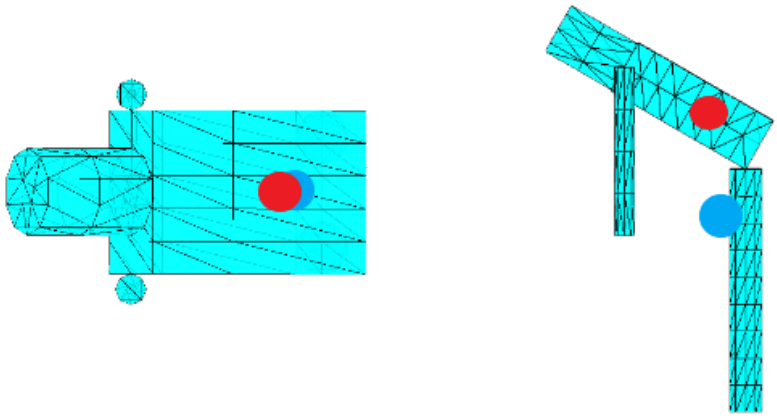

Figure 4.25: Scheme of the centres at an orientation of $\theta = 90^o$

These are only schemes of the centre's positions but they clearly show what has been explained in the previous paragraph. In the simulated conditions, the bodies' geometric centres are at $y_{GC} = 0.15$ m which means that water velocity gets higher when going on the right side of schemes 4.23, 4.24 and 4.25. Furthermore, they are above the maximum of the dip phenomenon and so water velocity gets higher when going down.

It must be kept in mind that the motion along *y* and the yaw rotation θ are blocked for these simulations. When they are released, it is expected to have a relation between geometric centre and thrust centre for the yaw rotation. That means that both points are very important to characterise the body.

Furthermore, the consideration of the motion along *y* may influence the position of the thrust centre. Indeed in the previous simulations, forces were one-dimensional forces. A second dimension would return a more complicate calculation and a more complete understanding of the thrust centre.

Finally, these experiments highlight the need for a specific drag coefficient for a human shape and its variables (body shape, clothes, hair, etc.). Even at high Re the behaviour of a human shape with the GCD or the SSD are different and reach a different velocity. As the final goal is to develop a model which predicts the position of a body in time (which can be of weeks), the need for an realistic estimation of the body velocity is obvious.

4.5 Conclusion

This chapter focus on the importance of the kind of discretisation used for the body models and the influence of the characterisation of the flow velocity on the one-dimensional motion of a body.

Discretisation of the flow and the models are linked and an inaccuracy on the characterisation of the flow or the discretisation of the model leads to a difference on the estimation of the position respectively of 1% or 150% of the actual drift.

The narrow flume is hard to modelize due to the dip phenomenon. This dip phenomenon evolves with water velocity but it is considered as constant. The influence of the flow discretisation is tested and a good knowledge of the flow is the most important factor to evaluate the drift of a body.

The kind of discretisation is important to evaluate the position of the body along y and the yaw rotation. The pointwise discretisation does not allow rotation while this motion rules the frontal area and the drift of the body. The thrust centre rules the displacement with the simplified shape discretisation but is difficult to evaluate.

5 | Outlook

It has previously been mentioned that this work is one of the first ones on the subject. In addition to that, the study was realised in a limited time (4 months). This means that there are many follow up opportunities. In this chapter, we try to have an overview of what needs to be done on the subject..

5.1 Improvements

5.1.1 Experimental modelling

In section 3.1.2.4, we mention that uncertainties on the determination of our projected areas are not negligible and that we did not try to estimate the Body Surface Area (BSA) of our models. A first step is to realise a numerical model of our body models in the fixed position. Indeed, a numerical model allows a very good estimation of both projected areas and BSA (Bixler et al., 2007). Furthermore such a model (Figure 5.1) would be very useful to differentiate pressure drag and skin friction. This model could finally be used to compare the simplification in simple shapes with the actual body.

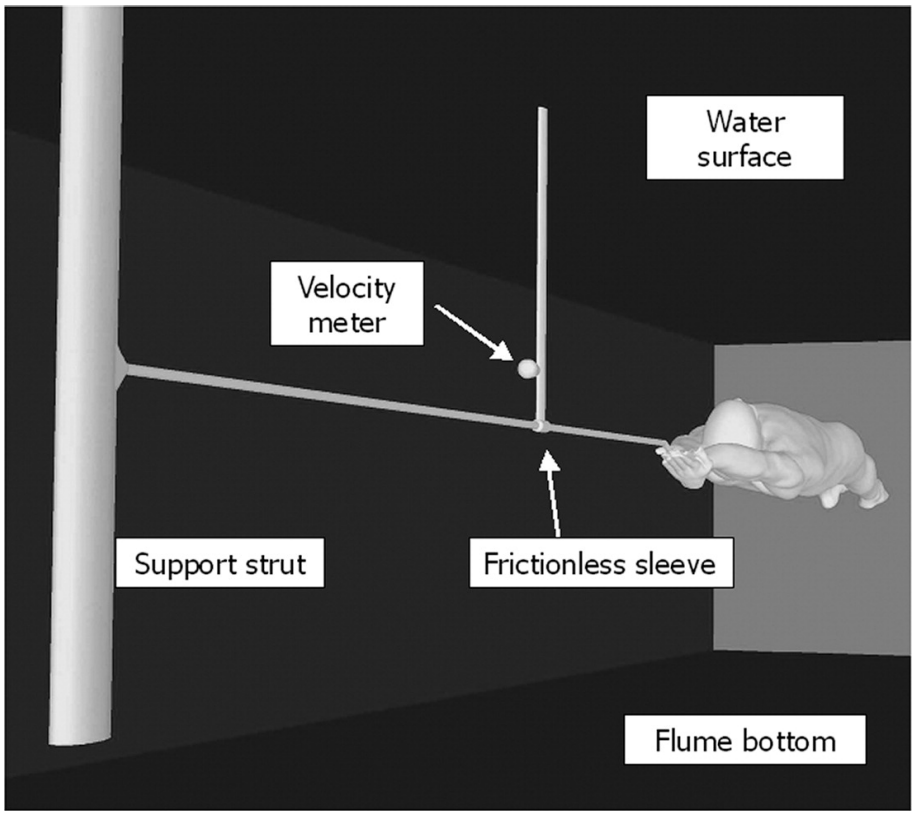

Figure 5.1: CFD model of the experiments (Bixler et al., 2007)

Then a relation could be established between the BSA and the projected areas. This lean on of the works of Nucara et al. (2012), Tanabe et al. (2000) and Tikuisis et al. (2001) for estimating the BSA in function of the mass and size of people. This relation would permit to deduce complex data like $A_p(\theta)$ from basic knowledge about a drowning victim.

The differentiation which is mentioned between pressure drag and skin friction is really important for the case of a human body. Indeed, experiments have been realised with optimised swimsuits to show that their skin friction was lower thanks to the swimsuits and improved the performances of the swimmer (Bixler et al., 2007). The same study should be done in our case with common clothes to analyse their influence. Furthermore, it has already been observed that the pressure drag could change with the orientation of the body and the way it was dressed. In our study in the laboratory flume, it has been decided to not compare the cases of a dressed model and a naked one. Indeed, the clothes of the smaller body models were not composed of the same material as a common clothes and it was not possible to differentiate pressure drag from skin friction. A first way to differentiate skin friction from pressure drag would be to work like Ghaffarian et al. (2020). They worked with two models: one in the studied material and the other in paraffin, a very low friction material. The paraffin shape gives mainly the pressure drag while the other one is a combination with skin friction. Proceeding like this, both the pressure drag and the skin friction can be known separately.

Another issue with the measurement system is that we had to work with a lever arm and many components between the model and the strain gauge. Forces may have been distorted due to all connections between the components. Experiments could be repeated with a smaller strain gauge and no lever arm in order to directly measure the force without any distortion.

At last, measurements have been taken in a narrow channel with a complex flow (Figure 5.2). A way to improve the precision of the deduced drag coefficient C_D is to work in a wider channel (Figure 5.3). This kind of channel would not be subject to a DIP phenomenon and the water velocity would be close to the average one. This change of channel width coupled to a precise determination of the water density would give a more reliable relation between the measured force and the drag coefficients.

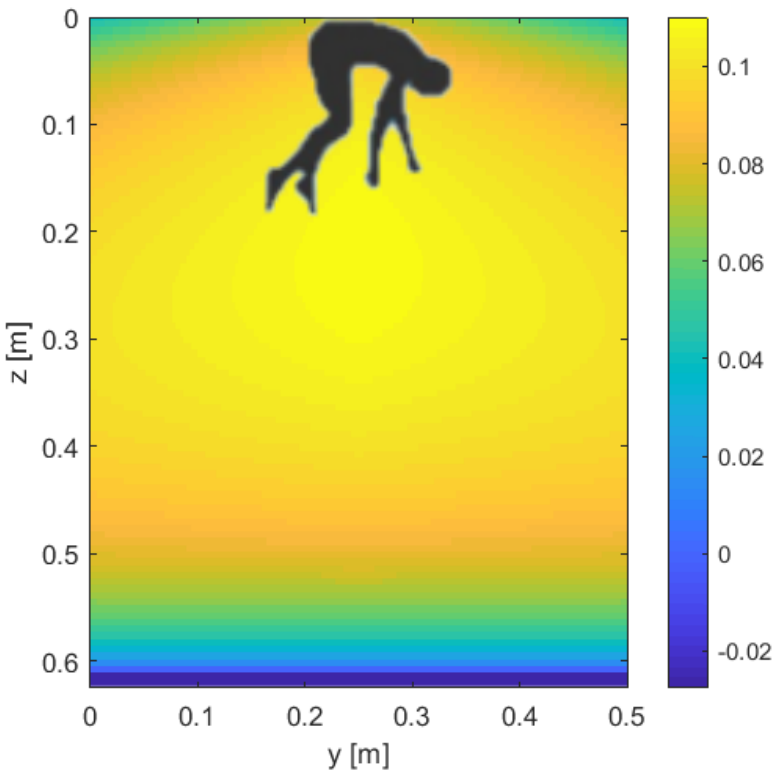

Figure 5.2: Scheme of the velocity profile in our experiments

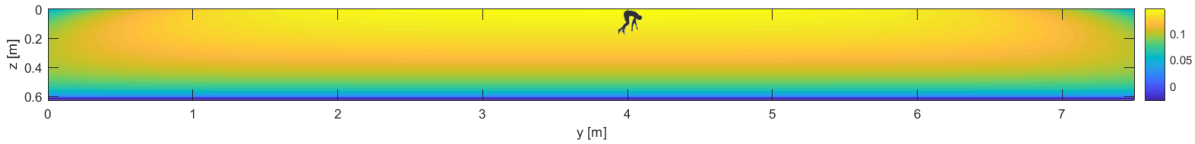

Figure 5.3: Scheme of the velocity profile in a wider channel

The following relation between F and U is used with a single value of U. With a flow closer to a uniform one, this approximation would be of better quality.

$$F = \frac{1}{2}\rho_w A C_D U^2 \tag{5.1}$$

After that, the drag component of the different bodies are compared at different Re and with only two different depth. It may be useful to repeat the experiments but this time keeping a fixed Re and vary depth more than twice to compare its influence. It is already known that the body's vertical motion is influenced by biological parameters. It seems obvious to check if this variation of depth has an influence on the interaction between the flow and the body. The same study has already been realised by Chu et al. (2018) and they showed the importance of considering depth in this interaction (Figure 5.4). The same observation is done with our models but the study of this position has not been developed enough in this work.

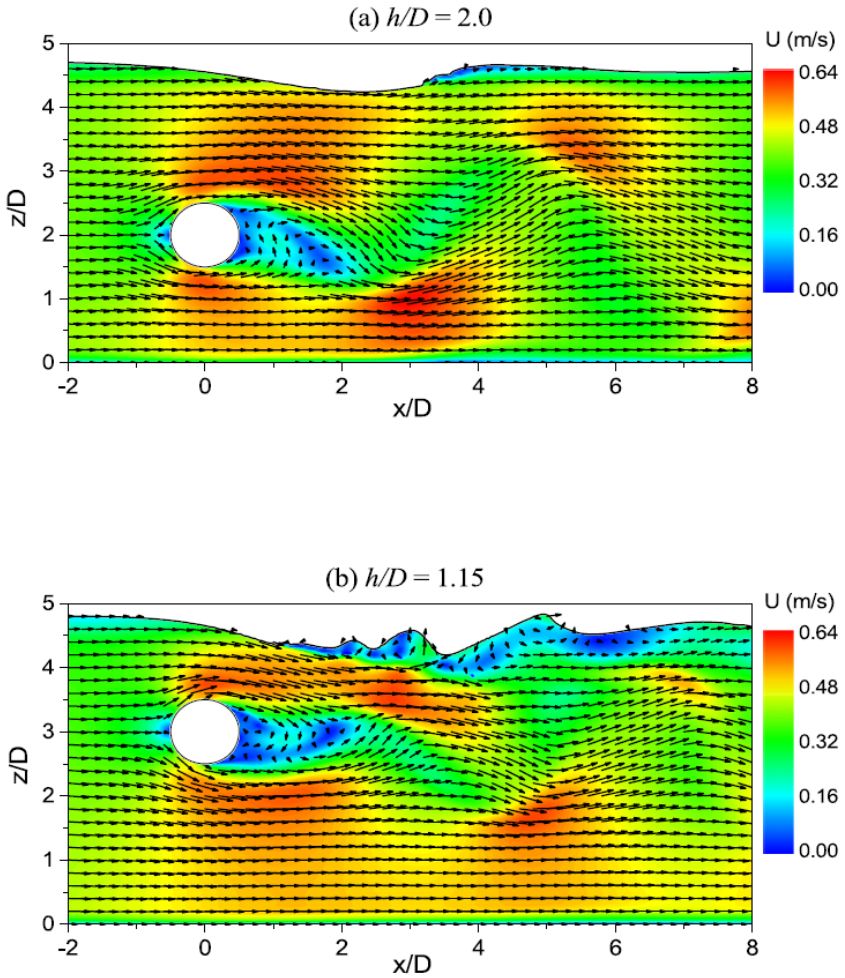

Figure 5.4: Influence of depth (Chu et al., 2018)

Finally, the study of the other coefficients of interaction between the body an the fluid such as C_{AM}, C_S and C_L has to be realised. In parallel, experiments to determine the gravity and thrust centre of a dead body in the studied position may be really useful. This determination would allow to use the precise velocity at the gravity centre in the simulation when the force balance is done.

5.1.2 Numerical modelling

So far, the toy model presented in Chapter 4 is restricted to predicting the acceleration of the body under fluid forces in a one-dimensional setting. Moving towards more realistic modelling requires the simulation of the body drift based on two-dimensional velocity fields in real-world domains, coupled with a parametrisation of the vertical profile of velocity. The governing equations need to be generalised accordingly (Ghaffarian et al., 2020; Persi et al., 2016, 2019).

Considering such equations, the models could be discretised in a better way to take into account forces applied by the flow on the whole body. The models are discretised as described in sections 5.1.2.1 and 5.1.2.2.

5.1.2.1 Cylinder

Each numerical model of motion is first tested with a cylinder to have a point of comparison. A fully discretised cylinder is created to be able to study this shape (Figure 5.5). It is composed of similar meshes as the models.

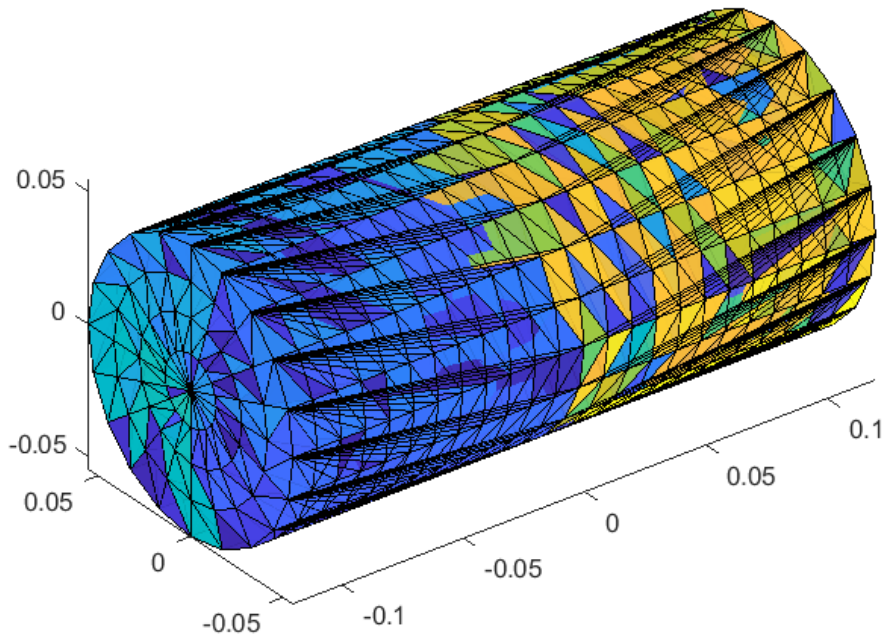

Figure 5.5: Fully discretised cylinder

5.1.2.2 Body models

The discretisation of the models consists in the generation of a mesh composed of 1240 triangles surrounding the simplified model (Figures 5.6 and 5.7). This value and the number of nodes by shape has been optimized to have more pannels in the zone of interest and enough precision in the other zones. The discretisation is realised with the shapes described in the previous section but this time totally considered to calculate forces on the whole body instead of the ones on representative points.

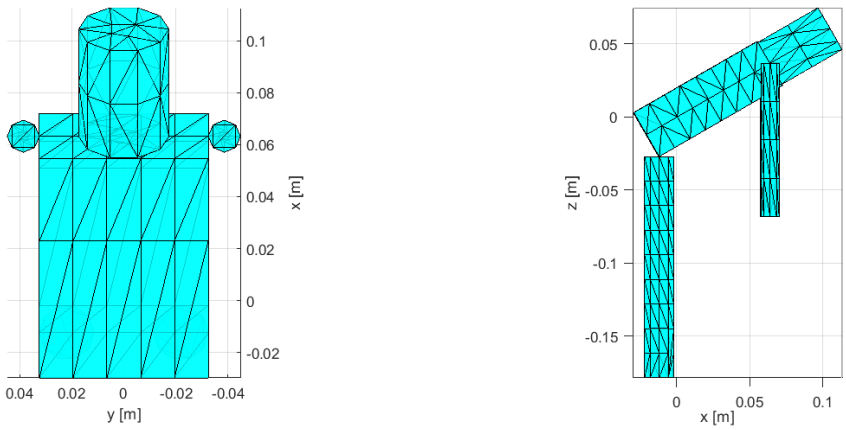

Figure 5.6: Discretisation of a whole simplified model

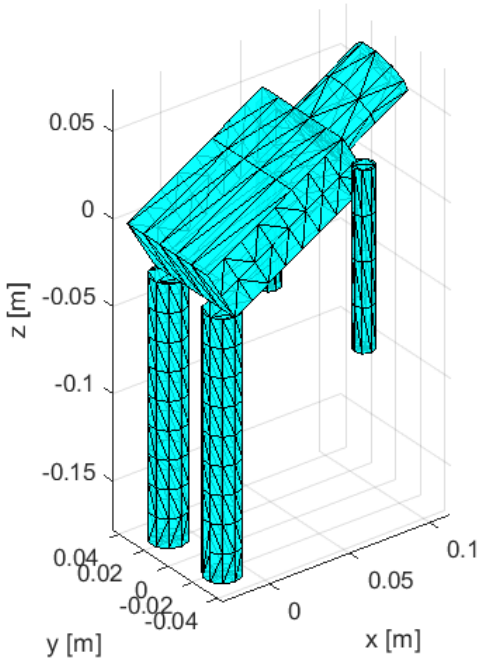

Figure 5.7: Discretisation of a whole simplified model

The goal of this discretisation is to apply the hydraulic load directly on each mesh of the body and then deduce the motion induced by the sum of all the forces $\overrightarrow{F}_p$. A force would be applied perpendicularly or in parallel to each mesh and multiplied by the area of the mesh to deduce an applied force at the centre of this one.

These directions and points can be easily found knowing that coordinates of the centre $\overrightarrow{P}$ of a mesh is the average of the coordinates defining the mesh. While the directions $\overrightarrow{d}_{\parallel}$ is the one defined by the mesh and its points and $\overrightarrow{d}_{\perp}$ is only the normalised perpendicular to the plane defined by the points and passing through the centre previously calculated.

$$P(x,y,z) = (\frac{x_1+x_2+x_3}{3}, \frac{y_1+y_2+y_3}{3}, \frac{z_1+z_2+z_3}{3}) \tag{5.2}$$

Considering that $\overrightarrow{I_1}$, $\overrightarrow{I_2}$ and $\overrightarrow{I_3}$ are the vectors from the origin of the axis to the three points defining a mesh in the 3D space, we have:

$$\begin{aligned} \overrightarrow{V}_{12} &= \overrightarrow{I_2} - \overrightarrow{I_1} \\ \overrightarrow{V}_{23} &= \overrightarrow{I_3} - \overrightarrow{I_2} \\ \overrightarrow{V}_{31} &= \overrightarrow{I_1} - \overrightarrow{I_3} \end{aligned} \tag{5.3}$$

$$\overrightarrow{d}_{\perp} = \frac{\overrightarrow{V}_{12} \wedge \overrightarrow{V}_{23}}{|\overrightarrow{V}_{12} \wedge \overrightarrow{V}_{23}|} \tag{5.4}$$

Finally, the area A_{mesh} of each mesh is calculated thanks to Heron's formula:

$$\begin{aligned} s &= \frac{|\overrightarrow{V}_{12}| + |\overrightarrow{V}_{23}| + |\overrightarrow{V}_{31}|}{2} \\ A_{mesh} &= \sqrt{s(s-|\overrightarrow{V}_{12}|)(s-|\overrightarrow{V}_{23}|)(s-|\overrightarrow{V}_{31}|)} \end{aligned} \tag{5.5}$$

The advantages of this representation are that the actual forces are computed on a shape close to the real one, no projected area of the body is needed to work, and the interaction between each shape of the body may be considered. However, the flow around the body has to be completely characterised which is complicated. Also, the calculation time depends on the number of mesh which is of course much higher than the previous discretisations.

Following result is obtained when showing each perpendicular direction (Figure 5.8). It has to be mentioned that the directions of the arrows had to be inverted for the scheme but actually they are pointing in the direction of the body.

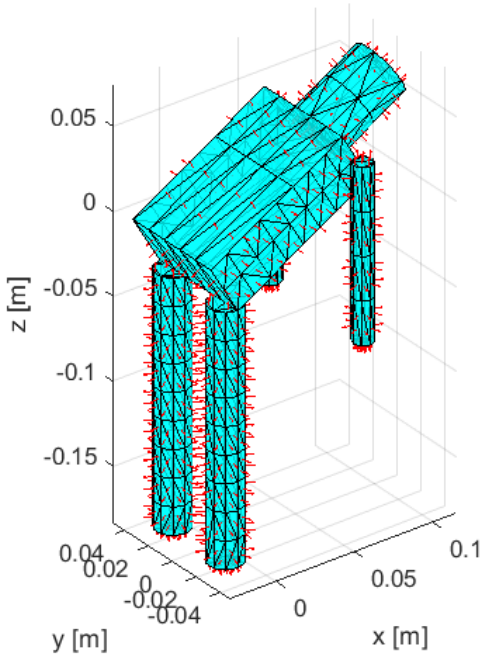

Figure 5.8: Each direction and point of application of perpendicular forces on the discretised model

5.1.2.3 Existing CAD models

Models discretised as a combination of simplified shapes could be compared to existing cost free CAD models found in Malcevic (2020).

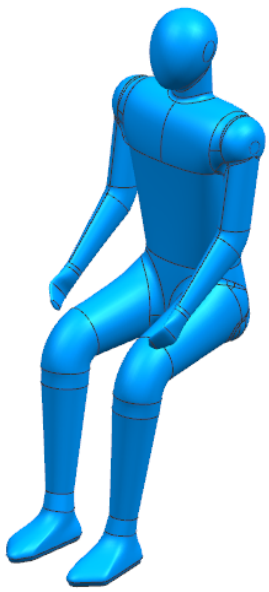

Figure 5.9: Example of a CAD model (Malcevic, 2020)

5.2 Collaborative work

Based on laboratory experiments and on a toy model, the present master thesis has brought contributions on which subsequent more advanced and realistic modelling of body drift will build. The present study frames indeed within a broader initiative, involving other actors such as INSA Lyon.

Here, the focus was set mostly on the horizontal motion of the body, but little attention was paid to the vertical motion. Progresses in this direction will obviously require parametrization of biological processes, which is a challenging, multidisciplinary task. Among other aspects, it requires a characterization of the volume evolution of the rib cage as a function of water temperature, immersion time, body shape, gender, flow variables, etc. In this process, various sources of data will prove valuable, including statistics available in literature (Heaton et al., 2010; Mateus and Vieira, 2014; Matheus et al., 2013) or on-going experiments conducted in Lyon by Celia Maghakian in collaboration with the fire brigade (analysis of the vertical motion of a body falling in water, and drift experiments in real-world rivers). Similar contacts have been initiated with the sub-aquatic brigade of the firefighters of the city of Liege. Such collaborations will be instrumental in subsequent steps of the research, by facilitating access to field data, and enabling us to capitalize on the experience of operational stakeholders. In particular, the sub-aquatic brigade owns body models, usually used for training, which could be used to simulate the drift of a human body in real-world flow conditions, generating valuable data for comparison with numerical predictions.

6 | Conclusion

This work is a first contribution towards mechanistic modelling of body drift for guiding the search for victims of drowning in rivers. The focus was set on determining possible ranges of values of the drag coefficient, which is instrumental for the parametrisation of drift models. The drag coefficient depends on a sizeable number of parameters, such as the body shape and positioning, presence of hair or clothes, the relative velocity with respect to the flow (through the particulate Reynolds number Re_p) and the submersion depth.

We conducted experiments in two complementary facilities, with two types of body models (dummies): 1:6 scale models in a 20-m long laboratory flume with recirculated water, and a prototype scale body model moved by a carriage at a controlled velocity in a 100-m long towing tank. In the former, three distinct body models were considered for evaluating the influence of the body shape. Two different plausible body positions were investigated, the influence of clothes was assessed, and the following parameters were varied systematically: relative velocity and body orientation (yaw angle).

Our experiments have shown the following:

1. In the laboratory flume (Re_p varying between $2.8{*}10^4$ and $5.2{*}10^4$), the drag coefficients of the body models range between 1.45 and 1.65 when the model is positioned at mid-depth, and between 1.7 and 2 when it is positioned close to the free surface. This is about 30% to 40% higher than the drag coefficient of a cylindrical object for a similar particulate Reynolds number.

2. The body model with a larger frontal area leads to considerably higher measured forces; but the drag coefficient does not differ by more than 15%.

3. The measured forces and the drag coefficient of the body models are found about 20% to 30% higher near the free surface than at larger submersion depths (e.g., at mid-depth). Moreover, when the submersion depth is larger, the measurements show less scatter than when the body model is positioned close to the surface, since in the latter case the flow around the body interacts strongly with the free surface.

4. Measured forces correlate better with the cross-sectional average of the flow velocity than with local velocity estimated from the ADVP.

5. In the towing tank (Re_p between 10^5 and $8 * 10^5$), for the case of a naked body model, the drag coefficient was observed to remain the same when the orientation is reversed. In contrast, with clothes, the drag coefficient increases by only 20% in one flow direction (head towards upstream), while it rises by up to 70% in the reverse direction (head towards downstream). This is explained by water entering the sweater in the latter case, inducing a “parachute effect". This effect becomes even stronger when the body model wears only the sweater than when it also wears pants. These findings were confirmed by additional tests performed in the laboratory flume, which highlight a substantial influence of the limbs position and the clothes.

Although it is obviously impossible to assign a clear-cut value for the drag coefficient of a human body, a key merit of the research conducted here is the identification of plausible ranges of values for this coefficient. This information is of high practical relevance for conducting uncertainty quantification on the predictions of a future drift model of victims of drowning in rivers.

The conducted experiments could benefit from a number of improvements, such as performing additional parametric tests (Bixler et al., 2007; Chu et al., 2018) to reach a better appraisal of the effects of clothes and body positioning (e.g., at full scale in the towing tank). Performing tests with a spherical or a cylindrical object in the towing tank would lead to a validation of the experimental procedure in the towing tank, similar to that achieved for the hydraulic flume. Image processing for the estimation of frontal areas should be refined, especially for the prototype scale body model. The Direct Linear Transformation method would certainly prove useful, as well as the generation of a 3D CAD model of the body.

Based on a literature survey, existing drift models, initially developed for computing the pathway of logs in rivers (Ghaffarian et al., 2020; Persi et al., 2016), are identified as a promising basis to set up drift models adapted to the case of victims of drowning in rivers. A simple, exploratory modelling was undertaken, in which the streamwise motion of a body was predicted based on the range of drag coefficients identified from the experiments. Further developments are obviously required to extend the modelling to 2D and take full benefit of the remarkable data sets available in practice (detailed bathymetric surveys, flow velocity fields obtained from computational fluid dynamics, real-time monitoring of river discharge and, monitoring of the operation of hydraulic structures and water temperature . . .). Ultimately, application to real-world case studies in urban rivers, such as the Meuse and the Ourthe in Liege, is sought.

Overall, the research field of interest here is far from mature, and many scientific challenges remain, particularly as regards bridging gaps between current mechanistic modelling capacity and the vast empirical knowledge existing in forensic medicine. Particularly, deeper analyses of the knowledge of body recovery in coastal and marine areas, including in relation with capsized boats used by asylum seekers, would enable building on the knowledge gained from the unprecedented number of such accidents having occurred over the last decade. More intense interdisciplinary collaborations with groups of forensic medicine would lead to evidence-based assumptions on the body positioning as well as a robust parametrisation of the decomposition effects controlling the vertical motion of the body.

Bibliography

Bern, 3007, L. S. (2021). Poumons et voies respiratoires - ligue pulmonaire suisse.

Bilterijs, M., Fobe, G., and Mergen, S. (2019). 77 noyades en Belgique en 2016: "Des générations entières d'enfants ne savent pas nager". Section: Info.

Bixler, B., Pease, D., and Fairhurst, F. (2007). The accuracy of computational fluid dynamics analysis of the passive drag of a male swimmer.

Boxho, P. (2013). *Eléments de Médecine légale*.

Braudrick, C. A. and Grant, G. E. (2000). When do logs move in rivers? 36(2):571–583.

Carniel, S., Umgiesser, G., Sclavo, M., Kantha, L. H., and Monti, S. (2002). Tracking the drift of a human body in the coastal ocean using numerical prediction models of the oceanic, atmospheric and wave conditions. 42(3):143–151.

Chu, C.-R., Lin, Y.-A., Wu, T.-R., and Wang, C.-Y. (2018). Hydrodynamic force of a circular cylinder close to the water surface. 171:154–165.

Cool Huy (2021). Cool Huy – Bienvenue sur le site "Eau Froide – Eau Libre de Huy".

Dey, S. (2014). *Fluvial Hydrodynamics*. GeoPlanet: Earth and Planetary Sciences. Springer Berlin Heidelberg.

Donoghue, E. R. and Minnigerode, S. C. (1977). Human body buoyancy: a study of 98 men. *Journal of Forensic Sciences*, 22(3):573–579.

Duma, D. (2010). *ADVP – Acoustic Doppler Velocity Profiler – Nortek Vectrino II - Quick guide*.

Ghaffarian, H., Lopez, D., Mignot, E., Piegay, H., and Riviere, N. (2020). Dynamics of floating objects at high particulate reynolds numbers. 5(5):054307.

Heaton, V., Lagden, A., Moffatt, C., and Simmons, T. (2010). Predicting the postmortem submersion interval for human remains recovered from u.k. waterways*. 55(2):302–307.

Heymsfield, S. B., Gallagher, D., Mayer, L., Beetsch, J., and Pietrobelli, A. (2007). Scaling of human body composition to stature: new insights into body mass index. 86(1):82–91.

Hora, M., Soumar, L., Pontzer, H., and Sládek, V. (2017). Body size and lower limb posture during walking in humans. 12(2):e0172112.

Humphreys, M. K., Panacek, E., Green, W., and Albers, E. (2013). Comparison of Protocols for Measuring and Calculating Postmortem Submersion Intervals for Human Analogs in Fresh Water. *Journal of Forensic Sciences*, 58(2).

Hölzer, A. and Sommerfeld, M. (2008). New simple correlation formula for the drag coefficient of non-spherical particles. 184(3):361–365.

Katopodes, N. D. (2019). Chapter 5 - Viscous Fluid Flow. In Katopodes, N. D., editor, *Free-Surface Flow*, pages 324–426. Butterworth-Heinemann.

Madea, B. and Doberentz, E. (2010). Commentary on: Heaton v, lagden a, moffatt c, simmons t. predicting the postmortem submersion interval for human remains recovered from u.k. waterways. j forensic sci 2010;55(2):3027. 55(6):1666–1667.

Malcevic, Y. (2020). human body - Recent models | 3D CAD Model Collection | GrabCAD Community Library.

Mateus, M. and Vieira, V. (2014). Study on the postmortem submersion interval and accumulated degree days for a multiple drowning accident. 238:e15–e19.

Matheus, M., de Pablo H., and Vaz, N. (2013). An investigation on body displacement after two drowning accidents. 229(1):e6–e12.

Megyesi, M., Nawrocki, S., and Haskell, N. (2005). Using accumulated degree-days to estimate the postmortem interval from decomposed human remains. 50(3):618–626.

Muhammad Saqlain, S., Ghani, A., Khan, I., Ghayyur, S. A. K., Shamshirband, S., Nabipour, N., and Shokri, M. (2020). Image analysis using human body geometry and size proportion science for action classification. 10(16):5453.

Nucara, A., Pietrafesa, M., Rizzo, G., and Scaccianoce, G. (2012). An anthropometric analysis of seated and standing people. In *Handbook of Anthropometry: Physical Measures of Human Form in Health and Disease*, pages 91–114.

Palazzo, C., Pelletti, G., Fais, P., Boscolo-Berto, R., Fersini, F., Gaudio, R. M., and Pelotti, S. (2020). Postmortem submersion interval in human bodies recovered from fresh water in an area of mediterranean climate. application and comparison of preexisting models. 306:110051.

Persi, E., Petaccia, G., and Sibilla, S. (2016). Large wood transport modelling by a coupled eulerianlagrangian approach | SpringerLink.

Persi, E., Petaccia, G., Sibilla, S., Brufau, P., and García-Navarro, P. (2019). Calibration of a dynamic eulerian-lagrangian model for the computation of wood cylinders transport in shallow water flow. *Journal of Hydroinformatics*, 21(1):164–179. Copyright - Copyright IWA Publishing Jan 2019; Dernière mise à jour - 2020-09-11.

Reh, H. (1967). Anhaltspunkte für die Bestimmung der Wasserzeit. *Deutsche Zeitschrift fur die Gesamte Gerichtliche Medizin*, 59(2-3):235–245.

Santé publique France (2019). Noyade.

Simmons, T., Adlam, R. E., and Moffatt, C. (2010). Debugging decomposition datacomparative taphonomic studies and the influence of insects and carcass size on decomposition rate. 55(1):8–13.

Tanabe, S.-i., Narita, C., Ozeki, Y., and Konishi, M. (2000). Effective radiation area of human body calculated by a numerical simulation. 32(2):205–215.

Tikuisis, P., Meunier, P., and Jubenville, C. (2001). Human body surface area: Measurement and prediction using three dimensional body scans. 85:264–71.

Van Daalen, M. A., Kat, D. S. d., Grotebevelsborg, B. F. L. O., Leeuwe, R. d., Warnaar, J., Oostra, R. J., and Duijst8208;Heesters, W. L. J. M. (2017). An aquatic decomposition scoring method to potentially predict the postmortem submersion interval of bodies recovered from the north sea. 62(2):369–373.

Wieczorek, B., Kukla, M., and Wargu (2021). The symmetric nature of the position distribution of the human body center of gravity during propelling manual wheelchairs with innovative propulsion systems. 13(1):154.

Wikipédia (2021). Yaw (rotation).

World Health Organization (2014). Global report on drowning: preventing a leading killer.

Yang, H., Fan, M., Liu, A., and Dong, L. (2015). General formulas for drag coefficient and settling velocity of sphere based on theoretical law. 25(2):219–223.

Yang, S.-Q., Tan, S.-K., and Lim, S.-Y. (2004). Velocity distribution and dip-phenomenon in smooth uniform open channel flows. 130(12):1179–1186.

A | Appendix

.1 First measuring system, variable, surface

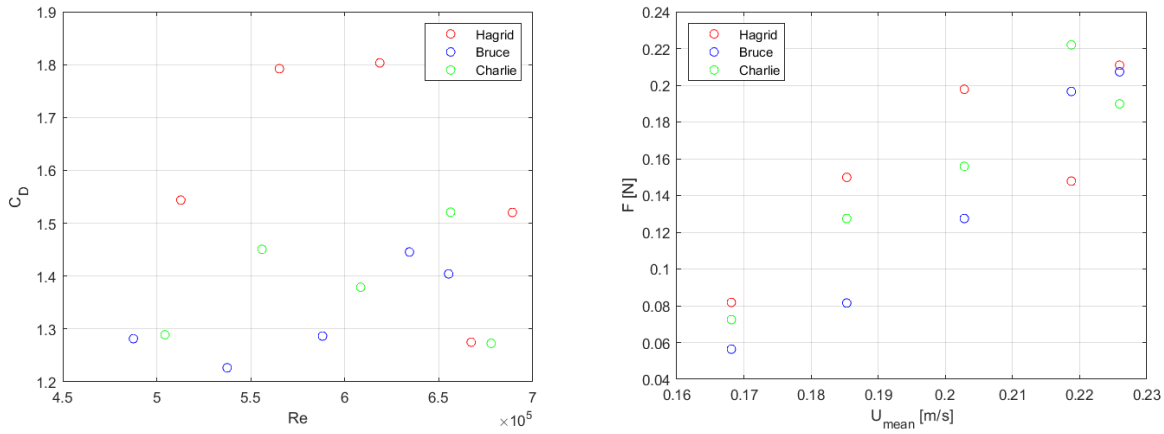

Figure 1: Variable, $\theta = 0^o$

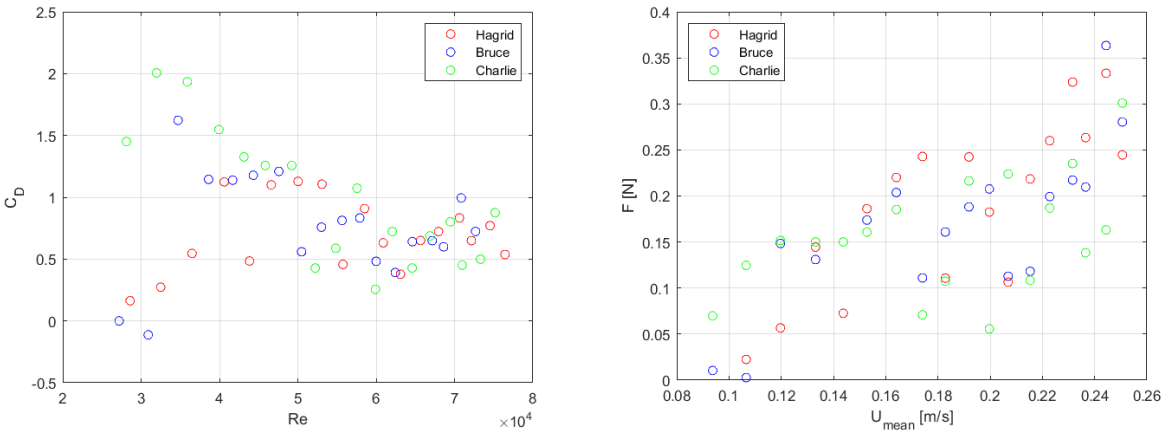

Figure 2: Variable, $\theta = 90^o$

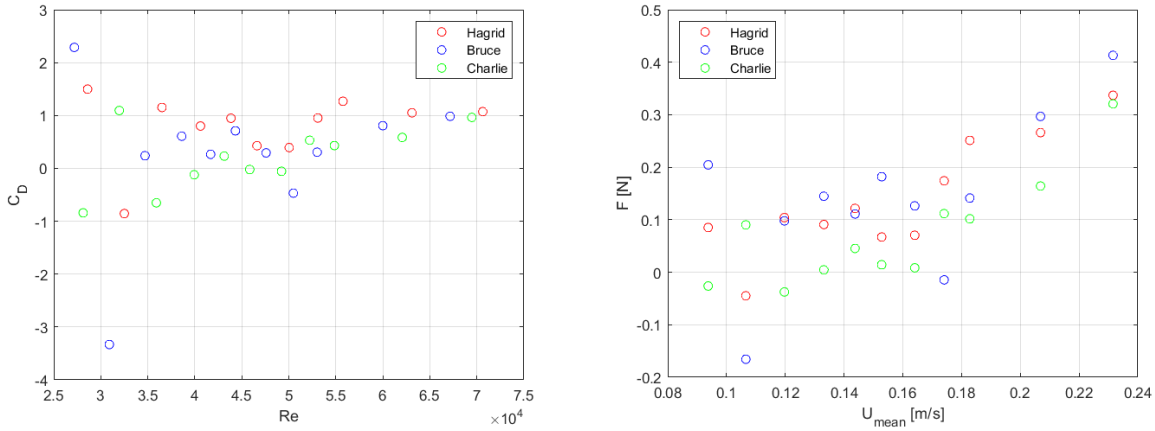

Figure 3: Variable, $\theta = 135^o$

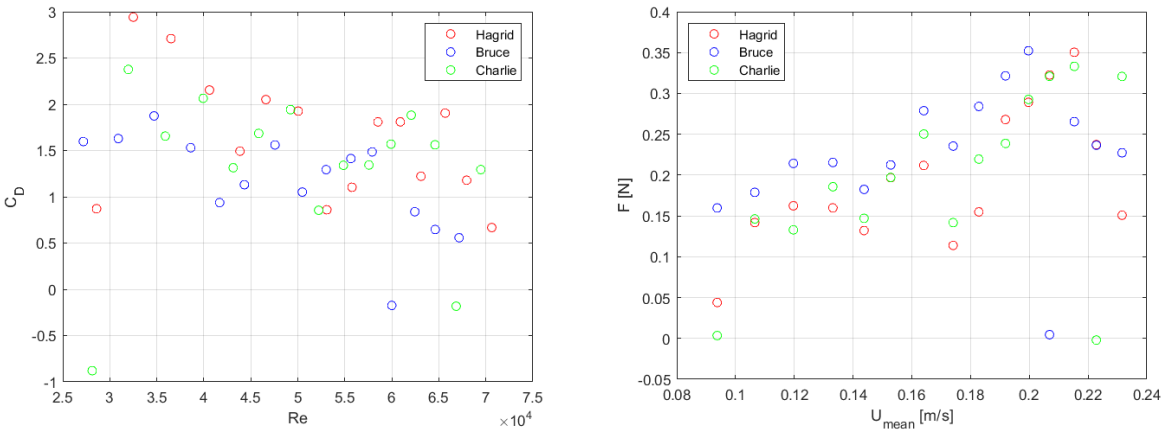

Figure 4: Variable, $\theta = 180^o$

.2 First measuring system, stable, surface

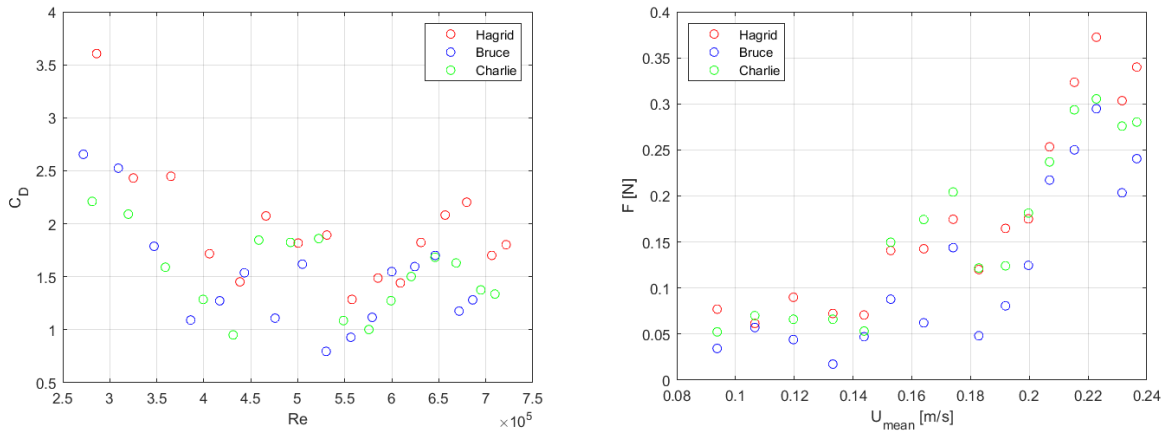

Figure 5: Stable, $\theta = 0^o$

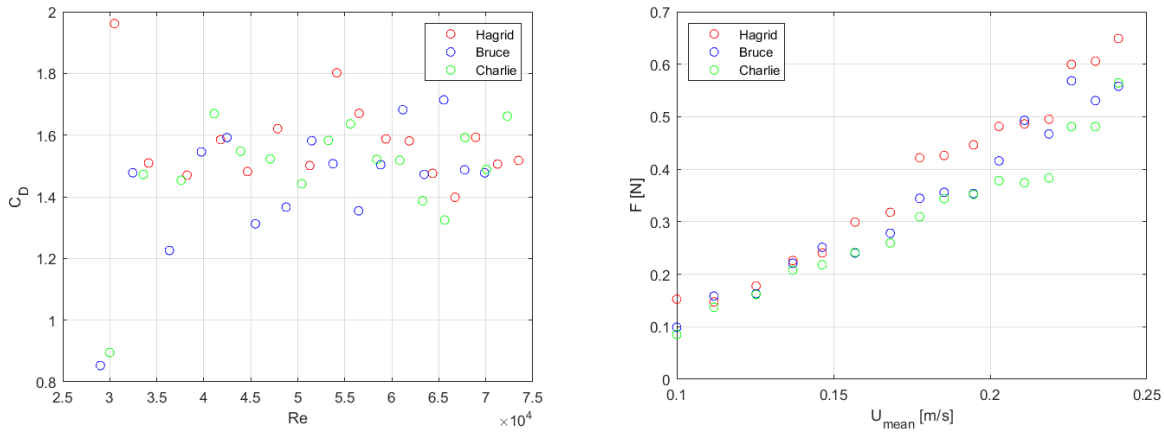

Figure 6: Stable, $\theta = 90^o$

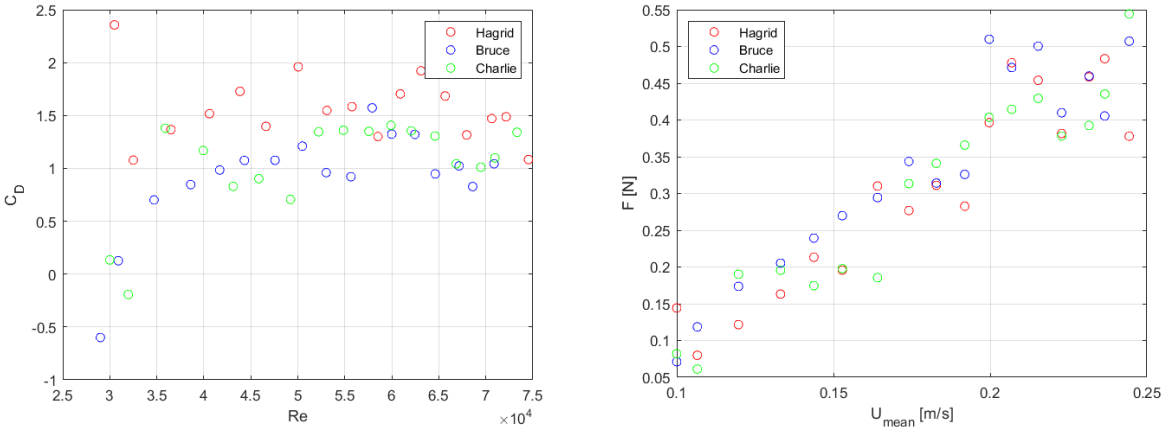

Figure 7: Stable, $\theta = 135^o$

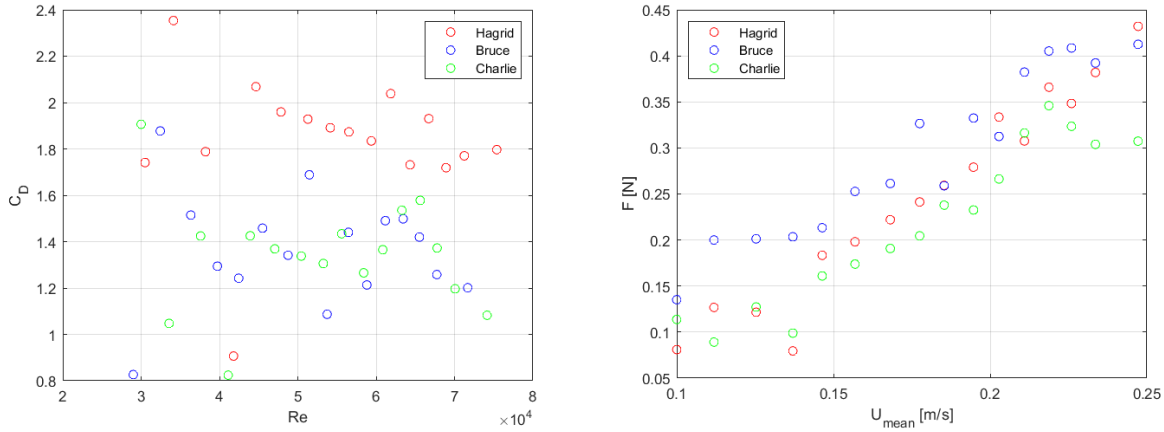

Figure 8: Stable, $\theta = 180^o$

.3 Second measuring system, very stable, surface

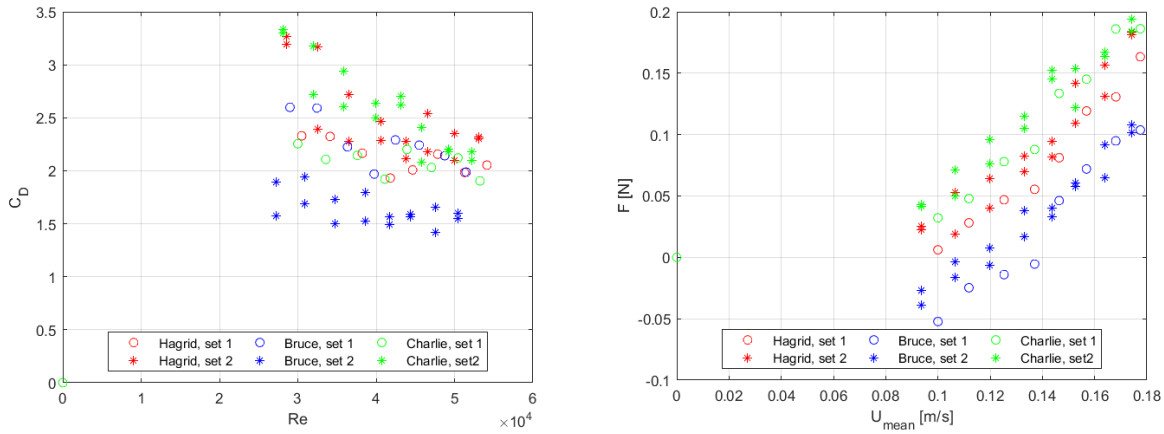

Figure 9: Very stable, $\theta = 0^o$

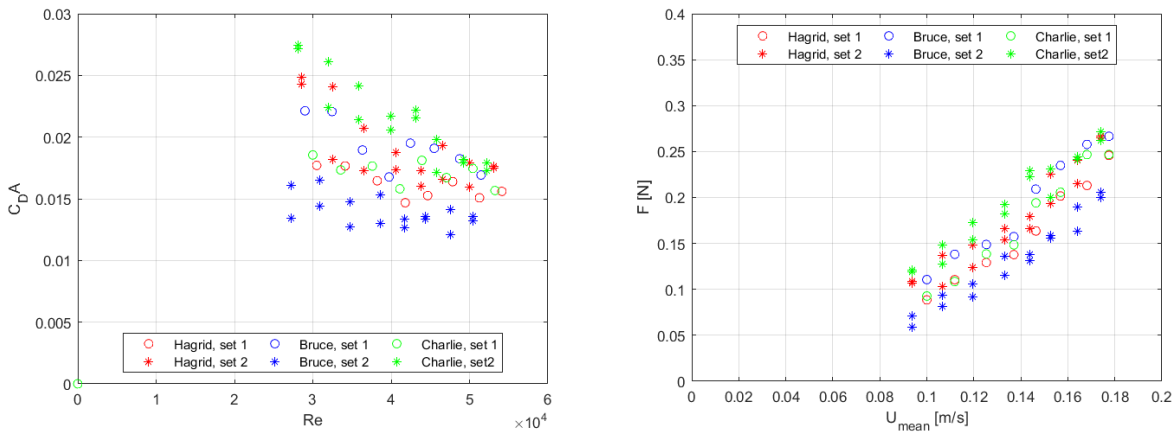

Figure 10: Very stable, $\theta = 0^o$

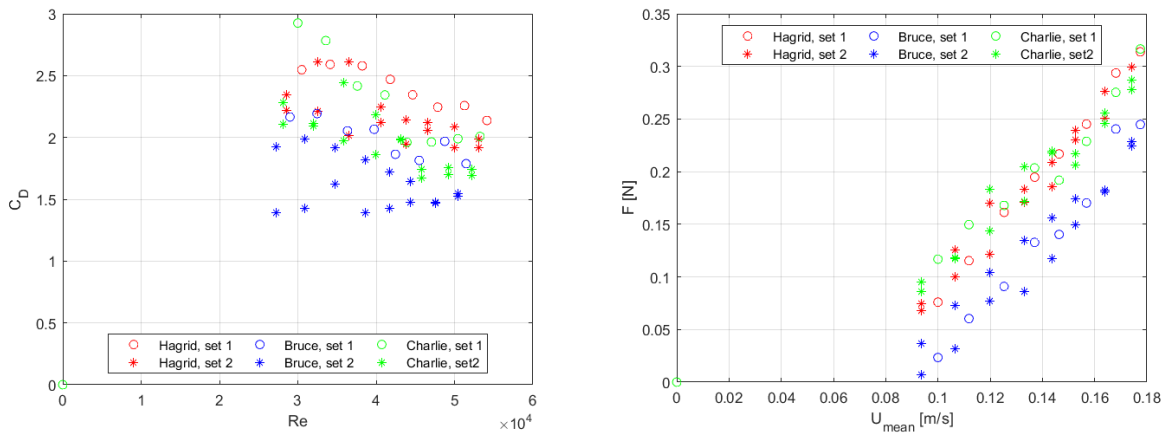

Figure 11: Very stable, $\theta = 45^o$

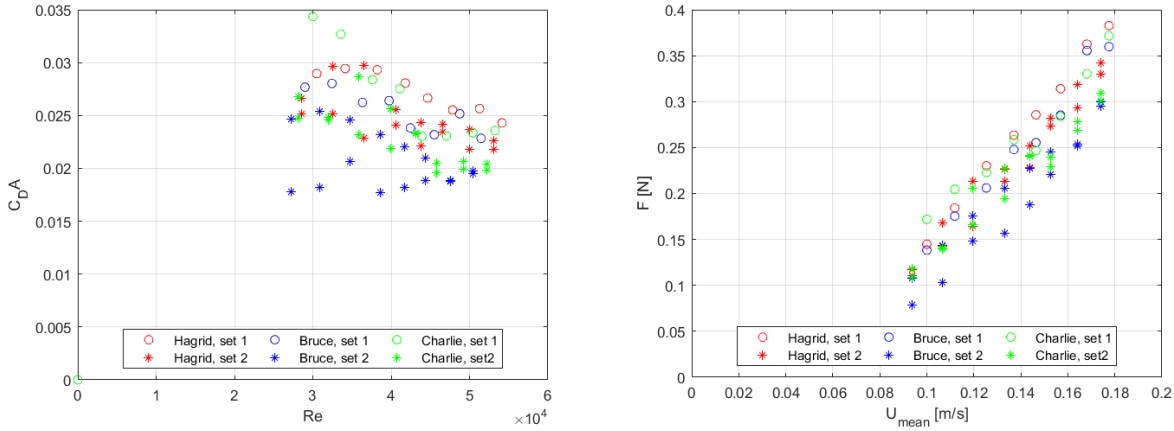

Figure 12: Very stable, $\theta = 45^o$

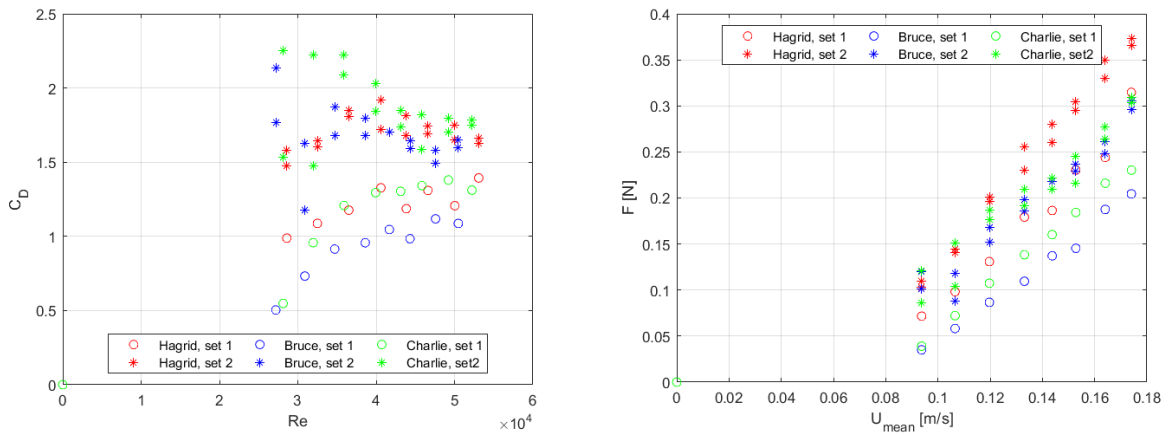

Figure 13: Very stable, $\theta = 90^o$

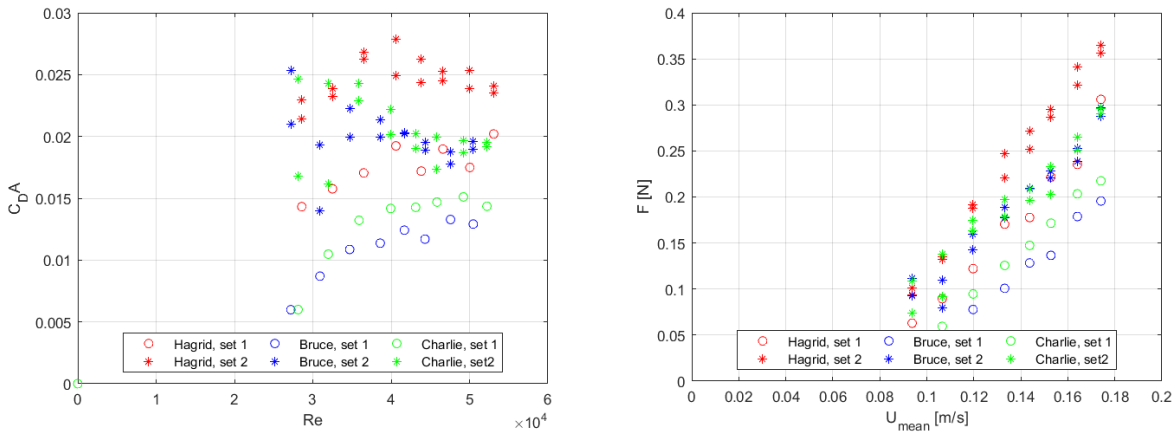

Figure 14: Very stable, $\theta = 90^o$

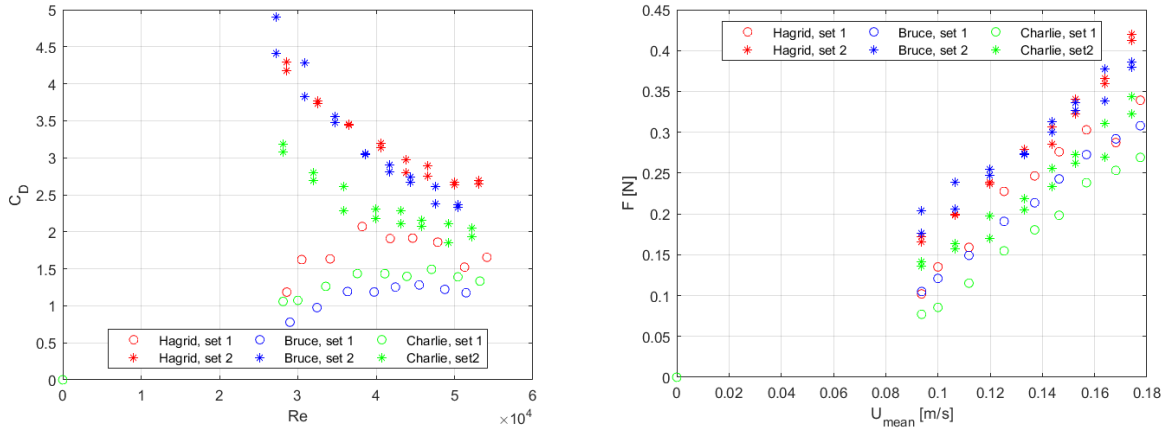

Figure 15: Very stable, $\theta = 135^o$

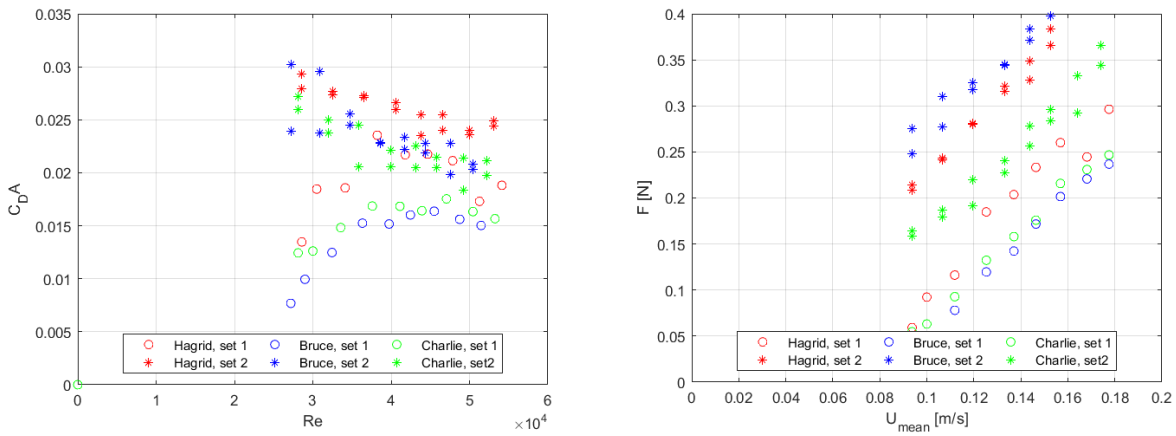

Figure 16: Very stable, $\theta = 135^o$

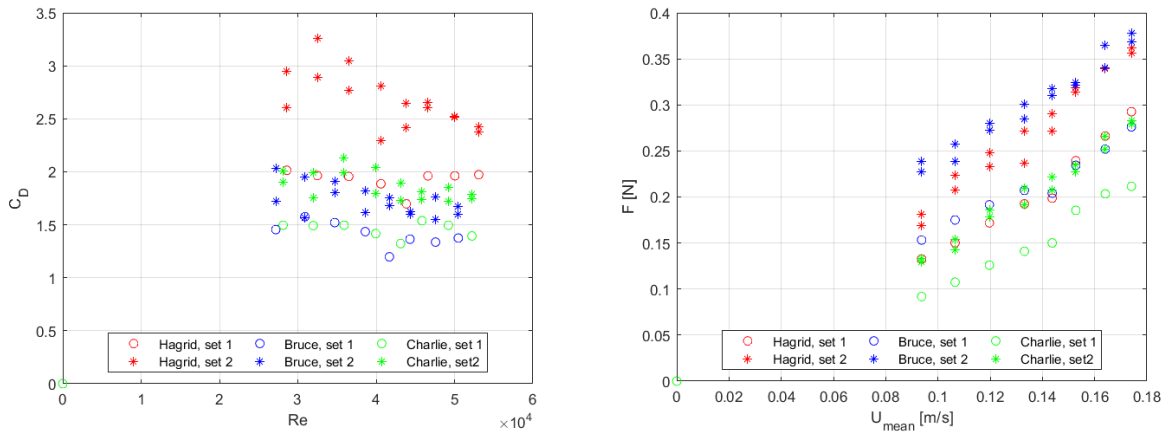

Figure 17: Very stable, $\theta = 180^o$

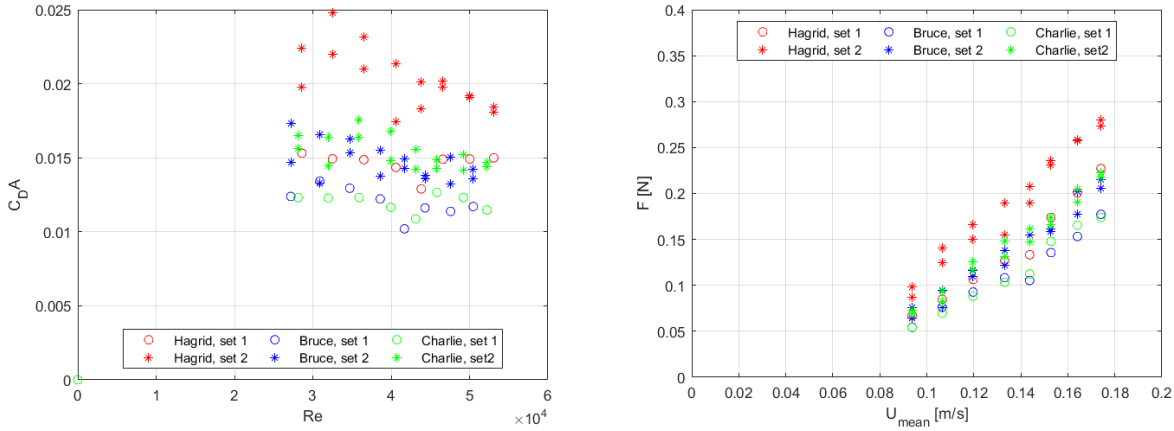

Figure 18: Very stable, $\theta = 180^o$

.4 Second measuring system, very stable, mid height

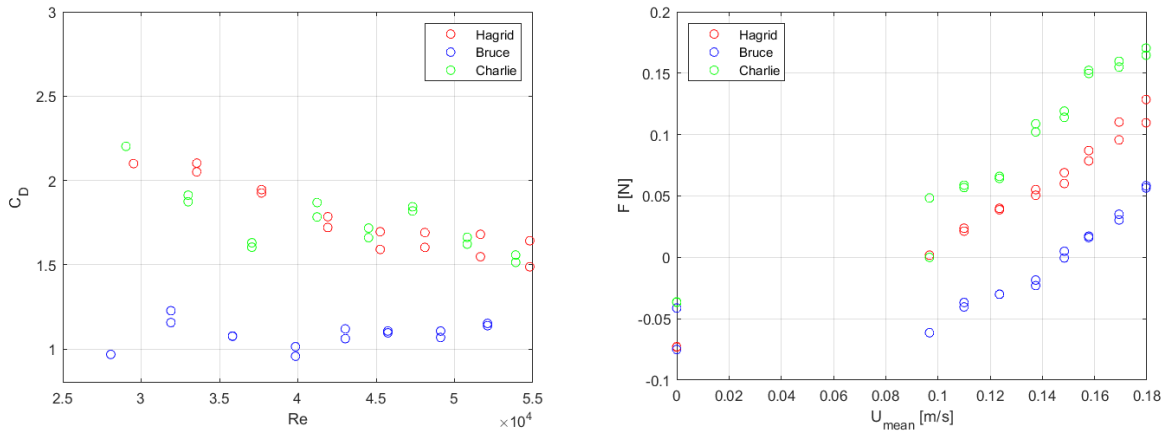

Figure 19: Very stable, $\theta = 0^o$, mid height

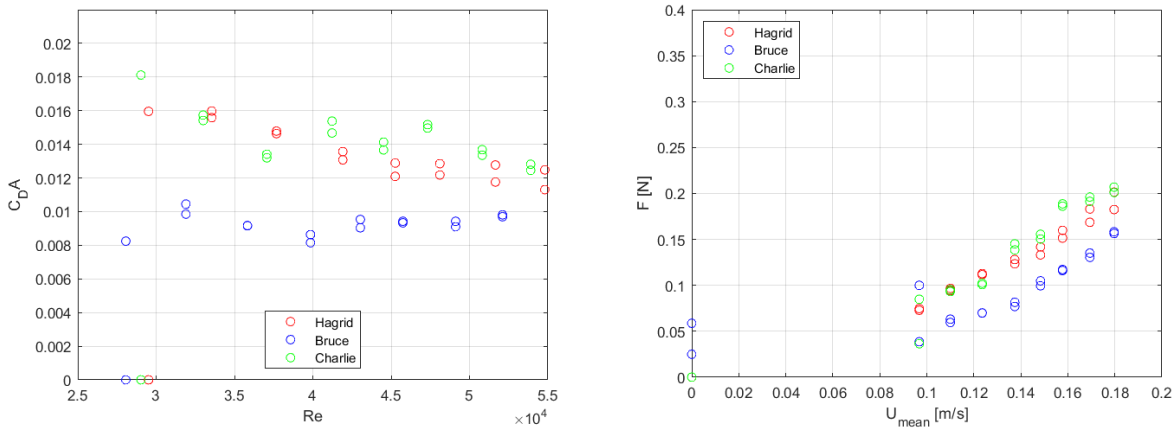

Figure 20: Very stable, $\theta = 0^o$, mid height

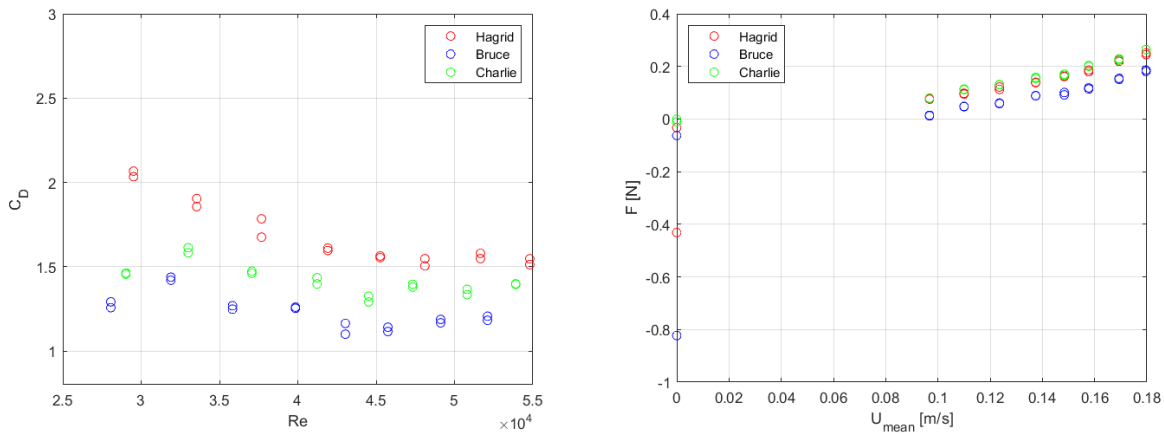

Figure 21: Very stable, $\theta = 45^o$, mid height

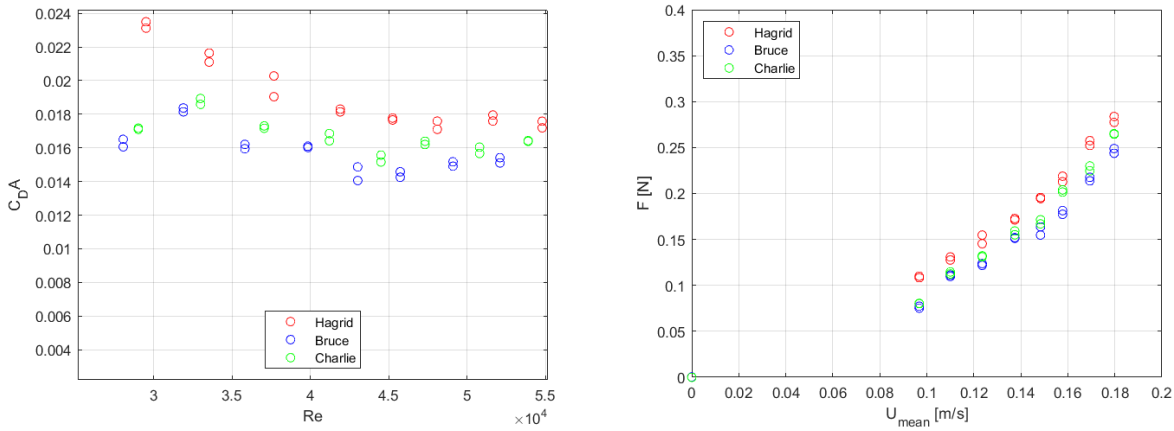

Figure 22: Very stable, $\theta = 45^o$, mid height

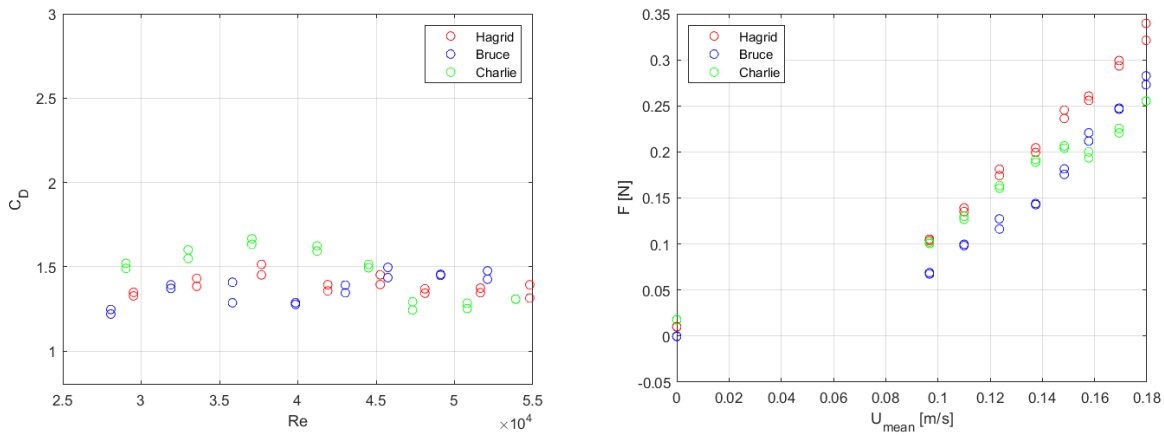

Figure 23: Very stable, $\theta = 90^o$, mid height

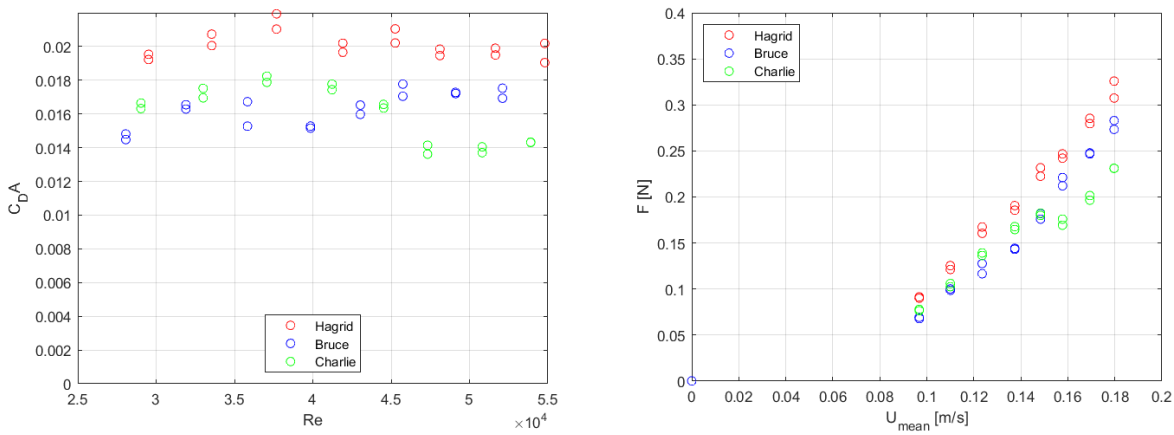

Figure 24: Very stable, $\theta = 90^o$, mid height

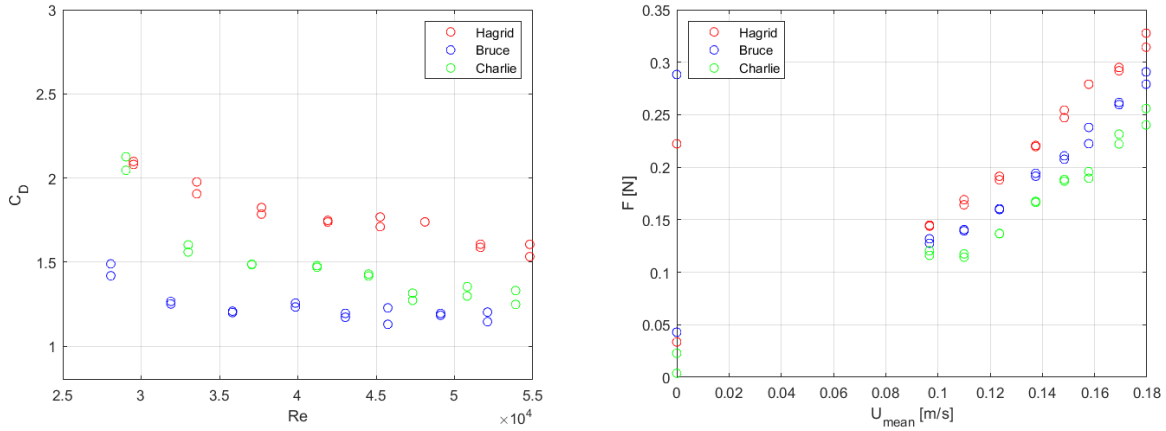

Figure 25: Very stable, $\theta = 135^o$, mid height

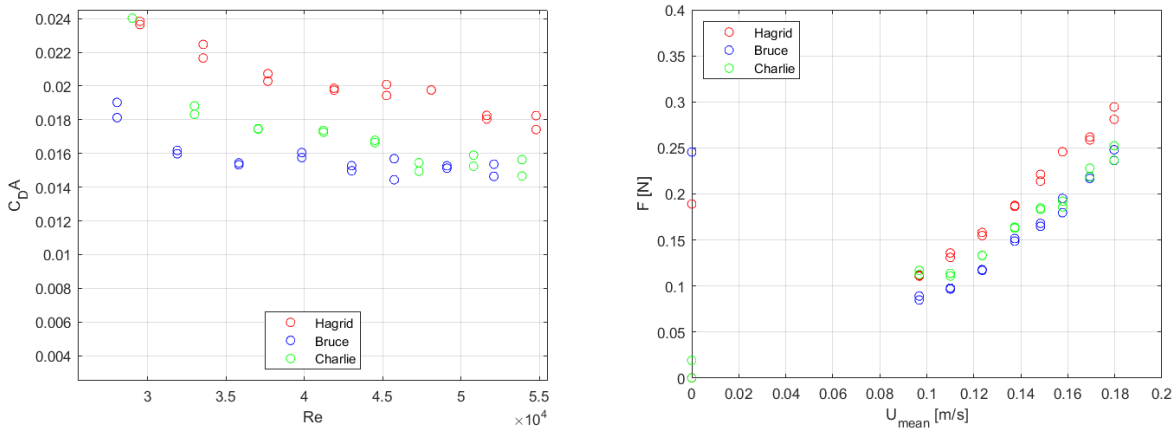

Figure 26: Very stable, $\theta = 135^o$, mid height

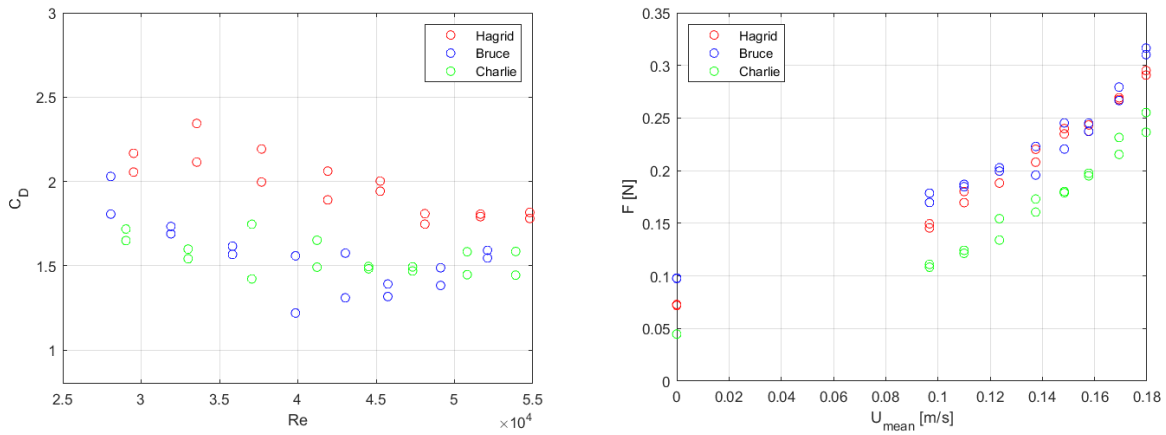

Figure 27: Very stable, $\theta = 180^o$, mid height

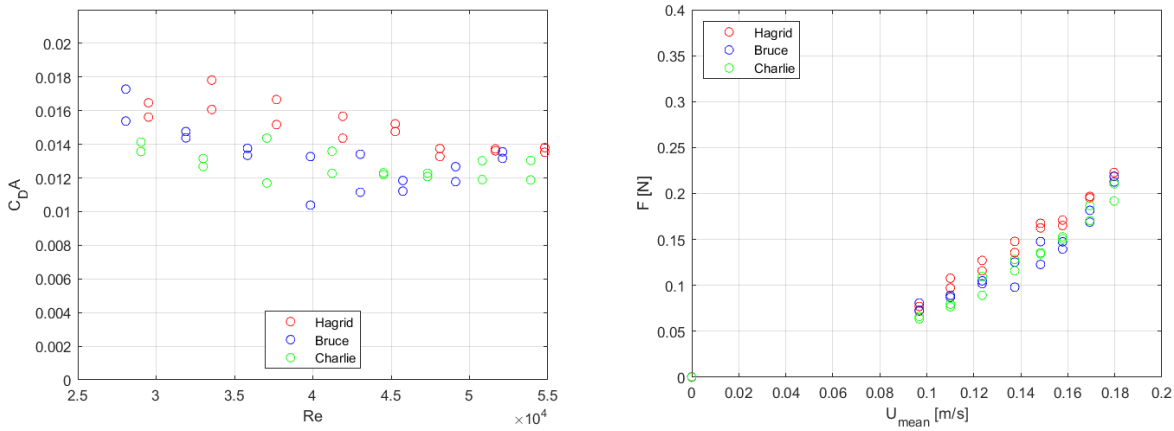

Figure 28: Very stable, $\theta = 180^o$, mid height

.5 Measurement of drag with a $Re = 0$ and lower Re_p

These experiments are realised with the automatic transverse system. Like in section 3.3.2, it is first required to verify the measurement accuracy. To do this, some samples are taken with a cylinder in exactly the same way as in section 3.3.2.

Tests are realised with a velocity of the movable bar from 0.025 m/s to 0.1 m/s and water at rest with the measuring system previously used. Measurements are taken twice per data set and the procedure is repeated twice (MF1 and MF2). Finally there are four C_D for each velocity tested and conclusions can be drawn out of these graphs in Figure 29.

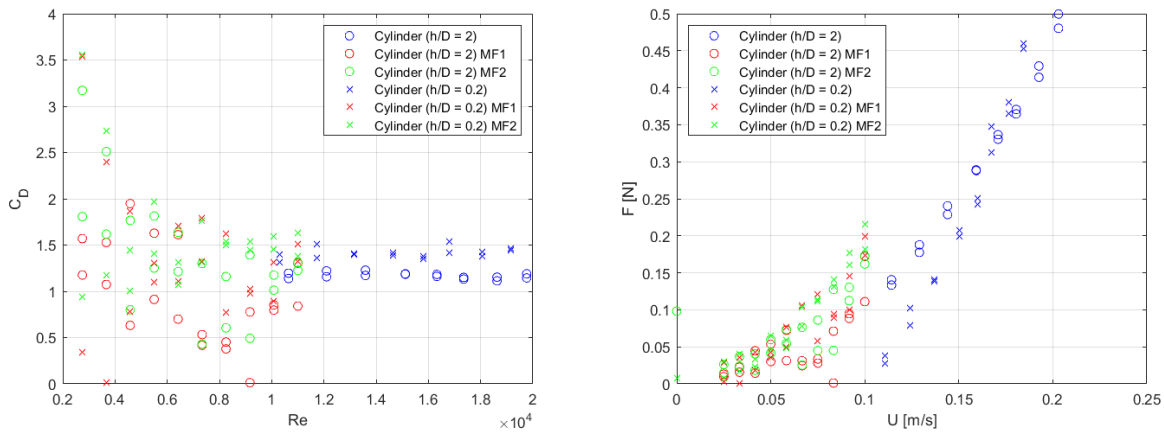

Figure 29: Results of the tests made on the automatic transverse system

These graphs show the high variability of the results. Even with a velocity of 0.1 m/s, which is a velocity tested with in section 3.3.2, results are around the same level but with a higher variability. Indeed the slower the bar, the higher the variability.

Three main reasons for these imprecisions have been identified:

- Problem of stabilisation after the acceleration: as previously mentioned, the available distance for a measurement is 1.2 m. This distance is very short and the acceleration, stabilisation, measurement and deceleration phases have to be made in this 1.2 m. The observed issue is that the acceleration generates an oscillation of the cylinder in water and this oscillation has not enough time to mitigate. Indeed, if the velocity is 0.1 m/s, the 4 phases have to be done in only 12 s in the case of a perfect fit of the automatic transverse system and distance between transverses. It is thus obvious that the cylinder still oscillates before decelerating.
- Value of the force: measured forces are on a range from 0.01 to 0.2 N. It is clear that a force close to the tenth of a Newton is difficult to measure with a sensor measuring an optimal force at 5 N. Noise on the signal and treatment of it influence the results and make interpretation almost impossible[1].

[1]The 1 kg strain gauge is the most precise strain gauge available in the laboratory

- Calibration problem: with the measuring system simply placed on the flume like in section 3.3.2, our system is calibrated between each data set by moving out the system and calibrate it like on picture 3.18. Indeed, temperature influences the force measurement as they are based on its elongation and the measured forces are of very low order. With the system on the automatic transverse system, it was impossible to remove it to make the calibration and an adaptation has to be done for us by calibrating over the flume which is of course less precise. This problem might seem less important but added to the two first ones, it becomes not negligible.

Because of these three reasons, it has been decided to not use the automatic transverse system with our models.